©2020 Uspekhi Fizicheskikh Nauk, Russian Academy of Sciences

INSTRUMENTS AND METHODS OF INVESTIGATION

PACS numbers: 29.25.Ni, **41.75.–i**, 81.16.Nd

Electrohydrodynamic emitters of ion beams

P Mazarov, V G Dudnikov, A B Tolstoguzov

DOI: https://doi.org/10.3367/UFNe.2020.09.038845

Contents

1. Introduction **1219**
1.1 Brief historical background; 1.2 Principal advantages of EHD ion sources
2. Ion optics and the basics of nanosized ion beam production **1221**
2.1 Ion column design; 2.2 Minimal diameter of an ion beam
3. Physical principles underlying the functioning of EHD ion sources **1223**
3.1 Liquid in an electric field, formation of the Taylor cone; 3.2 Ion emission: the principal mechanisms and operation modes
4. Liquid metal ion sources on pure metals and alloys **1226**
4.1 Design of liquid metal alloy ion sources; 4.2 Review of the existing liquid metal alloy ion sources; 4.3 Main emission and ion-optical parameters of liquid metal alloy ion sources
5. Ion sources with room temperature ionic liquids **1236**
6. Principal domains of application of EHD ion sources **1238**
6.1 Ion beam lithography and nanopatterning; 6.2 Focused ion beam systems; 6.3 Local secondary ion mass spectrometry; 6.4 Electrohydrodynamic sources for space exploration
7. Conclusions and prospects **1251**
References **1251**

Abstract. We discuss physical processes underlying the generation of ion beams with high emission current density in electrohydrodynamic (EHD) emitters based on liquid metals and alloys and with room temperature ionic liquids. We consider EHD effects that influence the emission of ions (ion production mechanisms) and the kinetics of ion interactions in high-density beams. We analyze the factors determining the emission zone size, sustainability of emission at high and low currents, generation of clusters, increase in energy spread, decrease in brightness, and other features of ion beams. We consider the specific design features of EHD emitters and the problems of practically ensuring their stable operation. Discussed in detail are modern application areas for ion sources with EHD emitters, including technological installations for ion beam lithography, micro- and nanopatterning, ion microscopes and tools for local mass spectrometry of secondary ions, and systems to control and neutralize the potential of spacecraft as well as electrostatic rocket engines (microthrusters). We analyze prospects for further development of EHD emitters themselves and instruments based on them.

P Mazarov [1, a], **V G Dudnikov** [2, 3, b], **A B Tolstoguzov** [4, 5, 6, c]
[1] Raith GmbH, Dortmund,
Konrad-Adenauer-Allee 8, 44263 Dortmund, Germany
[2] Novosibirsk State University,
ul. Pirogova 2, 630090 Novosibirsk, Russian Federation
[3] Budker Institute of Nuclear Physics,
Siberian Branch of the Russian Academy of Sciences,
prosp. Akademika Lavrent'eva 11, 630090 Novosibirsk,
Russian Federation
[4] Utkin Ryazan State Radio Engineering University,
ul. Gagarina 59/1, 390005 Ryazan, Russian Federation
[5] Department of Physics and Key Laboratory
of Artificial Micro- and Nano-structures of Ministry of Education,
Hubei Nuclear Solid Physics Key Laboratory
and Center for Ion Beam Application, School of Physics
and Technology, Wuhan University,
430072 Wuhan, China
[6] Centre for Physics and Technological Research (CeFITec),
Dept. de Física da Faculdade de Ciências e Tecnologia (FCT),
Universidade Nova de Lisboa, 2829-516 Caparica, Portugal
E-mail: [a] Paul.Mazarov@raith.de, [b] dvg43@yahoo.com,
[c] a.tolstoguzov@fct.unl.pt

Received 14 December 2019, revised 13 July 2020
Uspekhi Fizicheskikh Nauk **190** (12) 1293 – 1333 (2020)
Translated by S Alekseev

Keywords: electrodynamics, liquid metal ion source, room temperature ionic liquid, nanopatterning, secondary ion mass spectrometry, ion beam lithography, liquid metals and alloys, nanotechnology

1. Introduction

In the literature on micro- and nanotechnology published in recent years [1–5], sections devoted to electrohydrodynamic (EHD) [6] ion sources for submicrometer lithography, ion-stimulated chemical synthesis, implantation, and microanalysis have become mandatory. Today, it has become impossible to imagine patterning, analyzing, and processing a given surface relief with submicrometer resolution without a focused ion beam (FIB) [7–9]. Initially, only pure metals with low melting points (liquid metals), mainly gallium, made up the working material of EHD emitters (we here use the terms EHD source and EHD emitter synonymously) [10]. Therefore, the notion of a liquid metal ion source (LMIS) was

primarily associated with a source of gallium ions. But carrying out numerous present-day technological tasks, including local ion implantation doping, ion beam mixing, direct resist-free ion lithography, fabrication of micro- and nanoelectromechanical systems, and nanoengineering of thin-layer objects, is impossible without using beams of ions with different masses, charge states, and chemical properties [1]. This has stimulated the development of liquid metal alloy ion sources (LMAISs) ensuring the generation of a wide spectrum of various ions [2]. The use of eutectic alloys of different compositions has allowed the electrical, optical, magnetic, and mechanical properties of the processed materials to be modified with greater predictability and control. LMISs, and subsequently LMAISs, are also quite broadly used in secondary ion mass spectrometry (SIMS) [11–14] and secondary neutral mass spectrometry (SNMS) [15–18], as well as in space technology [19, 20] and ion microscopy [21, 22].

As a result of investigations conducted in this area over the last half a century, almost half of the chemical elements from the periodic table have turned out to be potentially suitable for use or are already being used in modern LMAISs [2]. In this paper, we detail the physical properties, fabrication technology, hardware features, and principal application domains for LMAISs involving pure metals as well as binary and ternary alloys.

Besides pure metals and metal alloys, low temperature ionic liquids [23–25] with a melting point no higher than 100 °C are used as the working materials in modern EHD emitters. By 'ionic liquids' we precisely mean room temperature ionic liquids. What ion sources working on pure metals, alloys, and ionic liquids have in common is the similarity of their EHD and emission processes. In what follows, we discuss these processes in detail and analyze them, paying attention to specific features of working materials.

The development of ionic liquid ion sources (ILISs) started about 20 years ago, and the principal domain of their application, where they can compete with LMAISs, is space technology, primarily electrostatic micro-jet engines for spacecraft with limited onboard resources, for example, for CubeSat satellites. The use of local reactive (chemical) etching, replacing gallium ion beams with heavy cluster ions of negative polarity, and also the use of ILISs in analytic ion beam devices for SIMS and SNMS, appear to be quite promising.

To summarize the foregoing, we can speak of the long-felt need to write this review covering a wide range of modern EHD ion sources, which have so far not been described in the Russian scientific literature in sufficient detail.

1.1 Brief historical background

The first LMISs based on the phenomenon of EHD emission appeared half a century ago. The physics, technology, and application domains of LMISs are the subject of book [26], several chapters in reference materials, and various handbooks [27–31]; more than a thousand research papers and reviews have been published (a detailed bibliography is given in [2, 32]).

The origins of LMISs are to be sought in early classic studies on the behavior of conducting liquids in an electric field, which were in turn based on observations made in Ancient Greece. In 1600, William Gilbert, a physicist and Queen Elizabeth I's physician, described the 'tendency' of liquid droplets at the end of a needle to extend so as to take the shape of a cone when rubbed amber was brought close to it [33]. In 1732, English astronomer and physicist Stephen Gray introduced the notion of EHD emission. Working with mercury, he discovered the extension of droplets into a meniscus in the electric field, followed by a discharge on the tip and the destruction of the droplet [34]. In 1879, English physicist and Nobel laureate John William Strutt (Lord Rayleigh) theoretically justified the criterion of electrostatic instability of a strongly charged droplet [35], a criterion that remains valid to this day.

In 1914, the Czech–American physicist and inventor of the electroscope John Zeleny studied and documented the effect of an electric field on the change in the shape of a droplet [36–38]. In 1951, Erwin Wilhelm Müller discovered that positive ions are torn off and material undergoes intense field evaporation from a tapered positively charged electrode in a very strong electrostatic field [39]. However, the intense field evaporation results in rapidly blunting the needle and terminating the process.

The first to propose using an LMIS prototype as an electrostatic thruster of space engines was Krohn [40]. Subsequently, for a long time EHD emitters were developed by space agencies as low-thrust engines for spacecraft with limited onboard resources. Capillary-type emitters were used, from the open end of which melted material was evaporated in the form of charged microdroplets by an electric field [41]. Next, emission of atomary ions from a capillary was achieved [42]. At the same time, Gomer published a pivotal paper on electron field emission and field ionization [43]. British physicist Geoffrey Ingram Taylor in 1964 for the first time mathematically rigorously described the change in the shape of a conducting droplet in an electric field [44]. Following that, the cone shape occurring in EHD equilibrium was named after him, although historically it would be more appropriate to call it the Gilbert–Gray–Zeleny–Taylor cone.

In the mid-1970s, Krohn [45, 46] developed and tested LMISs with different metals: Ga, Cs, and Hg. The best results (beam diameter [1] of about 200 nm at the accelerating voltage of 21 keV with brightness of the order of 10^5 A cm^{-2} sr^{-1} and emission current of 10 μA) were obtained with gallium. The first prototype of a modern needle-shaped emitter was built by Clampitt in 1975 [47]. Subsequently, the nanopatterning pioneer Seliger for the first time used an LMIS in an ion-optical device with electrostatic focusing and attained an on-sample beam diameter of the order of 100 nm at the accelerating voltage of 57 kV [48]. By analogy with field electron emitters, the first ion emitters were also strongly tapered, having a tip radius of less than 1 μm [39]. The modern shape of the needle, with a tip radius of 5 to 10 μm, was eventually arrived by accident. Still a graduate student, Venkatesan dropped a manufactured needle and, not bothering to make a new one, wetted it with gallium, thus obtaining an LMIS with much better emission characteristics than before [49].

During the first decade of the active development of EHD sources, no communications about them appeared in the Russian-language scientific literature, and only in 1983 did Gabovich publish the first review, "Liquid-metal ion emitters" in *Physics–Uspekhi* [10]. In the subsequent decade, hundreds of papers on the subject were published in the Soviet Union, which are partially reviewed in papers by Dudnikov and Shabalin [50–55]. Unfortunately, after the

[1] Here and hereafter in this review, the ion beam diameter is understood as the full width of the spatial distribution of ion current density at the level of half the maximum value of this density (FWHM, full width at half maximum).

Table 1. Main characteristics of ion sources for modern FIB systems, ion lithography, nanopatterning, ion microscopy, and microanalysis.

Source type	Ions	Brightness, A m^{-2} sr^{-1} V^{-1}	Energy spread (FWHM), eV	Ion current, nA	Beam diameter (FWHM), nm	Literature
LM(A)IS	Li, Be, B, C, Si, Co, Ga, Ge, Au, Bi, and others	10^6	5–10	$\leqslant 50$	2.5	[2, 7]
ILIS	$[R]^+$, $[A]^-$, $\{[R]^+[A]^-\}_m[R]^+$, $\{[R]^+[A]^-\}_m[A]^-$	10^5-10^6	5–15	$\leqslant 10^3$	5–50	[25, 61]
ECRIS [(1)] ICPIS [(2)] RFPIS [(3)]	Xe, Kr, Ar, O, N, and others	10^4	1–5	$\leqslant 10^4$	20	[62–65]
MOTIS [(4)]	Li, Rb, Cr, Cs	10^7	0.35	0.5–1	10–30	[66, 67]
NAIS [(5)]	Inert gases, H	10^4	1–2	$\leqslant 0.23$	50–60	[68, 69]
GFIS [(6)]	Inert gases	10^9	1	$\leqslant 0.025$	0.35	[21, 70]

Note. Some ion sources listed in the table have no commonly accepted names or abbreviations in Russian.
[(1)] ECRIS: electron cyclotron resonance ion source.
[(2)] ICPIS: inductively coupled plasma ion source.
[(3)] RFPIS: radio-frequency plasma ion source.
[(4)] MOTIS: magneto-optical trap ion source.
[(5)] NAIS: nano-aperture ion source.
[(6)] GFIS: gas-field ion source.

breakup of the Soviet Union, interest in the further development and studies of LMISs in the Russian Federation considerably decreased.

Since the late 1960s, work has been underway on creating LMISs based on indium and cesium for space applications. The first tests of an indium LMIS developed in the framework of the joint Soviet–Austrian project LOGION and intended for neutralization of the positive charge that appears on the surface of spacecraft under the action of solar wind, Earth's plasmasphere, and solar radiation, were conducted in 1991 aboard the space station Mir [19].

In the 1980s, researchers began actively seeking other materials suitable for use as the working material in EHD sources. The use of eutectic alloys with low melting temperatures led to the creation of the first LMAISs. Subsequent studies of multicomponent alloys for LMAISs considerably extended the prospects for their application. A detailed historical account is available in review [2].

One of the first ionic liquid sources [23] working in the mode of EHD ion emission was developed and tested at the beginning of the 21st century by Losano's group at the Massachusetts Institute of Technology (Cambridge, USA). The source had a needle emitter made of tungsten, similar to the one used in classic LMISs, but was wetted, not with a melted metal, but with the ionic liquid 1-ethyl-3-methylimidazolium tetrafluoroborate [emim][BF_4].

We note that, back in the mid-1980s, attempts were undertaken to use melts of different inorganic salts, such as metaborates, nitrides, and halogenides of alkali metals, primarily lithium, and also an alkali of sodium hydroxide as the working materials in EHD emitters for the generation of both positive and negative ions [54–58]. This work did not develop further, because the melts of the salts used and the alkali were chemically active, which resulted in rapid degradation and destruction of the metal needles of the emitters, and the emitted ions showed a large energy spread, about 100 eV for Li^+ ions [56]. In principle, EHD emitters with melts of inorganic salts and an alkali can be regarded as precursors, even if not entirely successful, of modern ion sources working on eutectic alloys and room temperature ionic liquids.

1.2 Principal advantages of EHD ion sources

Electrohydrodynamic sources allow obtaining currents of atomic and molecular (cluster) ions of different elements and their chemical compounds with densities up to hundreds of millions of A cm^{-2} and low energy spread, which usually greatly impresses all those aware of typical features of other types of ion emitters. EHD sources also exhibit high stability, sustainability, and a long lifetime [2].

The main characteristics of EHD sources and what distinguishes them from the vast variety of gaseous, plasma, and other types of ion sources are analyzed in detail in [14, 59]. We note that relatively recently an attempt to classify ion sources for FIB systems was made in review [60]. In Table 1, we list comparative characteristics of ion sources that are already in use or can potentially be used in modern FIB devices, ion lithography, nanopatterning, ion microscopy, and microanalysis. By the brightness of sources in Table 1, we understand the ion current emitted into the unit solid angle with normalization to the accelerating voltage, and the data on energy spread of ions and the ion beam diameter on the irradiated object are given as the full-width half-maximum (FWHM) value. For ion sources with ionic liquids, the 'ions' column includes $[R]^+$, $[A]^-$, $\{[R]^+[A]^-\}_m[R]^+$, $\{[R]^+[A]^-\}_m[A]^-$, where $[R]^+$ and $[A]^-$ are, respectively, cations and anions involved in the composition of ionic liquids, and $m \geqslant 1$. These abbreviations are described in detail in Section 5 below.

2. Ion optics and the basics of nanosized ion beam production

2.1 Ion column design

To obtain ion beams that ensure nanosize spatial resolution, modern FIB systems use a relatively simple ion-optical system whose main modules were developed and described practi-

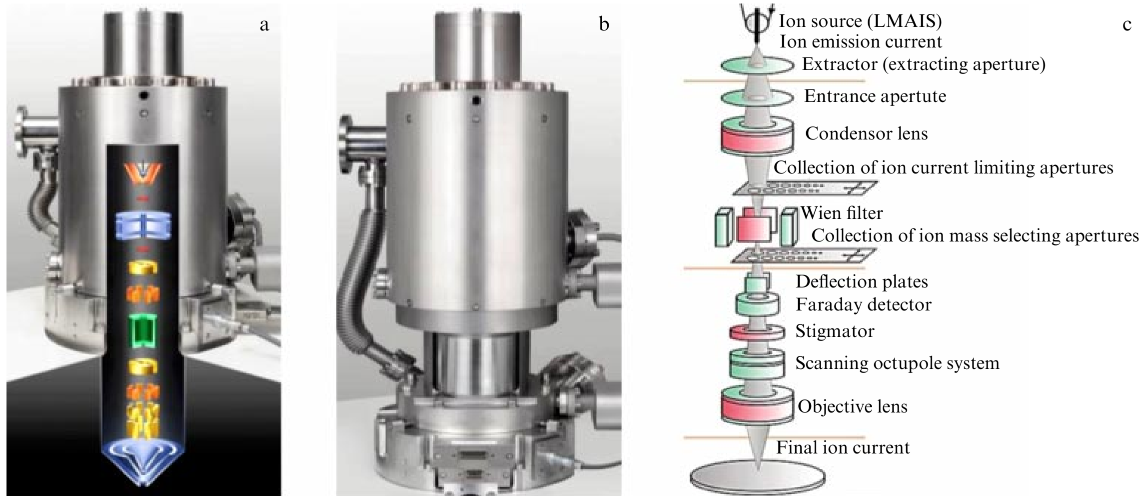

Figure 1. Typical design of an ion column: (a) without and (b, c) with a Wien filter (Raith GmbH).

cally simultaneously with the appearance of LMAISs [48]. In Fig. 1, we show a skeleton diagram of an ion column used by Raith GmbH (Germany). Along with the ion source, the main components of the ion column are the extractor electrode and the entrance aperture, condensor and object lenses, a collection of apertures restricting angular spread and the ion beam diameter, a Wien filter with a selection aperture, a deflection plate, a Faraday detector, a stigmator, and a scanning electrostatic octupole system [71]. Because of the ultra-high vacuum requirements for the operation of LMAISs, the column is divided into three vacuum sections with autonomous pumping. The setup, its configuration, and the principle of operation of suchlike ion columns are described in detail in specialized reference literature [27, 28, 72, 73].

The condensor lens serves to specify the trajectory of ions in the column. In Fig. 2, we show the geometry of motion of the ion beam in a column, with five main modes considered in the order of increasing voltage on the condensor lens. The modes that do not involve the condensor lens or the objective lens (which means that their voltage is equal to zero) are not used in modern columns, but can be utilized occasionally to achieve a more precise adjustment of the column. We note that the divergent and parallel beam modes are the main ones in ion lithography for on-target currents below 1 nA. A divergent beam allows achieving the minimal ion spot size at the optimum distribution of ion current in the beam for small currents (up to 0.1 nA). The parallel beam mode is used for moderate currents in the range of 0.1–1 nA. The last mode with a crossover inside the aperture is basic in all FIBs for high currents (up to 100 nA) and the only possible one in systems equipped with a Wien filter mass separator [74, 75]. We note that in an ion column without a mass separator, ion beams with different m/z ratios are focused onto points displaced with respect to one another due to the displacement in Earth's magnetic field (with the induction approximately equal to 1 G in Europe). For example, in the VELION scanning ion microscope, at the accelerating voltage of 30 kV and the simultaneous use of gold and silicon ions with an AuSi-LMAIS, slow single-charged gold ions with a speed of 170 km s^{-1} produce an image approximately 1.2 μm to the left of the faster double-charged silicon ions, whose speed is 640 km s^{-1}. This displacement increases with a decrease in the accelerating voltage and an increase in the free path of ions.

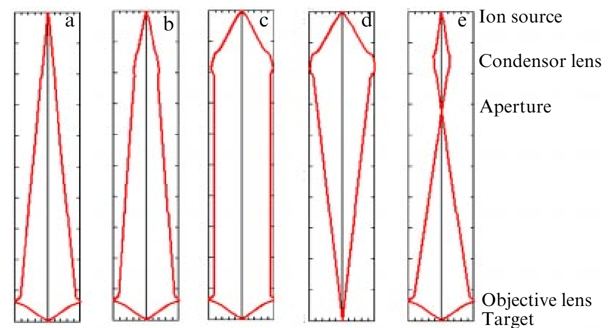

'**Figure 2.** Trajectory of ions in a column with increasing voltage on the condensor lens: (a) without the use of a condensor lens, (b) divergent beam, (c) parallel beam, (d) without the use of an objective lens, (e) crossover inside the aperture.

2.2 Minimal diameter of an ion beam

The most important characteristic of any ion column is the focusing of the ion beam to the smallest possible quasi-zero-dimensional size [26]. The minimal ion beam diameter d on the target is

$$d = \sqrt{(M d_{\mathrm{q}})^2 + d_{\mathrm{s}}^2 + d_{\mathrm{c}}^2 + d_{\mathrm{b}}^2}\,, \tag{1}$$

where M is the optical magnification of the ion column, d_{q} is the virtual (imaginary) spot size of the source, d_{s} is the spherical aberration disk, d_{c} is the chromatic aberration disk, and d_{b} is the diffraction disk.

In turn, d_{s}, d_{c}, and d_{b} are given by

$$d_{\mathrm{s}} = \frac{1}{2} C_{\mathrm{s}} \alpha^3\,, \quad d_{\mathrm{c}} = C_{\mathrm{c}} \left(\frac{\Delta E}{E}\right) \alpha\,, \quad d_{\mathrm{b}} = 0.6 \frac{\lambda}{\alpha}\,, \tag{2}$$

where α is the entry angle of ions in the target, C_{s} is the spherical aberration coefficient, C_{c} is the chromatic aberration coefficient, E is the energy of ions, ΔE is energy spread, and λ is the de Broglie wavelength of the ions, which can be calculated as

$$\lambda = \frac{h}{p} = \frac{h}{\sqrt{2meU}}\,, \tag{3}$$

where h is the Planck constant, m is the ion mass, U is the accelerating voltage, and $p = mv$ is the ion momentum.

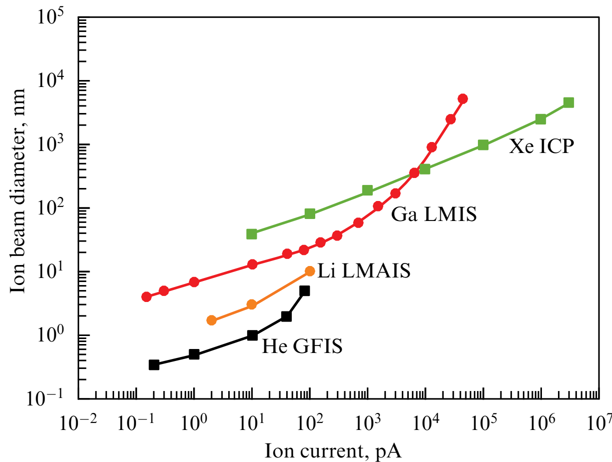

Figure 3. Dependence of the ion beam diameter on the ion current for different sources used in modern FIB systems (based on the data in Table 1) [76].

The ion entry angle is given by the formula

$$\alpha^2 = \frac{I}{\pi M^2 (\mathrm{d}I/\mathrm{d}\Omega)}\,, \tag{4}$$

where I is the initial ion current and Ω is the angular spread of ions in the beam.

An inspection of formulas (1)–(4) shows that the optical magnification of an ion column is initially determined by the sizes and design of the column, and it can be varied within a narrow range by changing the potential on the condensor lens (see Fig. 2). We recall that the de Broglie wavelength of ions is negligibly small compared with that of electrons, and therefore the effect of diffraction on the blurring of the spot is not typically taken into account. The entry angle (acceptance) of the ions is determined by the choice of the aperture that limits the ion current. At high ion currents (1–100 nA), the main contribution to the ion beam diameter is made by spherical aberration, but in the range of moderate currents (10–50 pA), its effect becomes insignificant. The leading role is then taken by chromatic aberration. Up to 10 pA, the main contribution is made by the virtual size of the source. Hence, from the practical point of view, a substantial effect on the ion beam diameter is produced by the accelerating voltage, the overall ion current, the energy spread of ions and the virtual size of the source. In what follows, we consider the relation of these parameters to the types of ions used in EHD sources in more detail. As an example, Fig. 3 shows the dependence of the gallium beam diameter on the ion current compared with the best-known sources employed in modern FIB systems [76].

3. Physical principles underlying the functioning of EHD ion sources

3.1 Liquid in an electric field, formation of the Taylor cone

Investigations of the shape of the liquid surface in an electric field began early in the 17th century, as we have already noted in the history section of this review. Modern ideas regarding the operation of EHD emitters are derived from Taylor's paper [44], where it was proven mathematically that, at the

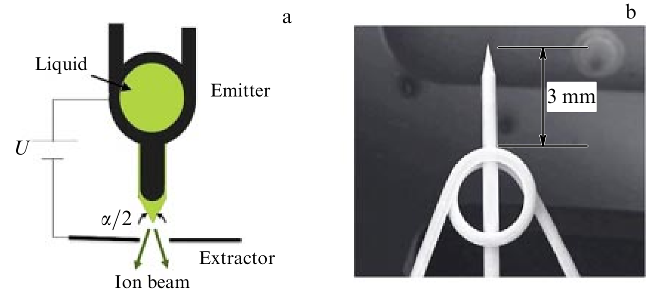

Figure 4. (a) Schematic image of an EHD ion source with a needle metallic electrode wetted with working liquid. (b) Photograph of such an electrode without the working liquid [77].

threshold potential difference between an extractor electrode containing an exit orifice for ions and the tip of a needle-shaped emitter electrode wetted with a conducting liquid, the surface of this liquid is deformed (takes a more sharp shape) and evolves into a cone (Taylor's cone) with a half-angle at the apex of $\alpha/2 = 49.3°$ (Fig. 4a).

The condition for the formation of such a cone is the quasistationary equilibrium of forces due to surface tension γ of the liquid and the action of the electric field with field strength E directed along the normal to the Taylor cone surface:

$$\gamma\left(\frac{1}{r_1} + \frac{1}{r_2}\right) + \frac{\rho}{2} v^2 - \Delta p = \frac{E^2}{8\pi}\,, \tag{5}$$

where r_1 and r_2 are the principal radii of curvature of the Taylor cone, $\Delta p = p_{\mathrm{int}} - p_{\mathrm{ext}}$ is the difference between pressures inside and outside the liquid, and ρ and v are the density of the liquid and its flow velocity.

If we assume that the surface of the Taylor cone has the mean curvature radius r, then, ignoring the action of space charge, we can obtain the threshold (minimal) electric field strength E_{min} as

$$E_{\mathrm{min}} = \sqrt{\frac{4\gamma}{\varepsilon_0 r}}\,, \tag{6}$$

where ε_0 is the electric constant.

It then follows that the threshold potential difference U_{min} for an EHD source shown schematically in Fig. 4a can be calculated as

$$U_{\mathrm{min}} = \sqrt{\frac{\gamma r}{\varepsilon_0}} \ln \frac{2d}{r}\,, \tag{7}$$

where d is the distance between the Taylor cone apex and the extractor electrode.

It follows from formula (7) that the threshold potential difference is sensitive to the surface tension of the working liquid. The surface tension of room temperature ionic liquids is lower than that of liquid metals. For example, $\gamma = 0.71$ N m^{-1} for gallium, and $\gamma = 0.039$ N m^{-1} for the [emim][Tf_2N] ionic liquid; at the same geometry of the source and the curvature radius of the Taylor cone, U_{min} for ILISs is approximately four times less than for gallium LMISs. We also note that Taylor's model in [44] is rather simplified, because it ignores the effect of space charge and the evolution of the surface of the conducting liquid in an increasing electric field, and therefore formulas (6) and (7) are based on

necessary, but not sufficient conditions for the formation of an equilibrium conic configuration on the apex of an EHD emitter. The question of the Taylor cone formation and its stability in different operation modes of EHD emitters is discussed in greater detail, e.g., in [7, 27] and the references therein.

An EHD emitter with a needle electrode whose tip has a radius of 3–10 μm and with a ring reservoir (Fig. 4b) or a helix for storing the working material is typically made of a refractory metal, for example, tungsten. This design is one of the most popular ones, distinguished by its simplicity and universality, which allow working with very different materials, including ionic liquids. The working material is heated in such an emitter by the Joule heat released by directly flowing electric current through the electrodes.

There are also other, more intricate, designs involving thin metal capillaries filled with the working material, as well as capillaries with an inserted metal needle whose tip extends through the open end of the capillary. The heating can be done indirectly due to electron bombardment. The needle-shaped electrode can be fabricated from porous tungsten, which plays the role of a reservoir and of a transport system for delivering working liquid to the tip of the emitter. There are linear (slit) designs of EHD emitters, in which a number of point-like Taylor cones (up to a hundred per millimeter in length) are formed along the slit [78]. Such a source has a high efficiency but at the same time is not suitable for micro- and nanotechnology, because it generates an extended ribbon beam [79].

In this section, we do not aim to cover the entire variety of designs of modern EHD emitters, but wish to emphasize the common features of physical processes that govern the behavior of the liquids (melts of pure metals and alloys, inorganic salts, and ionic liquids) in an electric field with a strength of 10^6 V cm^{-1} or above. Specific features of different EHD emitters are discussed in more detail in Sections 4 and 5, which are devoted to LMISs, LMAISs, and ILISs.

3.2 Ion emission: the principal mechanisms and operation modes

Currently, it is generally accepted that at low currents (below 10 μA), the principal mechanism of ion emission in EHD sources is the field evaporation of ions from the surface of the working liquid in a strong electric field [80–84]. According to Arrhenius's law [80, 82], the rate constant of this process can be written as

$$K = \omega \exp\left[-\frac{G - \sqrt{e^3 E}}{kT}\right], \tag{8}$$

where ω is the ion oscillation frequency ($\omega \sim 10^{12} - 10^{13}$ s^{-1} [80, 81]), k is the Boltzmann constant, T is the absolute temperature, e is the electron charge (in the case of single-charged ions), G is the energy of activation of ion evaporation, and E is the evaporating electric field strength. The expression in the radicand describes a decrease in the surface barrier near the emitter surface due to the Schottky effect [85]. With formula (8), we can easily calculate the ion current density as

$$j = eN_{\mathrm{s}}K, \tag{9}$$

where N_{s} is the density of atoms on the surface of the emitter ($\sim 10^{15}$ cm^{-2}).

For metals, G can be calculated in the thermo-ion cycle approximation as [80, 81]

$$G = \Lambda + I - W, \tag{10}$$

where Λ is the energy of sublimation of a neutral atom from the metal surface, I is the ionization energy of that atom (the first ionization potential), and W is the energy released as the liberated electron returns to the metal (it is equal to the electron work function in the metal $e\varphi$). We note that bombarding the emitter with such electrons leads to an increase in its temperature. In the case of a liquid metal ion source with gallium, G is conventionally taken to be equal to 0.1 eV, and the evaporating field strength is estimated in the range of 10–50 V nm^{-1} [80].

A major problem occurring in trying to apply the field evaporation theory to EHD emitters is the necessity of ensuring a very small radius of the tip of the emitter in order to obtain the required electric field strength. The current density and the space charge magnitude are then very high, as is the voltage that must be applied to the emitter. This problem is circumvented, however, if we assume that the Taylor cone near the apex is deformed, leading to the appearance of a protrusion from which the ions are being emitted (Fig. 5). In this way, it is possible to reconcile the theoretical and experimental voltages on the EHD emitter.

A liquid cone with a protrusion at the apex was simulated numerically in [86], taking the space charge and the motion of the liquid in the cone into account. Computing the thermal mode of such a protrusion 3 nm in diameter [87] with the field evaporation of ions occurring from its apex confirmed the validity of the proposed model, which overall agrees well with experimental data. We also note that methods for the analytic determination of the length and diameter of the protrusion can be found in [88].

The field evaporation of ions from the surface of a liquid protrusion at the apex of a Taylor cone is the dominant

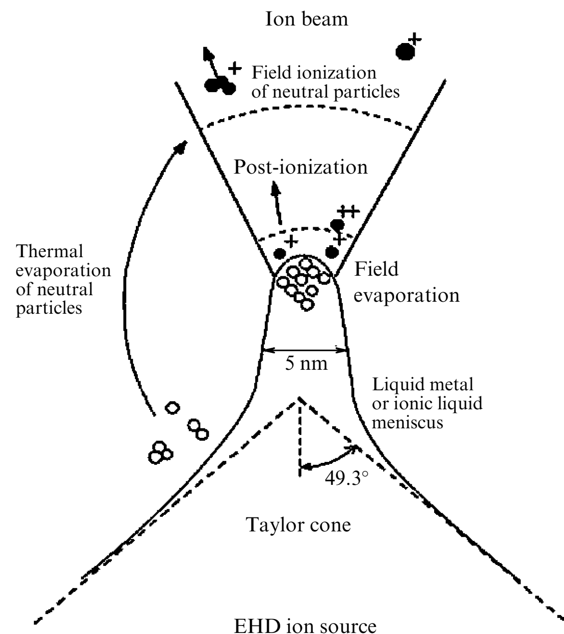

Figure 5. Schematic representation of processes occurring at the protrusion formed at the apex of a Taylor cone in an EHD emitter with a liquid metal (alloy) or ionic liquid [31].

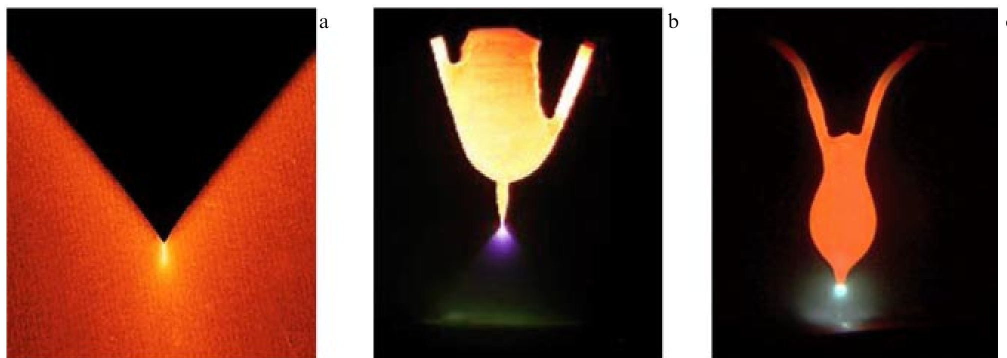

Figure 6. Glow near the EHD emitter tip: (a) with gallium liquid at room temperature, (b) with the HoNi alloy at 800 °C and (c) with the CoNd alloy at 700 °C [2].

process in the mode of low emission currents (less than 10 μA). In the mode of high currents (more than 100 μA), which has little use in modern FIBs, field ionization of the evaporating atoms can start and gas discharge can be initiated in a metal vapor cloud near the apex of the tip. A conjecture was made in [89] that explosive emission can occur from the end of the liquid metal jet at high currents; in [90], a model of a plasma cloud was proposed that can hardly be considered justified. A detailed discussion of these models is outside the scope of this review, and their critical comparative analysis can be found in Dudnikov and Shabalin's works [50–53, 91, 92]. As we can see from Fig. 5, the process of direct field evaporation of ions can be accompanied with post-ionization immediately after their breakaway, which leads to the formation of double- and sometimes of triple-charged ions [93–95].

Simultaneously with ion emission, a characteristic glow appears in EHD emitters in the form of a bright spot near the tip of the needle (Fig. 6), with the intensity of the glow rapidly increasing as the current increases. Spectroscopy investigations conducted for gallium LMISs have shown [49, 96] that the glow comes from gallium atoms excited by the ion beam. The causes of the appearance of high-density metal vapor near the emission zone remain vague. The conjecture that the metal atoms evaporate from the lateral surface of the Taylor cone and are dragged into the strong-field domain near the emission zone [97, 98] is not entirely justified, because the density of saturated vapor of gallium is extremely low, and the drag of the atoms into the strong-field domain becomes substantial only at the low (nitrogen) temperatures of the tip [80]. The experiment in [99] showed that heating the emitter with gallium to 450 °C does not lead to an increase in the intensity of the glow, although the gallium evaporation rate strongly increases at that temperature. In our opinion, one of the causes of the appearance of a gaseous cloud is that, in the process of the field evaporation of ions, which is manifestly nonequilibrium, energy can be transferred to the nearest, surface, atoms, which stimulates their evaporation and eventually leads to the formation of high-density vapor. Another possibility could be the quantum (dipole) character of the glow near the tip of the needle due to time variation of the electric dipole moment of the evaporated atoms of the metal in the emission zone in a strong electric field, causing a spontaneous transition of the system of atoms from the state with a higher potential energy to a lower-energy state [100].

The main difference between the process of field emission from ionic liquids and the processes in metals and alloys is that it is not neutral atoms that are evaporated from the ionic liquid, but positively or negatively charged ions. Similarly to electrolyte solutions, field evaporation of ions, which has been considered in detail in [101, 102], in the case of ionic liquids in formula (10) is to be used not with the activation energy G of ion evaporation from a metal surface but with the change in enthalpy $\Delta H_{+(-)}$ in the transition of an ion from the ionic liquid to the vacuum.

In the literature that we are aware of, no data are available on the $\Delta H_{+(-)}$ values for ionic liquids; processes of field evaporation of ions from ionic liquids are more complicated than for aqueous solutions of salts [101]. Under the action of an electric field, evaporation of neutral ion pairs $\{[R]^+[A]^-\}_n (n \geqslant 2)$ is possible with their subsequent dissociation into cations $[R]^+$ and anions $[A]^-$. Depending on the polarity of the accelerating voltage applied to the emitter, either cations or anions would return to the ionic liquid surface, initiating its etching, heating, and degradation due to ion bombardment. Moreover, the evaporated neutral pairs that are spatially close to the apex of the Taylor cone can interact with the newly formed cations and anions, resulting in the formation of complex ions $\{[R]^+[A]^-\}_m[R]^+$ and $\{[R]^+[A]^-\}_m[A]^-$, where $1 \leqslant m \leqslant n-1$. We note that the occurrence of molecular ions was observed when using the melt of lithium metaborate $LiBO_2$ as the working material in an EHD emitter [54].

Two principal modes of operation of EHD sources must be singled out. Depending on the specific conductance and surface tension of the working liquid, the speed of delivering it to the apex of the emitter (feed speed) and the electric field strength of the source can work either in the pure ion emission mode, producing beams of single- and multiple-charged atomary and cluster ions, or in the mode of emission of charged droplets. A mixed mode is also possible, with the source emitting both ions and charged droplets.

For liquid metals and alloys with the specific conductance $\sigma > 10^5$ S m^{-1} and high surface tension, the first mode is dominant, and for electrolyte solutions with $\sigma < 10^{-3}$ S m^{-1}, the characteristic mode is that of the emission of charged droplets, up to several micrometers in diameter. This mode is also called the colloid electrospray mode [103–105].

According to their specific conductance $\sigma \sim 0.1$–10 S m^{-1} and surface tension $\gamma \sim 0.01 - 0.1$ N m^{-1}, ionic liquids are intermediate between liquid metals and electrolyte solutions, and therefore ILISs can work in both modes. At low conductance and high feed speed of the ionic liquid, the apex of the Taylor cone deforms, leading to the formation of a thin extended jet (the cone jet) [105, 106] emanating from

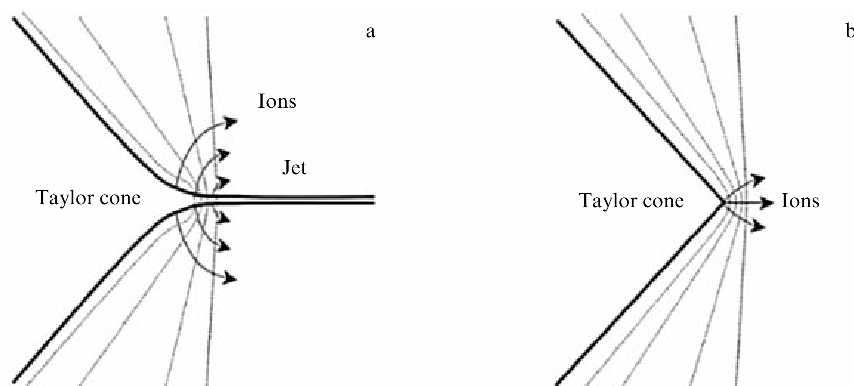

Figure 7. Operation mode of an EHD source: (a) droplet (jet) mode, (b) mode of pure ion emission. Dotted lines show equipotential lines near the apex of a Taylor cone [106].

the apex (Fig. 7); the flow of emitted particles contains both charged and neutral droplets, as well as ions, excited atoms, and molecular complexes. We note that operation in the droplet mode is also possible for LMISs, including gallium ones, for which this mode is undesirable.

Recently, numerical computations of the shape of the meniscus formed at the apex of the thin tip of a capillary emitter working with [emim][BF_4] ionic liquid were done in [107]. It was shown that, in the pure ion emission mode, the meniscus is cone-shaped, although different from the classical Taylor cone, with the apex half-angle $\alpha/2 = 49.3°$.

4. Liquid metal ion sources on pure metals and alloys

Modern EHD ion sources must generate high-intensity monochromatic beams with stable parameters, ensuring the ultimate brightness and density of the ion current, form a sharply focused and mass-separated ion beam with a specified mass-to-charge ratio m/z (without impurities of ions of different masses and or charge states), be simple to fabricate and operate, and have a long lifetime. Due to their universality, reliability, high spatial resolution, emission characteristics, and the duration of sustainable operation, LMAISs are the most popular (more than 99.99%) sources used in modern industrial systems. In the framework of a single review, it is impossible to discuss all the technological characteristics and parameters of LMAISs in detail. For a closer acquaintance, we suggest Refs [2, 7, 26–31, 50, 72, 108], although this list is by no means exhaustive and can be extended. In this section, we focus on only those features, understanding which greatly facilitates selecting sources for their most effective use in modern FIB systems, given any specific problem in research or technology.

4.1 Design of liquid metal alloy ion sources

As was noted in Section 3.1, the LMAIS principle of operation is based on the balance of the electrostatic force and the force of surface tension of liquid metal [97, 98, 109–111]. Figure 8 outlines the operation of LMAISs [112]. Placed in front of the tip of a needle emitter made of a refractory metal is the extractor electrode with an orifice to output the formed ion beam. The working material is in the liquid state due to Joule heating from an electric current flow through the outputs and the reservoir of the emitter. Owing to the action of capillary forces, it wets the emitter with a thin layer and

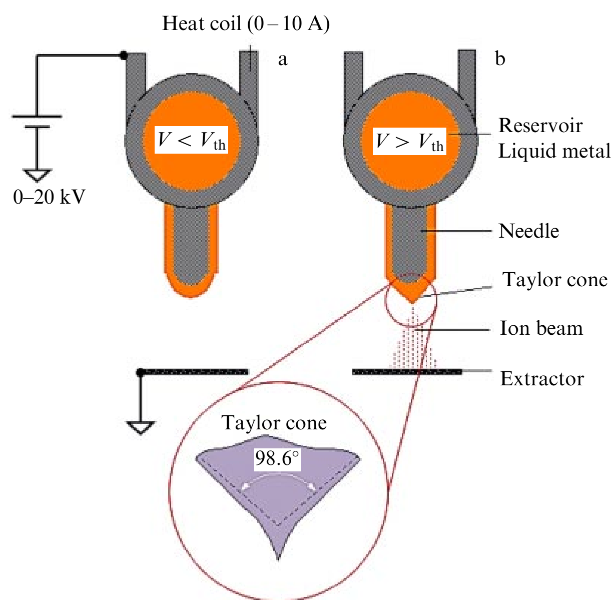

Figure 8. Schematic image of a working LMAIS [112].

flows to its tip along the lateral surface (Fig. 8a). The extractor electrode creates a strong electric field near the tip, and when the threshold voltage difference V_{th} ($\sim 10^8$ V cm^{-1}) is exceeded, the liquid metal surface takes the shape of a cone, with field evaporation of ions starting from its apex (Fig. 8b).

The use of a transmission electron microscope (TEM) with 1-MeV electron energy has allowed directly observing a Taylor cone with the full angle of 90°–100° at the tip of the needle in the course of the emission process for LMAISs working on Au, AuSi, AuGe, CoGe, CoNd, Ga, In, Sn, and Pb [113–116]. Figure 9 shows photographs of the CoNd-LMAIS needle tip shape during the emission of a 5-μA current [117] before and after the emission starts.

Various research groups have been improving the LMAIS design and technology for almost half a century. A detailed description of the LMAIS fabrication process is available in fundamental reference materials and original papers (see, e.g., [14, 26, 31]). We want to draw the attention of the reader to some special issues in LMAIS technology.

In Fig. 10, we show the evolution of LMAIS design [14]. Fabricating thin metal capillaries turned out to be a rather complicated technological process. With a small diameter of the capillary, the tip from which the emission mainly occurs

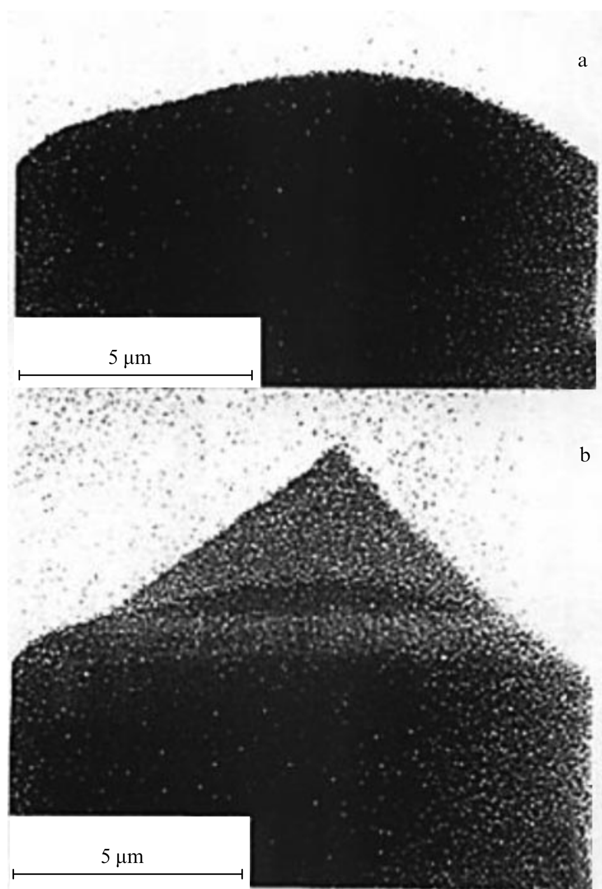

Figure 9. Formation of a Taylor cone upon CoNd-LMAIS EHD emission: (a) before and (b) after the start of emission. Photographs are taken with a TEM with the electron energy of 1 MeV [117].

can travel over the surface of the bulging droplet, which leads to an increase in the effective size of the emitter and instability of the emission. The Clampitt source design proved successful [47], with the emission domain localized on the tip of the needle protruding through the open end of the capillary and the melt flowing to the emission zone along the lateral surface of the needle. Afterwards, various needle designs of EHD sources were developed (see Fig. 10).

Versions of the LMAIS design in modern industrial devices are shown in Fig. 11. The fabrication of such sources consists of three main stages: mechanical assembly or spot welding, tip formation by electrochemical etching or mechanical polishing, and, in a high vacuum, wetting the emitter by dipping into a crucible with the melted alloy.

To fabricate a reliable and durable source generating ions of some specified chemical elements, the following important questions must be answered first: (1) what is the melting temperature T_m of the alloy, (2) what chemical compounds can be used in that alloy to decrease its melting temperature, (3) is the pressure of saturated vapor at T_m sufficiently low to avoid thermal evaporation of the alloy, (4) is the content of the relevant element in the alloy sufficient for its subsequent use, (5) are chemical reactions possible between the alloy and the material of the emitter needle at the working temperature of the source, (6) what is the viscosity of the alloy and can it efficiently wet the surface of the emitter, (7) what are the surface tension coefficients and the ionization potentials of chemical elements in the alloy, (8) can the desirable ions be separated from the undesirable ones by their mass and charge state? Most of these question can be answered by studying basic elements of the theory of alloys [118], the relevant phase diagrams [119–121], tables of saturated vapor pressures [122–124], and of surface tension and viscosity coefficients of chemical elements [125]. The thermodynamic, structural,

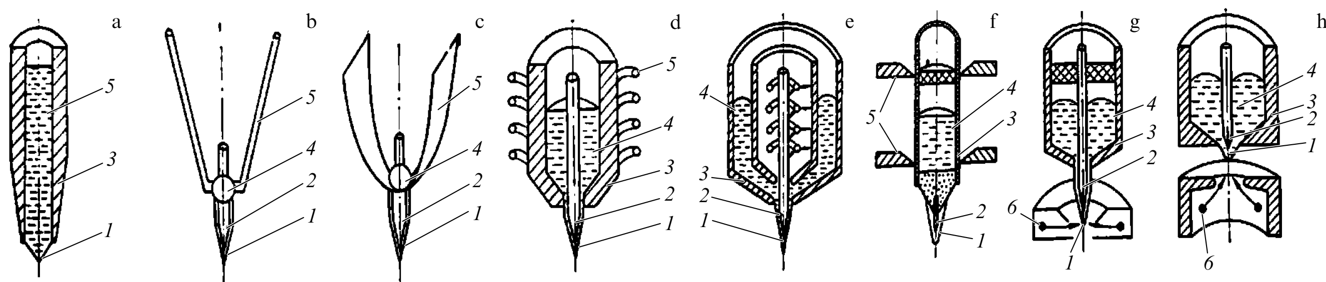

Figure 10. Examples of different LMAIS designs [14]: (a) capillary emitter and needle emitters: (b) with a hairpin, (c) with a ribbon heater, (d) with a standard container, (e) with heating by electron bombardment, (f) with a porous reservoir, (g) with a ring emitter of electrons, (h) with a ring emitter of electrons of the opposite flow. Notation: *1* — ion emitter, *2* — needle, *3* — container, *4* — working material, *5* — heater, *6* — electron emitter.

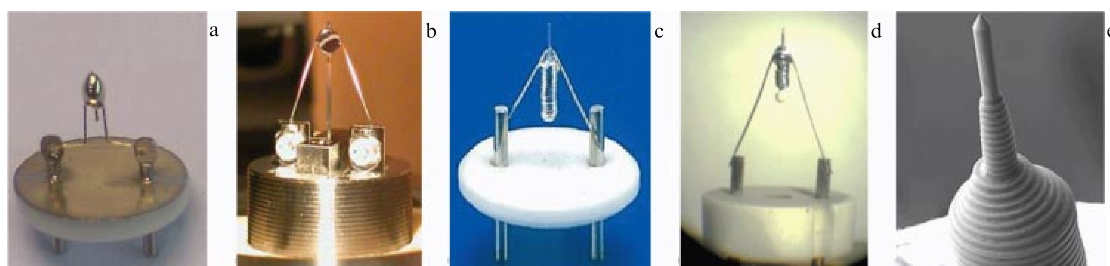

Figure 11. Design of LMAISs used in modern industrial devices manufactured by different companies: (a) AuGeSi (HZDR, Germany), (b) AuSi (Raith GmbH, Germany), (c) Ga (Denka, Japan, and Thermo Fisher Scientific, USA), (d) AuDySi (RUB, Germany), (e) Ga (Orsay Physics, France) [2].

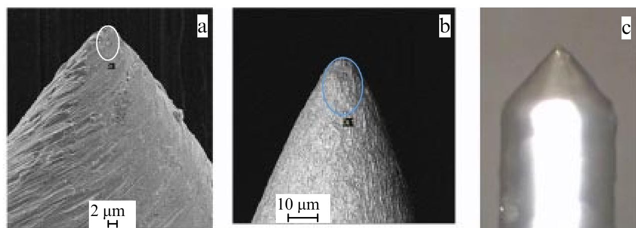

Figure 12. Needle for LMAISs: (a) mechanically polished rough needle with helicoidal grooves, (b) rough needle after electrochemical etching, (c) needle polished by electrochemical etching [131].

and diffusion properties of liquid metals are discussed in detail in [126] in relation to computer simulation methods.

Of special importance in designing LMAISs is the shape of the emitter tip, because its size and type essentially determine the emissive and technological features of the source [127, 128]. In capillary emitters, the liquid flows within a relatively thick capillary, and therefore just a small negative pressure in the Taylor cone suffices to ensure its supply with the working liquid in such emitters. But capillary emitters turn out to be much less stable than needle emitters, because the liquid column in a capillary often breaks into parts [129]. The working alloy must not interact chemically with the needle, which means that a low solubility of this alloy in the material of the needle and a low solubility of the material of the needle in the alloy must be ensured simultaneously. Therefore, depending on the working alloy in an LMAIS, modern needle emitters are made of wires of various metals (W, Re, Ta, Mo, Ni, Ti, Fe, NiCr, V, Nb, and Pt), which require dedicated processing methods, either mechanical or electrochemical. Mechanical thinning of the needle tip and the production of grooves are achieved by automated polishing on a diamond blade. Electrochemical etching of needles made of different metals is achieved in suitable chemical solutions with different methods, described in detail in [130].

Etching in the alternate current mode yields rough needles with grooves about 1 μm in depth extended along the surface, and etching with the use of direct current produces needles with mirror-smooth surfaces (Fig. 12) [131]. The flow of the liquid to the Taylor cone proceeds differently in these cases. With rough needles, liquid flows to the tip along the grooves due to capillary forces, practically without hydrodynamic impedance. In the vicinity of the reservoir, grooves are filled with liquid and the pressure in them is equal to zero; near the tip, the grooves can be almost empty, with the pressure $|p| = \gamma/r$, where γ is the surface tension coefficient and r is the radius of a semicylindrical groove. Due to the difference in pressure, the liquid flows to the tip. It was shown in [51, 52] that the grooves on a typical needle ensure the flow of the liquid to the Taylor cone by large margins. Sources with the needle made of porous tungsten infiltrated with the working material have been developed for work with even higher currents, up to 800 μA, and for better flow [132–134]. For a mirror-smooth needle, the flow rate is strongly bounded. The melted liquid flows under the action of the so-called 'splittering' pressure [135], which occurs in liquid films below 10 nm in thickness, because the formation of such films is disadvantageous from the energy point of view. An exact computation of the flow in that case is complicated by the absence of data on the splittering pressure magnitude for metals, but it is obvious that the hydrodynamic impedance of smooth needles must be much higher than that of grooved needles.

Li	Be												B	C	
Na	Mg												Al	Si	P
				Ti	V	Cr	Mn	Fe	Co	Ni	Cu	Zn	Ga	Ge	As
Rb			Y							Pd	Ag	Cd	In	Sn	Sb
Cs										Pt	Au	Hg		Pb	Bi
		La	Ce	Pr	Nd		Sm	Eu	Gd	Tb	Dy	Ho	Er	Tm	
					U										

Figure 13. Table of elements whose ions are obtained in modern LMAISs (shown in red) [2].

4.2 Review of the existing liquid metal alloy ion sources

The 48 chemicals elements whose ions have been obtained in LMAISs are shown in red (dark) in the periodic table of elements in Fig. 13 [2, 136]. A relatively recent addition to them was furnished by yttrium [137]. The most detailed list of existing LMAISs is provided in [2] together with numerous references to the publications of developers and manufacturers of these instruments and to the original papers, giving a detailed technological description for each source and alloy. As can be seen from the table, researchers and developers are especially interested in the use of light and heavy metals, semiconductors, and ferromagnetic and rare-earth elements in LMAISs. Understandably, gases and radioactive metals are not suitable for use in LMAISs. The remaining yellow squares may be filled in the coming decade.

4.2.1 LMISs on low-melting metals. Initially, only the low-melting metals shown in Table 2 were used as working material in LMISs [2]. A major drawback of most of these metals was the high pressure of saturated vapor at the working temperature, which is typically several tens of degrees higher than $T_{\rm m}$.

Table 2. LMIS sources on pure metals [2].

Ion mass	Metal	$T_{\rm m}$, °C	T, °C, at $p=10^{-5}$ Pa	Ions in mass spectrum
7	Li	181	260	Li^{++}, Li^+_{1-7}
23	Na	98	95	Na^+_{1-11}
27	Al	660	745	Al^{++}, Al^+_{1-4}
28	Si	1410	1055	Si^{++}, Si^+_{1-8}
70	Ga	30	615	Ga^+
73	Ge	938	840	$Ge^{+,++}$, Ge^+_{2-11}
85	Rb	39	15	Rb^+_{1-9}
115	In	157	525	$In^+_{1,2,3}$
119	Sn	232	730	Sn^{++}, Sn^+_{1-7}
133	Cs	28	−2	Cs^+_{1-3}
197	Au	1064	875	$Au^{+,++}$, Au^+_{2-5}
201	Hg	−39	−55	
207	Pb	328	375	Pb^+_{1-6}, $Pb^{++}_{1,3,5}$
209	Bi	271	360	$Bi^{+,++,+++}$, $Bi^{++}_{3,5,7,9}$, Bi^+_{2-7}
238	U	1135		U^+, U^+_2, U^{4+}_3, U^{2+}, U^{3+}

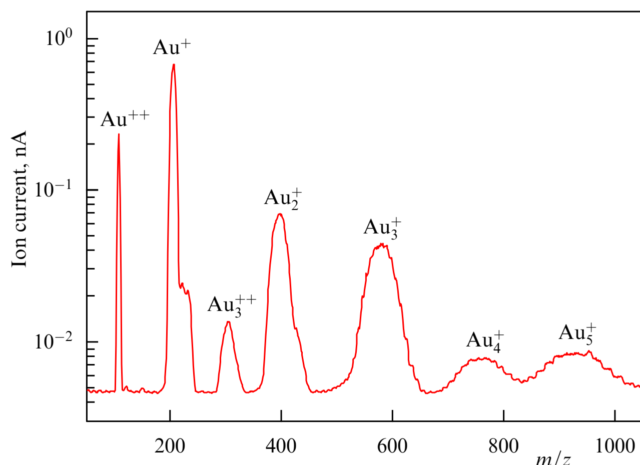

Figure 14. Mass spectrum of an Au-LMIS ion beam [2].

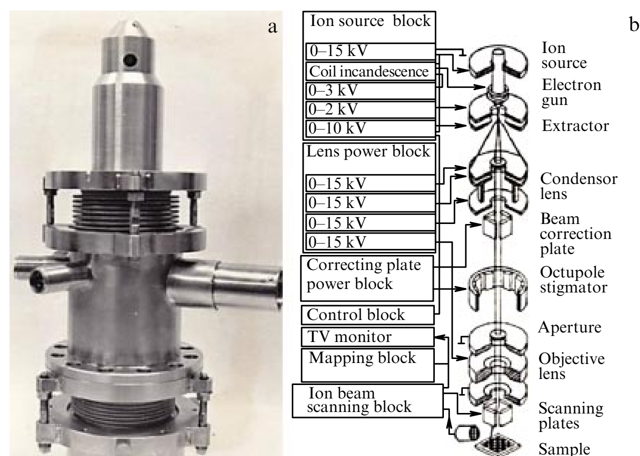

Figure 15. Gallium ion gun developed at the NITI: (a) general view, (b) functional schematic [141, 142].

At the same time, the main advantage is that LMISs can work without a mass separator, although an analysis of mass spectra (see, e.g., data for a gold LMIS presented in Fig. 14) reveals the existence of double-charged and cluster ions in the generated ion beam. The presence of such ions, which are not chemical impurities, considerably worsens the beam shape and increases its diameter. We note that a larger fraction of clusters (up to 50% of the general composition) has been found in LMISs of most of the other, nonlow-melting, metals. The 'purest' LMIS, having only single-charged atomic ions in its composition, is the gallium LMIS. But even in this case, the use of a high-resolution high-sensitivity time-of-flight mass spectrometer has allowed detecting cluster ions containing up to 25 gallium atoms [138–140].

Practical use in modern technologies is enjoyed by LMISs with only four pure metals: Ga [141, 142], In [20, 143], Bi [144–146] and, partway, Au [147, 148]. The other sources are mainly of academic interest and have insignificant technological value because of the difficulty in fabrication and/or a short lifetime. The most popular LMIS with an ideal history of practical use is the gallium LMIS, which has a low T_m, exhibits an absence of undesired ions in the generated beam, and stands out from other LMISs due to its high stability, efficiency, and extended lifetime, almost unaffected by the evaporation of gallium.

As an example of a domestic LMIS design, Fig. 15 shows a gallium ion gun built in the late 1980s at the Nauchno-Issledovatel'skii Tekhnologicheskii Institut (NITI, Ryazan) [141, 142].

4.2.2 LMAISs based on two-component alloys. The desire to extend the variety of generated ions has resulted in the fabrication of LMAISs. The normal operation of such a source requires that the alloy with a doping element should be in the melted state at a sufficiently low temperature, wet the needle well, and still have a sufficiently low pressure of saturated vapor. This set of requirements complicates obtaining ions of doping elements [28, 149– 151]. Used most frequently are eutectic alloys based on noble metals such as gold, platinum, and palladium. The necessary second element, which is the rationale behind the LMAIS, is to be chosen depending on the problem at hand.

Eutectic amorphous metals (metallic glasses) $Au_{82}Si_{18}$ [152–157] and $Au_{73}Ge_{27}$ [108, 152, 158, 159] were among the

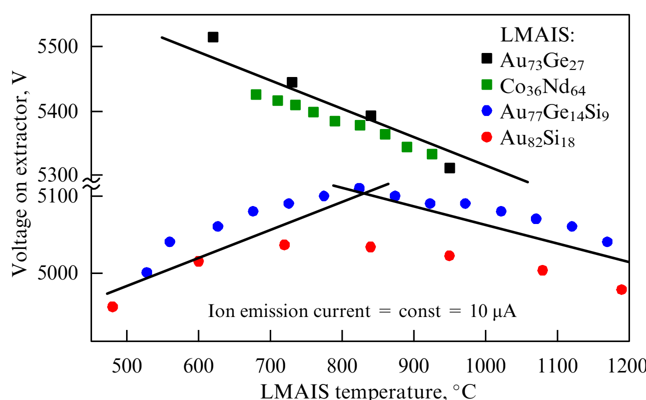

Figure 16. Dependence of the extracting voltage measured on the extractor electrode on the LMAIS temperature [158].

first alloys used in LMAISs and are still being used. These materials have an excellent track record due to their low melting temperature T_m (about 365 °C), low pressure of saturated vapor, good wettability of the tungsten emitter, and relative simplicity of fabrication. Perhaps a single significant drawback of the $Au_{82}Si_{18}$ alloy is the anomalous behavior of its surface tension, which increases at temperatures up to approximately 800 °C [2]. In Fig. 16, we show the dependence of the extractor electrode voltage on the LMAIS temperature [158]. The increasing part of the curve, corresponding to low-entropy states of the system, is due to crystal order within the first several surface layers of the liquid [160]. But at sufficiently high temperatures, this residual order is destroyed and surface tension returns to the standard monotonic decrease with temperature, thereby increasing the ion emission of the source. As regards the $Au_{73}Ge_{27}$ alloy, its surface tension decreases as the temperature increases, as is the case with the vast majority of known metals and alloys. The main drawback of that alloy is that, at temperatures above 650 °C, a chemical reaction of germanium with the tungsten emitter begins, leading to rapid destruction of the source. This behavior of both LMAISs must be taken into account in their fabrication and in working with them.

A detailed description of other technologically important LMAISs with two-component alloys is available in review [2] and the references therein. Fabricating sources with such alloys

typically faces major difficulties. For example, phosphorus and antimony start sublimating prior to melting, and the melts of aluminum actively interact with almost all materials and rapidly dissolve the details of the sources, whereas boron and carbon compounds are too hard to melt. Pure carbon in the form of graphite or other allotropic modifications has a very high melting temperature T_m, above 3500 °C. It is possible to substantially decrease T_m by using carbon in alloys with rare-earth metals. In [161], the alloy of carbon with cerium, $C_{20}Ce_{80}$, was used to generate carbon ions. Notably, the mass spectrum of the source with this alloy, in addition to atomic and cluster ions of cerium and carbon, also exhibited aluminum ions in numbers sufficient for practical use; these ions diffused into the alloy from the ceramic melting pot.

4.2.3 LMAISs based on multicomponent alloys. If the desired ions cannot be produced with a pure metal or a two-component alloy, three-component and occasionally multicomponent alloys are used. State diagrams for ternary alloys are typically constructed graphically with the help of an equilateral (concentration) triangle, using binary phase diagrams [162]. Thermodynamic calculations of three-component alloys are given in [163] for AuSiDy as an example. The easiest way to create new alloys is to use well-studied alloys with the minor addition of the required chemical elements. For example, by adding a small amount of other elements to $Au_{82}Si_{18}$ and $Au_{73}Ge_{27}$, a number of three- and four-component alloys have been obtained, which were then successfully used in LMAISs [2, 136]. If the proportion of such impurities is no greater than 5–10 at.%, the value of T_m remains practically unchanged for the resultant alloy. AuSi eutetics were used to produce LMAISs with rare-earth metals Y, La, Ce, Pr, Sm, Eu, Gd, Tb, Dy, Ho, Er, and Tm, and also Li, Be, Zn, and Sb [2, 136, 137].

In Fig. 17, we show the mass spectra of rare-earth metals Y, Er, and Gd, emitted from an alloy based on the $Au_{82}Si_{18}$

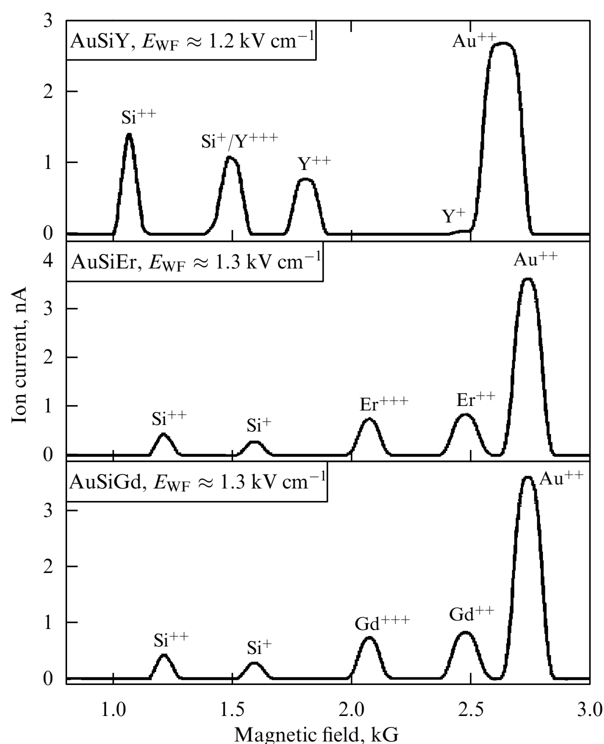

Figure 17. LMAIS mass spectra of rare-earth metals Y, Er, and Gd [137].

Table 3. Universal LMAIS [164].

LMAIS	T_m, °C	Ions in mass spectrum	Mass range, amu
$Ga_{35}Bi_{60}Li_5$	222	$^6Li^+$, $^7Li^+$, $Bi^{+,++}$, $Bi^{++}_{3,5,7,9}$, Bi^{+}_{2-7}, Ga^+	6 – 1881
$Au_{70}Be_{15}Si_{15}$	365	$Be^{+,++}$, $Si^{+,++}$, $Au^{+,++}$, Au^{+}_{2-5}	9 – 985
$Au_{77}Ge_{14}Si_9$	365	$Si^{+,++}$, $Au^{+,++}$, Au^{+}_{2-5}, $Ge^{+,++}$	28 – 985

eutetics [137]. Interestingly, the rare-earth metals, unlike other chemical elements, exhibit conspicuous peaks of triple-charged ions, thereby extending the energy characteristics of the initial ion beam. Based on the AuGe eutetics, LMAISs with the ferromagnetic elements V, Cr, Mn, Fe, Co, and Ni, as well as B and Ag, have been obtained [2, 136].

Recently, interest has been growing in using universal LMAISs that allow obtaining ions with a wider range of masses [164]. In the ideal case, a universal LMAIS must generate ions of all chemical elements and their clusters with different charge states. But in that case, besides the fabrication hurdles described in Section 4.1, it is impossible to separate the ions, and ion currents turn out to be so low that their use would be of no practical merit. Therefore, we understand universal LMAISs as sources that can generate light, medium-mass, and heavy ions in sufficient numbers, and can also work reliably and sustainably for no less than 1000 h. In Table 3, we list universal LMAISs with the best track record.

Following the refusal of many researchers to use high-fidelity $Au_{70}Be_{15}Si_{15}$-LMAISs due to the high toxic level of beryllium, while in the range of light masses $Au_{77}Ge_{14}Si_9$-LMAISs turned out to be limited to silicon ions, good prospects are envisaged for the GaBiLi-LMAIS [165, 166]. Lithium is the lightest and bismuth the heaviest nonradioactive metal in the periodic table. Besides heavy clusters, such an EHD source is capable of generating ions in the range of 6–1881 amu (Fig. 18a), and the ions can be reliably separated in a standard ion column and then used for submicrometer lithography and nanoanalysis.

The use of ions of different masses in a single source with a time interval of less than one minute for switching over between them has a number of advantages. For example, at the accelerating voltage of 40 kV, the sputter yield on gold with lithium ions is $Y = 0.3$, which is 100 times lower than with bismuth ions (Fig. 18b). Given the mass relations $270m_{Li} = 27m_{Ga} = 9m_{Bi} = 3m_{Bi_3} = m_{Bi_9}$ in that source and nonlinear effects of sputtering with heavy clusters of bismuth, we can expect a 20-fold increase in the sputter yield with double-charged bismuth clusters of nine atoms. Simultaneously, under bombardment of the surface, light ions penetrate into the substrate much more deeply than heavy ions and clusters do. In Fig. 19, we show the results of simulations with the help of the TRIM software for the penetration depth of Li, Ga, Bi, and Bi_3 ions with an energy of 35 keV into an Si substrate [168]. In turn, light ions considerably increase the yield of secondary electrons, have practically no destructing effect on the surface, and are actively used in ion microscopy, where they allow attaining the optimum focusing of the beam [164].

Other multicomponent LMAISs are broadly represented and described in [2] and in the references therein. Very recently, detailed investigations were performed on the fabrication and application of different alloys for the

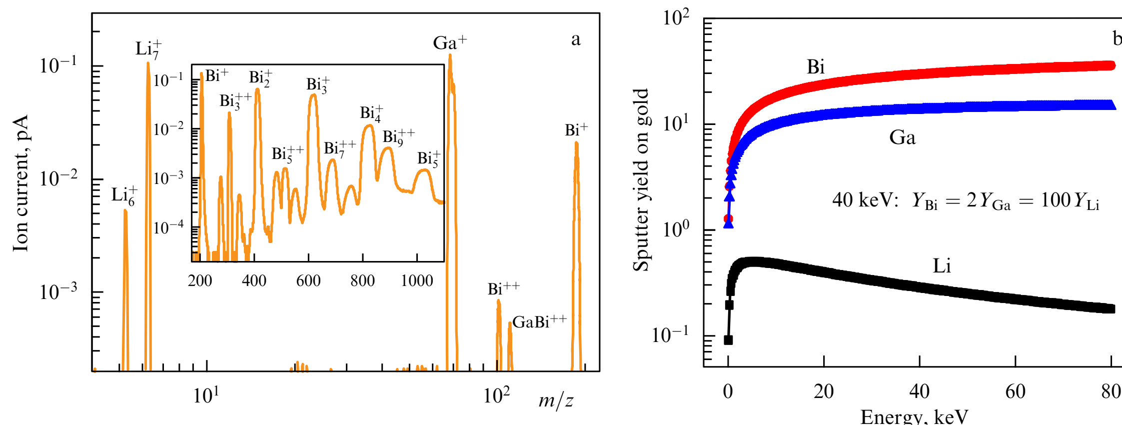

Figure 18. (a) $Ga_{35}Bi_{60}Li_5$-LMAIS mass spectrum [164], (b) sputter yield on gold with Li, Ga, and Bi ions at the energies used in FIB systems [167].

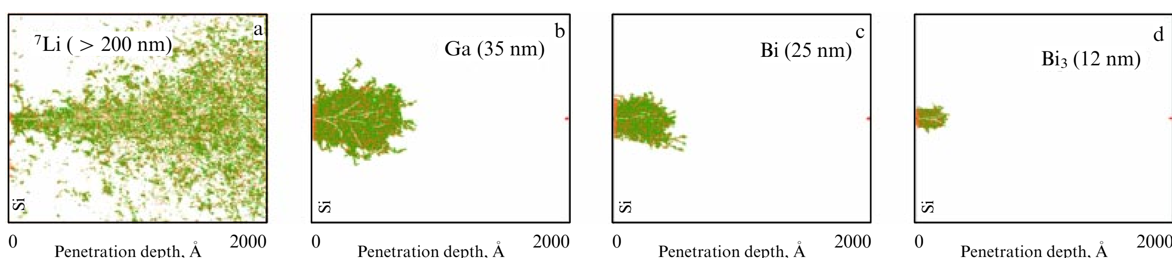

Figure 19. Computation with the TRIM software of the penetration depth of Li, Ga, Bi, and Bi_3 ions with the energy of 35 keV in an Si substrate [168].

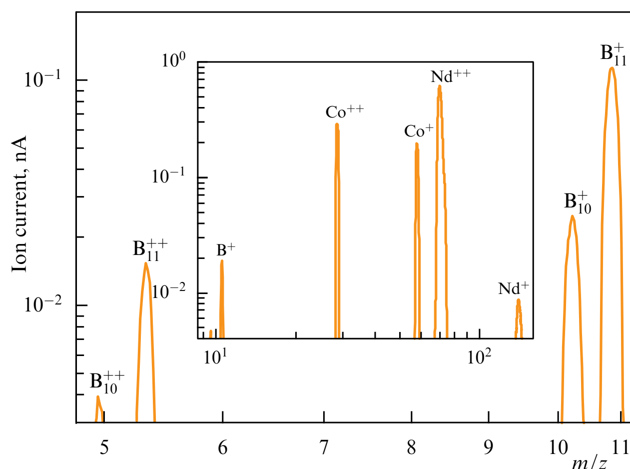

Figure 20. $Co_{31}Nd_{64}B_5$-LMAIS mass spectrum [169].

generation of boron ions in variously designed sources [169]. The $Co_{31}Nd_{64}B_5$-LMAIS turned out to be the most suitable and reliable; its ion beam mass spectrum is shown in Fig. 20, where we can see that the spectrum contains both single-charged and double-charged ions of all elements entering the alloy composition, including boron isotopes.

4.2.4 Cluster sources. Cluster ions are typically understood as ions of heavy elements with a possibly increased content of atoms in the cluster. As shown above, all the LMAISs apart from atomic ions emit clusters [170], but only those sources that allow producing ion beams with a high content of clusters are of interest. For example, the proportion of clusters in a Ga-LMIS is considerably less than 1% [138, 139], but in the Bi-LMIS, which is the most desirable source from this point of view, their proportion reaches 50% [144–146].

4.2.5 LMAISs for emission of electrons. Under reversal of the accelerating voltage polarity, emission of electrons from the apex of a frozen Taylor cone have been observed for some LMAISs [171–178]. Unfortunately, even though this mode is certainly of interest, it is unstable and short-lived, which does not allow considering LMAISs as sources of electrons.

4.3 Main emission and ion-optical parameters of liquid metal alloy ion sources

4.3.1 Current–voltage curve. One of the main indicators of the performance of any LMAIS is its current–voltage curve (IV), which expresses the functional dependence of the ion emission current I on the extracting voltage U applied to the extractor electrode. The correct interpretation of an IV unambiguously allows judging the suitability and reliability of an LMAIS in all of its operation modes, both after the fabrication of a source and after its long-term use. This question has always been given special attention in experimental and theoretic studies [2, 10, 27, 72, 179, 180].

According to the generally accepted Mayer theoretical model, the ion emission current for a threshold potential difference U_{min} is given by [179]

$$I = 3\pi\sqrt{\frac{2e}{m}}\,\frac{r\gamma\cos\alpha}{\sqrt{U_{min}}}\left\{\frac{U}{U_{min}} - 1\right\}. \tag{11}$$

It follows from formulas (7) and (11) that, besides voltage U on the extractor electrode, the emission current also depends on atomic mass m of the generated ions, surface tension γ of the working liquid, emitter rounding radius r, and Taylor

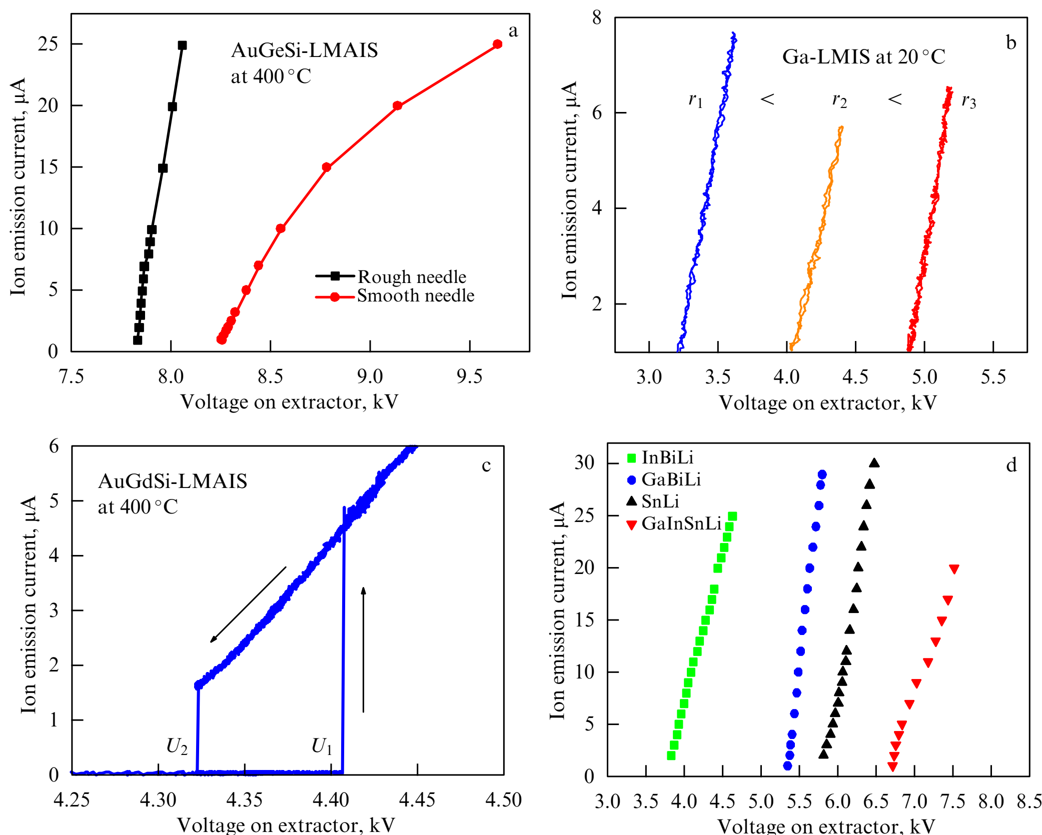

Figure 21. Current–voltage curves: (a) AuGeSi-LMAIS with rough and smooth needles, (b) Ga-LMIS with emitters of different radii, (c) hysteresis IV for AuGdSi-LMAIS (U_1 and U_2 are the voltages for turning emission off and on), (d) LMAIS with InBiLi, GaBiLi, SnLi, and GaInSnLi [131, 166].

cone angle α. Ion emission starts when the extracting voltage threshold is exceeded. As shown in Section 4.1, capillary LMAISs are not particularly interesting for industrial applications (commercialization) because of the unstable flow of the liquid along the capillary to the Taylor cone, and we do not therefore discuss them here. The character and slope of the IV of a needle LMAIS depends on the distance between the source and the extractor electrode, on the diameter of the aperture in the extractor, on the material of the emitter, and hydrodynamic impedance, which in turn depend on the roughness of the source needle (see Fig. 12). On a rough surface, the liquid film is thicker, which facilitates its flowing to the tip.

Figure 21a shows the IVs of an AuGeSi-LMAIS with rough and smooth needles. For smooth needles, the impedance strongly limits the flowing of the liquid to the needle tip, but for rough needles, because of capillary forces in the grooves, the impedance is so small that it can be disregarded, together with the second term in formula (5). Therefore, the IV slope is gentler for smooth needles. Additional factors that can change the impedance are the angle and radius of the tip (Fig. 21b) and the diameter of the needle base. The effect of the geometry of the electrodes on LMAIS IVs was studied in detail in [127].

If emission starts jump-wise at voltage U_1 [181], then it disappears at lower voltage U_2 (Fig. 21c). The hysteresis at $U_2 < U < U_1$ is explained by the fact that two stable liquid states on the tip coexist in this range: one in the form of a film and the other in the form of a Taylor cone. Formation of the Taylor cone requires a higher voltage than that needed for maintaining it. Therefore, the optimum working emission current is assumed to be the one at which the extracting voltage is greater than U_1. The larger the radius of the tip rounding, the diameter of the needle base, and the angle at its tip, the greater the magnitude of hysteresis. A substantial effect on the IV form is exerted by the physical–chemical properties the alloys, such as density, surface tension, surface free energy, sublimation heat, and the working temperature. In Fig. 21d, we show LMAIS IVs with different alloys of lithium.

4.3.2 Source lifetime. From the practical point of view, an important characteristic of an LMAIS is its actual lifetime, measured in μA h. The lifetime duration is directly proportional to the amount of material in the source and inversely proportional to the rate of its consumption. Orloff's guidelines [28, p. 63] give consumption data for some types of sources. For example, for Ga-LMISs, the material consumption is 383 μA h mg^{-1}, and for AuSi-LMAISs, 169 μA h mg^{-1}.

Disregarding container-type sources and sources for electrostatic micro-jet engines, which can contain several tens of grams of working material, we discuss only the design of sources used in FIBs. They can be conventionally divided into two types: (1) Denka/FEI (up to 15 mg of working material), used by the absolute majority of manufacturers, including Thermo Fisher Scientific Inc., Carl Zeiss AG, TESCAN, JEOL Ltd., and IONTOF, and (2) Raith GmbH (up to 100 mg of working material). The lifetime of first-type sources is $(2-6) \times 10^3$ μA h and is about an order of magnitude less than for sources of the second type.

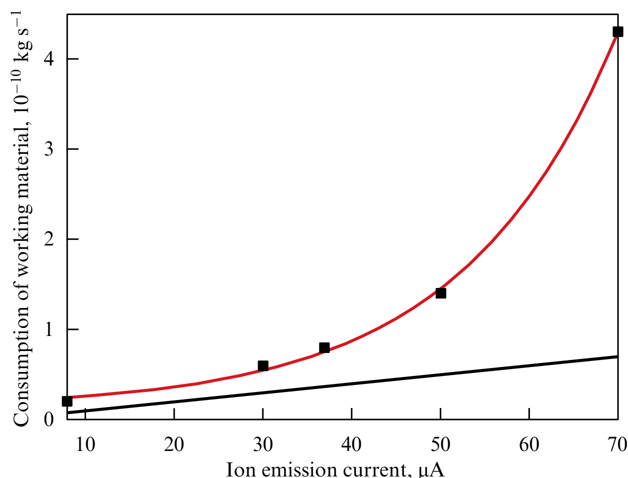

Figure 22. Consumption of working metal in a Ga-LMIS as a function of the emission current (red exponential dependence) and the calculated dependence (straight line) under the assumption that the emission current consists of single-charged atomic ions [183, 184].

The first threshold is the minimum guaranteed by the manufacturer. The absolute duration of the source lifetime expressed in hours can be increased by ensuring operation at a minimal temperature and low emission currents (not greater than 2 μA) and also by protecting the reservoir and the emitter from possible contaminations, because adsorbed material obstructs the flow of the liquid metal. In the high-current mode, local evaporation from the needle and microdroplet emission occur, the yield of clusters increases, and oscillations of the ion current occur, which considerably increases the liquid metal consumption [27, 28, 89, 109, 182]. The rate of consumption of the LMAIS working material is very difficult to determine experimentally. The lifetime can be estimated by comparative weighing of the source immediately after fabrication and after its has been worn out, keeping track of its working modes and conditions.

Figure 22, based on data in [183, 184], shows actual consumption of the working metal in a Ga-LMIS depending on the emission current and its calculated estimate when all the emitted ions were single-charged and atomic.

After long use of a source, the working material can be contaminated or worn out at the end of the needle, thereby displacing the Taylor cone sideways. Such a displacement considerably changes the working mode and the characteristics of the source, eventually leading to its unstable operation, up to the total termination of emission. The reversed inflow of material and the wettability of the needle tip can be achieved by either temporarily overheating the source or by increasing the emission current to the maximum possible value (rarely above 100 μA), or, indeed, by combining both regimes. Metal oxides typically have a higher T_m. In the case of gallium, heating to 750 °C at the tip of the needle is required for cleaning it from contamination. Because the increased pressure of saturated gallium vapor at this temperature can lead to its virtually instantaneous evaporation, the heating process must be strictly controlled. Because of a relatively massive LMAIS design, the temperature difference between the tip of the needle and the reservoir of working material can attain several tens of degrees, which leads to increased consumption of material and hence to shortening the life of the source. On average, over the entire time of operation of a source, the proportion of such nonscheduled losses can amount to half the working material mass. It is therefore important to minimize the number of times the source is heated. In addition, when overheating the source, the evaporated material is deposited on the nearby units of the ion column, which can lead to short-circuiting. To eliminate contamination of the liquid metal, it is recommended to maintain the pressure in the source chamber below 5×10^{-6} Pa and prevent the extractor electrode material sputtered by the ion beam from entering the alloy. Accordingly, if an LMAIS is not used, it should be stored in high vacuum or in an atmosphere of dry nitrogen or an inert gas.

4.3.3 LMAIS stability. Temporal stability is a factor determining LMAIS performance. The physical foundations of LMAIS stability, which must satisfy very high demands, have been actively investigated and discussed in many papers [2, 26–31, 128, 185–188]. The minimal emission current (below which the source shuts down due to the loss of dynamic stability of the liquid–vacuum interface) has been determined for many sources and lies in the range of $\sim 0.1-1$ μA [189–191]. It is assumed that, depending on the magnitude of the emission current, LMAISs have several EHD stability modes, such that the ranges defining them vary little for different alloys and variations in the emitter design. We select five ranges, which in our opinion characterize the behavior of the majority of LMAISs most precisely: (1) low-current instability mode, in which the ion emission is either absent or terminates periodically (0–1 μA), (2) stable mode in ideal conditions (1–2 μA), (3) maximum stability mode (2–15 μA), (4) stable high-current mode (15–40 μA), and (5) unstable high-current mode (40–200 μA). Emission with ultra-high currents, in excess of 200 μA, is possible, in principle, but has been poorly investigated.

In addition to the restrictions imposed on the stability of an EHD source by the emission processes in and of themselves, a very substantial effect is exerted by the following processes and factors: type of needle; working temperature; contamination of the source with material oversputtering from the extractor electrode and other surfaces; vacuum conditions in the working chamber; high-speed electrons bombarding the emitter; sustainability and stability of high-voltage power sources; existence of a suppressor electrode in the extraction block; computer software controlling the operation of a source. By taking all these factors into account, a high stability of even the most difficult and 'finicky' sources can be ensured. In Fig. 23, we show the time dependence of the emission current of a GaBiLi-LMAIS at the accelerating voltage of 40 kV and the lithium current on the target for 16 h of uninterrupted work. The emission current was measured every second, and the lithium ion current on the target was measured every 10 s.

4.3.4 Source brightness and angular intensity of the ion current. Other very important and mutually complementary characteristics setting the limits to ion beam focusing in EHD sources are the angular intensity $J_\Omega = I/(\pi\alpha^2)$ (ion current within a single solid angle) and the source brightness B_r, which is generally understood as the ion current emitted from a single area into a single solid angle:

$$B_r = \frac{J_\Omega}{(\pi/4)d_q^2} = \frac{d^2 I}{d\Omega_1\, dA_1}\,, \tag{12}$$

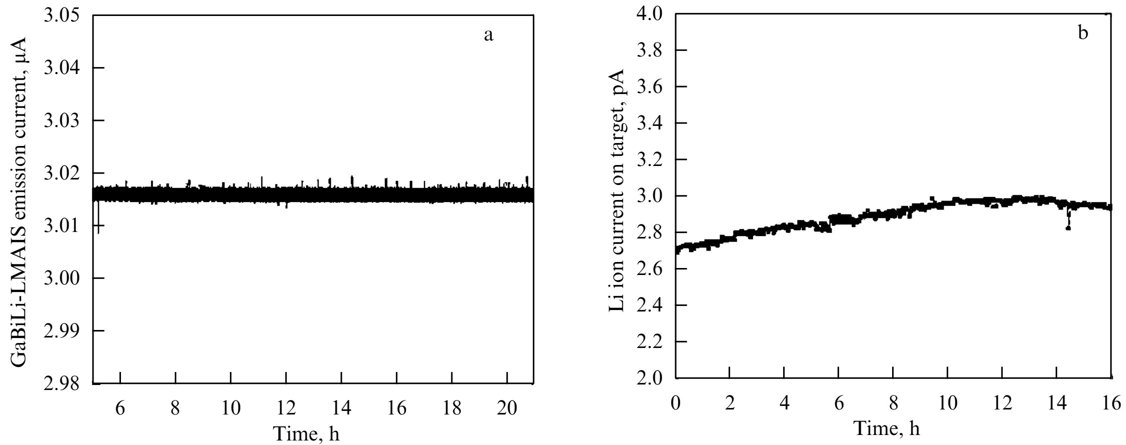

Figure 23. (a) GaBiLi-LMAIS emission current at the accelerating voltage of 40 kV and (b) lithium ion current on the target [164, 166].

where I is the ion emission current, α is the angle, d_q is the virtual (imaginary) size of the source, Ω_1 is the solid angle, and A_1 is the transverse cross section of the beam at the exit from the source.

To compare different sources independently of the ion accelerating voltage U, the notion of normalized brightness is introduced as

$$\beta_1 = \frac{d^2 I}{d\Omega_1 \, dA_1 U} \,. \tag{13}$$

If only conservative forces are present in the system, then, in accordance with the Liouville theorem, the brightness β_2 at the focused spot is equal to the brightness of the source:

$$\beta_1 = \frac{d^2 I}{d\Omega_1 \, dA_1 U} = \frac{d^2 I}{d\Omega_2 \, dA_2 U} = \beta_2 \,, \tag{14}$$

where the subscript 2 refers to the focused beam.

It has been shown experimentally that the angular divergence of the beam increases as the emission current and the mass of the emitted particles increase, and J_Ω and B_r decrease as the mass increases as $m^{1/2}$. LMAIS brightness has been estimated and measured by many researchers, and it is currently regarded as determined sufficiently precisely, at least for Ga-LMISs [192, 193].

Under field evaporation, energy spread of ions is determined by quantum effects occurring when the electrons break away, and amounts to $\Delta E \sim 4.5$ eV [26]. Knowing the emission current density of gallium ions $j_o \sim 10^8$ A cm^{-2}, a typical virtual source size of the order of 45 nm, and its emission area $A_1 = 1.6 \times 10^{-11}$ cm^2, we obtain the normalized LMIS brightness of the order of 10^6 A m^{-2} sr^{-1} V^{-1} for an accelerating voltage of 30–40 kV and emission current of 1–5 μA.

By the end of the 20th century, LMAISs had the highest brightness among all the ion sources in use. Table 1 lists modern highest-brightness ion sources. Only with the appearance of GFIS and MOTIS sources at the turn of the century did LMAISs experience real competition. We note, nevertheless, that GFISs are essentially limited by the magnitude and stability of the current, and MOTISs have not yet found application due to their complex design and control. In addition, LMAISs extend the total scope of GFISs and MOTISs severalfold as regards the choice of ions [2].

4.3.5 Accelerating voltage and the total ion current. As shown in Section 2.2, a decisive role in forming and optimizing an ion beam is played by the ion column design and the choice of the ion source. In what follows, we discuss ion-optical LMAIS parameters that can substantially restrict the focusing and the diameter d of the ion beam. These include the accelerating voltage and the total ion current, the virtual size of the source, and energy spread of the ions. Coulomb repulsion forces acting between ions strongly deflect their trajectories from the optical axis, producing a divergent ion beam. The ions are accelerated to the final energy in the gap between the extractor electrode and the first electrode of the condensor lens. Passing through the column, a major part of the ion beam (90–100% of the ion current) is lost on the intermediate electrodes and apertures. In the best-case scenario, industrial FIBs ensure a current of the order of 50–100 nA at the exit from the column at the accelerating voltage of 30–40 kV and emission current of 1–10 μA. Using the maximum possible energies offers several advantages: better focusing due to reduced chromatic aberration (Section 3), a higher sputter yield (Section 6), and more current through the column (Fig. 24). The most important conditions for optimizing ion-optical systems are the exact positioning of the emitter on

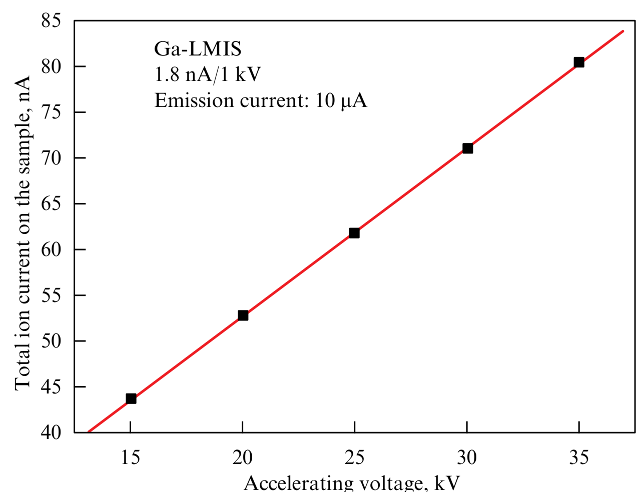

Figure 24. Dependence of the total current of gallium ions at the exit from the column on the accelerating voltage [131].

the optical axis and the possibility of ion emission strictly from the tip of the needle. Displacement of the emission point considerably changes the ion-optical properties in the extractor zone, which itself is a weak immersion lens, and the ion column overall, which leads to degradation of the beam shape and a loss of total ion current. In many industrial systems, this effect is partially eliminated by introducing a suppressor electrode [194], but in systems without it, changes in ion-optical properties are practically inevitable.

4.3.6 Virtual (imaginary) size of the source. In an ideal ion column, in the total absence of all aberration and astigmatism (which is only possible hypothetically), the minimal size of the ion beam in the focus plane is directly proportional to the size of the source $d = Md_{\mathrm{q}}$, where M is the optical magnification of the ion column. As the aperture angle of the beam decreases, chromatic aberration becomes less and less apparent, and the virtual LMAIS size starts playing a role. The LMAIS virtual source size (the size of the disk from which the ions are emitted) depends on the mass of the original material, $d_{\mathrm{q}} \sim (m^{1/2} I)^{0.45}$ [195], and amounts to 20–50 nm, which is 5 to 10 times greater than the physical size of the emission spot. Possible reasons are the sideways motion of the liquid jet and the effect of space charge, which changes the trajectories of the ions. Backtracking the trajectories outside the strong Coulomb interaction domain near the source shows that ions are emitted from a virtual source with a diameter much greater than that of the physical source. Theoretical discussions on the displacement of ion trajectories in LMAISs and numerical model results that are consistent with experimental data are given in [196, 197]. Measurements of the virtual size of the source were conducted in [198], with the virtual size taken to be equal to the diameter at which the source brightness decreases two fold compared with the brightness in the center. Numerical computations of the virtual size magnification were performed in [196], and analytic calculations were done in [199], with the analytic result differing from numerical ones and showing a much better agreement with experiment. Figure 25 shows the results of estimating the virtual source size based on the theory of trajectory displacements [195] for ions of different masses at the ion emission current $I = 1$ μA.

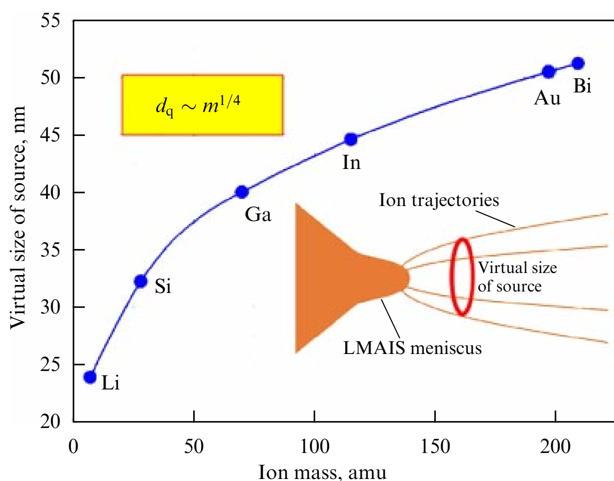

Figure 25. Dependence of the virtual size of a source on the mass of emitted ions [2].

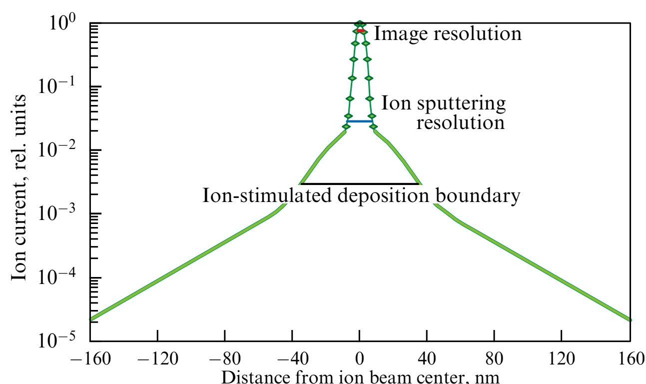

Figure 26. Current density distribution in an ion beam [207].

Quite significant also is the focused beam profile on the target. Measurements made by the authors of [200–205] show that the ion current density distribution in the beam remains Gaussian up to intensities three orders of magnitude lower than the maximum, but after that the intensity decreases much more slowly with the radius. This effect can be explained by the mutually repellent interaction of ions in the beam [196] and their scattering on atoms and molecules of residual gas [206], and also by chromatic aberrations of cylindrical lenses for ions from the tails of the energy distribution function [200]. It was hypothesized in [205] that, as the beam intensity decreases, chromatic aberration starts playing a role, and only at very small intensities does the scattering on residual gas dominate. In Fig. 26, we show the ion current density distribution on the target [207].

4.3.7 Energy spread. Still, when ion beams are formed in LMAISs, the main cause of the decrease in brightness is the chromatic aberration of electron lenses. Its magnitude is proportional to the energy spread ΔE (formula (2)), which is equal to the work spent to create an ion on the surface of a solid body or a liquid in an electric field. Under field evaporation, ΔE increases owing to the interaction of ions in a dense beam, which stimulates heating along the direction of the longitudinal degree of freedom due to the potential energy of inter-ion interaction [199], and cooling along transverse degrees of freedom as a result of ion collisions (the Boersch effect [208]), thereby decreasing the original brightness of the beam. When focusing a beam of ions with such energy spread, electrostatic lenses distort its shape, such that ions in the center and at the edges of the focused beam have different energies. As shown in Fig. 27 the greater ΔE is the wider the chromatic aberration spot.

Experimental studies and theoretical justification of the energy spread ΔE of ions in LMAISs is the subject of a large

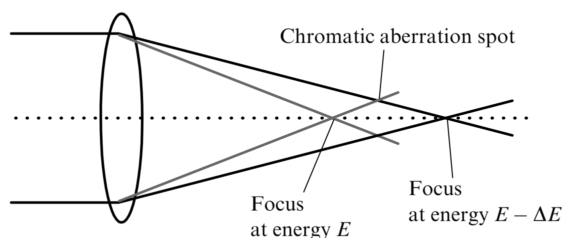

Figure 27. Schematic image of a chromatic aberration spot.

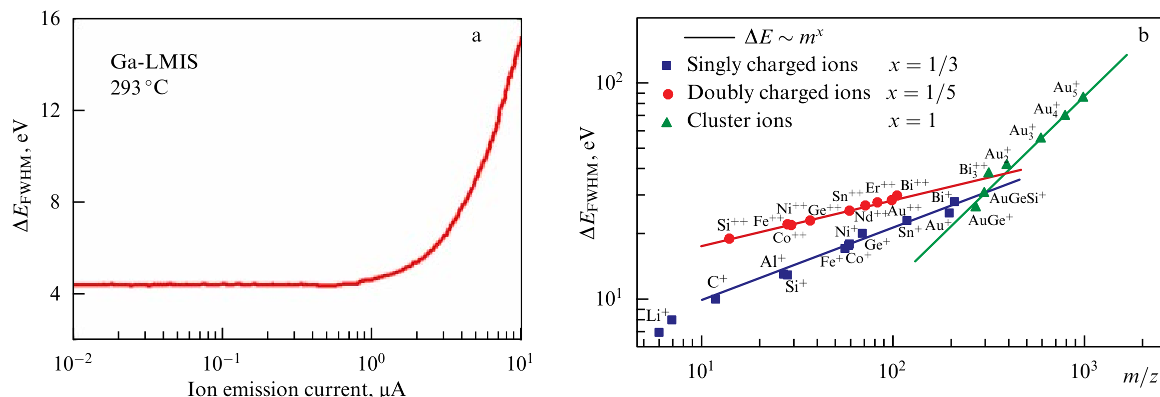

Figure 28. (a) Dependence of the energy spread width (FWHM) for a gallium LMIS on the emission current at room temperature [212], (b) dependence of energy spread of singly and doubly charged atomic and cluster ions with the emission current 15 μA on the ion mass [2, 218].

number of studies [83, 87, 209–215]. We wish to draw the reader's attention to the dependence of ΔE on the emission ion current I, the ion mass m, and the LMAIS temperature T. These dependences play a decisive role in selecting the working alloy and optimizing working conditions for a source with the aim to decrease chromatic aberration and the ion beam diameter [199, 214]:

$$\Delta E \propto T^{1/2} I^{2/3} m^{1/3} \,. \tag{15}$$

The temperature dependence of ΔE has been studied for various LMAISs [99, 214–217]. The working temperature typically exceeds the melting temperature of the alloy by 10–100 °C, and its level is insignificant in the energy equivalent. The dependence of ΔE on I is also studied well [83, 209, 212]; an example of a gallium LMIS at room temperature is shown in Fig. 28a [212]. We can see that, at small currents, energy spread stops decreasing, which is consistent with the conjecture of a minimal ion current necessary for maintaining stable emission. The dependence of ΔE on m is based on long-term experimental investigations of different sources by Bischoff's group in Dresden [2, 218]; the results are shown in a single plot in Fig. 28b. The experimental installation and the method of measurement are described in detail in [108]. In addition to atomic ions, ΔE was also measured for some doubly charged ions, and, consistently with the data of other authors [219, 220], it was shown that

$$\frac{\Delta E\,(m^{++})}{2} < \Delta E\,(m^{+}) < \Delta E\,(m^{++}) \,. \tag{16}$$

Thus, at the same accelerating voltage, chromatic aberration for double-charged ions is less than that for single-charged ones. The dependence of ΔE on m for clusters has a linear character, and therefore focusing heavier cluster ions is fraught with considerable complications. For example, if a beam of lithium ions from an LMAIS can be focused on a spot 2 nm in radius, the radius of a beam of bismuth clusters with five atoms already exceeds 100 nm [164].

5. Ion sources with room temperature ionic liquids

As already noted in Section 1.2, ionic liquids consist of organic cations $[R]^+$ and organic or inorganic anions $[A]^-$. In accordance with modern theoretical and experimental ideas (see, e.g., [24, 221, 222] and references therein), ionic liquids are complicated nanostructured fluids consisting of polar and nonpolar domains with ordered structures: domains, ion pairs, quasimolecular packings, and associates. In review [60], the sources of ions based on ionic liquids were called electrolytic. In our opinion, this is somewhat of a misnomer, because, in the general case, electrolytes include materials that conduct electric current due to dissociation into ions in a melt or solution (translated from the Greek, *electrolyte* literally means 'decomposable by electricity'), whereas ionic liquids can exhibit their ionic nature without electric current running through them.

More than ten thousand different ionic liquids are currently known, and the successful synthesis of new compounds is underway [223]. Many of them are suitable for generating ion beams, of both positive and negative polarity, with different masses, including in excess of 5000 amu. At present, the ionic liquid most frequently used in ILISs is EMI-BF_4, whose composition involves imidazolium — a cation of imidazol, which is an organic compound from the class of heterocycles. This liquid also bears the notation [emim][BF_4] (the polarity of the cation or the anion charge usually being omitted) or [C_2mim][BF_4]. Information on other ionic liquids that are also used for generating ion beams can be found in [60, 61].

We note that, in view of their ionic nature, ionic liquids have an extremely low pressure of saturated vapors; this allows using them even in ultra-high vacuum. They remain liquids in a wide temperature range, including at room temperature, have high thermal stability, do not deflagrate, and are low-toxic; many of them are inert to air and water. By their exterior, ionic liquids are colorless or faintly yellowish, which is due to a small amount of impurities. Presently, different ionic liquids pure at a 99.5% level or higher are produced by many companies, for example, Merck (Germany).

In many ILISs (see, e.g., [77, 224]) working in the pure ion mode, the emitters are needle-shaped electrodes made of W-wires designed for industrial FIB systems. Such an emitter is shown in Fig. 4b. In principle, most of the emitters developed for LMISs and LMAISs (see Figs 10 and 11) are suitable for ILISs, the only difference being that for ILISs there is no need to heat and melt the working material.

Ion beams of positive and negative polarity generated in ILISs mainly consist of cations $[R]^+$ and anions $[A]^-$, and also

cluster ions $\{[R]^+[A]^-\}_m[R]^+$ and $\{[R]^+[A]^-\}_m[A]^-$, where $m = 1$; the intensity of cluster ions is typically lower than that of cations and anions. However, this rule is not valid for all ionic liquids. In [225], for example, a source with a W-emitter was used to obtain the ion current with [emim][Beti], whose specific conductance (0.34 S m^{-1}) is lower than that of [emim][BF_4] (1.3 S m^{-1}). The anion $[Beti]^- = (C_2F_5SO_2)_2N^-$ with the molecular mass 380.1 amu is similar to the anion [Tf_2N]. Time-of-flight analysis has shown that, among the positive ions emitted by a source with the ionic liquid [emim][Beti], besides the cation $[emim]^+$, there were cluster ions $\{[emim][Beti]\}_m[emim]^+$ with the maximum value $m = 4$ (molecular mass 2076 amu). The intensity of cluster ions with $m = 1$ was higher than the intensity of cations. For negatively charged ions $\{[emim][Beti]\}_m[Beti]^-$, the maximum value $m = 3$ was obtained (molecular mass 1854 amu), but the intensity of emission of $[Beti]^-$ anions was higher than that for negative cluster ions. In view of such a variety of ions of both polarities, ILIS columns must necessarily be equipped with mass separators for ion beams, for example, Wien filters.

It was shown in [226] that, in the course of emission of a needle emitter wetted with the ionic liquid [emim][BF_4], this liquid undergoes degradation due to electrochemical reactions. As a result, the ion current decreases, and the operation of the source becomes unstable. The reason is that at the interface with a metal electrode, any ion liquid experiences a change in composition as a result of depletion in ions, which leads to the formation of a double electric layer preventing the displacement of ions inside the ionic liquid and causing rapid destruction of the tapered part of the emitter. A proposal to eliminate this effect consisted of alternating the polarity of the extracting voltage on the emitter at a frequency of 1 Hz. Later, in [227], a dedicated distal (peripheral) electrode fed with the accelerating voltage was used to suppress electrochemical reactions.

Besides ILISs with standard needle emitters, which are in use in FIB systems, original capillary ion sources have been constructed and tested (see, e.g., [228–230]). It was shown in these studies that, for the ionic liquid [emim][BF_4], depending on the polarity of the accelerating voltage, the ion beam composition is dominated by cations or anions with an insignificant contribution of cluster ions with $m = 1$ and products of the ionic liquid decomposition with mass numbers in the range of 20–40 amu. On the contrary, for [bmim][PF_6], which has a lower specific electrical conductivity and higher dynamic viscosity than [emim][BF_4], the cluster ions $\{[bmim][PF_6]\}[bmim]^+$ and $\{[bmim][PF_6]\}[PF_6]^-$ were dominant. The highest ion current densities at the best temporal stability of the beams were achieved for emitters made of graphite, which, due to the high wettability by the ionic liquid, ensured its stable supply to the apex of the Taylor cone. In addition, graphite is the most chemically resistant material among those used for fabricating emitters in that study.

The idea of combining in ILISs the use of a distal electrode and a porous tapered emitter, which simultaneously plays the role of a container and a system of ionic liquid supply, was realized in [231, 232]. Figure 29a schematically shows an ion source whose main parts are the needle-shaped carbon emitter located in the upper part of the electrode made of a high-porosity resorcinol-formaldehyde xerogel, a distal electrode, an insulating insertion made of fiberglass, and a cylindrical reservoir made of teflon (fluoropolymer-4). The distal electrode was also made of xerogel, and the contact electrode through which the accelerating potential is applied to the source was platinum. At the emitter apex (Fig. 29b), the needle was originally sharpened mechanically [231], and later, in [232], with an excimer laser, which allowed a smaller rounding radius ($\sim$ 10 μm) with lower roughness of the needle surface. The ionic liquid [emim][BF_4] was used as the working material in that source. The threshold potential at which ion emission starts was 1.6–1.65 kV, and the emission current was 0.45–0.55 μA.

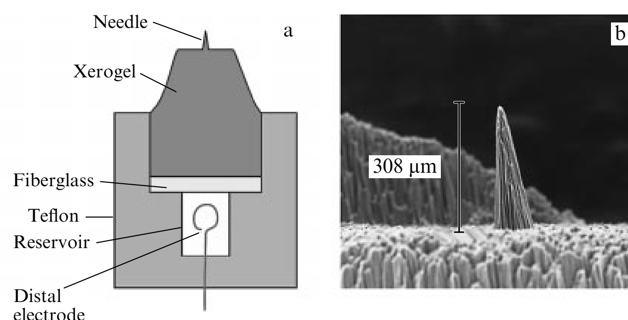

Figure 29. (a) Schematic image of an ILIS with a xerogel needle emitter, distal electrode, and teflon reservoir; (b) magnified image of the needle obtained with a scanning electron microscope (needle height: $\sim$ 300 μm, apex radius: $\sim$ 10 μm) [232].

To summarize the information on ILISs with needle emitters and distal electrodes working in the pure ion mode, we can state that, with the use of different ionic liquids, these sources are capable of generating a stable ion current of either polarity in the range from tens of nanoamperes to several microamperes at the accelerating voltage of several kilovolts in the course of hundreds of hours without noticeable degradation of the ionic liquid or destruction of the emitter tip. The ion beam, depending on the polarity, mainly consists of cations or anions, but it is also possible to obtain sufficiently intense cluster ions of a heavier mass (>1000 amu). The relaxation time of the ionic liquid, i.e., the time to attain the ready state after applying the accelerating voltage, is estimated in the range of 0.05–0.1 ns. The electric field strength at which ion emission starts from the apex of the Taylor cone is about 1 V nm^{-1} at an emission zone radius of the order of 10 nm. The brightness of needle ILISs is comparable to that of gallium LMISs, and energy spread of the emitted ions in duly selected modes of operation does not exceed 10 eV (see also the data on ILISs in Table 1).

Outside the scope of this section are ILISs working in the droplet (jet) mode (see Fig. 7). They are capillary-type colloid (electrospray) sources, capable of generating charged and neutral droplets of complex composition with a mass up to 10^8 amu and a mass-to-charge ratio of more than 10^5 at the mean diameter of the droplets of 30–40 nm (see, e.g., [233, 234] and the references therein). Experiments have shown [235] that electrospray sources can be useful in analyzing complex biological objects using the SIMS technique, because the use of charged droplets of ionic liquids helps preserve the original molecular structure of the ions emitted from the surface of the objects under study. However, such an analysis is not local in view of the large diameter of the probing beam (jet).

6. Principal domains of application of EHD ion sources

The use of ions instead of electrons allows creating three-dimensional structures directly on the surface of the samples. This opens up prospects for ion implantation, deposition, and ion-stimulated etching, as well as ion beam cutting. In the framework of a single review, even if a very detailed one, it is impossible to discuss the entire range of applications of EHD sources, which is rapidly expanding year by year and is reflected in numerous research studies and reviews [1–5, 7–9, 26–32, 50–53, 236–245]. Without a doubt, EHD sources are currently one of the most in-demand ion sources in all branches of nanotechnology where the use of ion beams with a resolution within 100 nm is required. The possibility of obtaining new ions and designing new configurations of EHD sources, as described in this review, is attracting even more interest of researchers and designers to this class of ion sources and to their application domains.

6.1 Ion beam lithography and nanopatterning

Ion beam lithography (IBL) and creating nanosize functional instruments are among the principal technological tools in the domain of nanotechnology with a spatial resolution better than 10 nm [246–261]. Because ions are much heavier than electrons, ion beam systems have a much broader potential in regard to surface formation. Continuous fabrication of complex three-dimensional structures on larger-size areas is only possible with the use of a stable, high-precision, and fully automated system. For this purpose, Raith GmbH created an ion beam lithography device, VELION (Fig. 30) [262, 263], which allows processing large areas with different ions, ensuring the formation and modification of planar and three-dimensional structures. The ion column contains an LMAIS with a Wien filter (mass resolution $R_m > 50$). The beam diameter in the substrate plane varies in the range of 2–100 nm (FWHM), depending on the energy (1–80 keV) and the mass of the ions (6–3000 amu), as well as on the ion current (0.5–2000 pA). An additional electron beam column ensures the generation of a sharply focused electron beam with an energy of 1–20 keV for visual (*in situ*) control over preparation and electron beam lithography (EBL) of the samples. This column provides a high spatial resolution (down to 5 nm)

Figure 30. General view of the VELION ion beam lithography device [264].

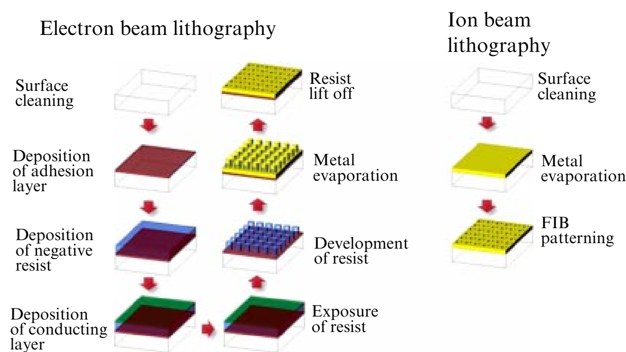

Figure 31. Step-by-step comparison of the methods of electron beam and ion beam lithography [262].

in combination with an automated focus correction, tuning flexibility, high precision, stability, and automation. Therefore, VELION is currently the only two-beam lithography device in the world for high-precision and efficient lithography with the use of both ion and electron beams.

IBL with a sharply focused beam offers new options for constructing and nanoengineering thin-layer structures. We note that direct resist-free lithography has a number of substantial advantages over other methods. Owing to optimization and a reduced number of processing cycles, IBL allows creating three-dimensional structures directly on a substrate and with a higher efficiency than EBL does.

Figure 31 shows a step-by-step comparison of the two lithography methods. VELION also opens broad possibilities for ion implantation, ion beam sputtering from the gaseous phase, and etching, and also for ion beam cutting (precision shock destruction of structure). The high spatial resolution of the electron beam opens access to ion beam processing of samples under direct control via an electron microscope, for example, in the fabrication of lamellae for transmission electron microscopy.

The formation of high-quality extended structures has always been fraught with methodological and instrumentation complications. In the VELION ion beam lithography device, a surface area of more than 1 mm^2 can be processed with nanosize resolution both by the method of stitching fields and in the mode of continuous displacement of the bench supporting the substrate. The standard field stitching in vector scanning lithography inevitably leads to the appearance of steps at the boundaries of the exposure fields. VELION was therefore developed and optimized to achieve the highest precision and reproducibility of the processing results. A five-axis laser interferometric bench (LIB) capable of tilting and rotating ensures a positioning precision of 1–2 nm, with exact stitching and juxtaposition of fields of the order of 20 nm over areas 100×100 mm in size. Comparative advantages of positioning with the use of the LIB and automated beam correction are illustrated in Fig. 32 with the example of the formation on gold of a three-dimensional structure (columns) 500 nm in height with two different tilt angles. Without an LIB, considerable variations in the structure due to drift, variations in the ion current, and poor stitching of fields can be seen (Fig. 32a). With the use of the LIB, on the other hand, automated corrections of the positioning, drift, and ion beam focusing inside the working field allow minimizing distortions of the ion beam even at the edges of the stitching fields (Fig. 32b). We note that the

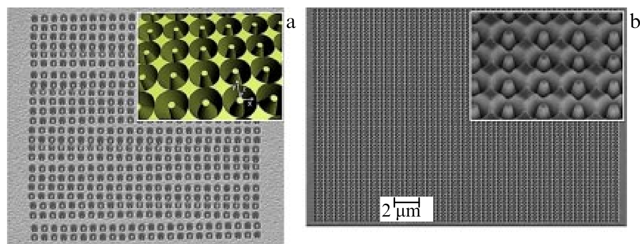

Figure 32. Comparison of stitching fields in ion beam lithography devices (a) without and (b) with the use of a laser interferometric bench and a system for automatic correction of the ion beam [265].

majority of these operations require stable continuous work of the lithography device over the course of many days.

The VELION ion beam lithography device features high temporal and current stability of the ion beams of different elements, such as Au, Si, Ga, Li, Bi, and Ge, the possibility of working at low irradiation doses, high spatial resolution (both in the imaging mode and in lithography), high precision, and small drift in beam positioning on the substrate. A calibrated sweep generator has for the first time allowed obtaining ultra-precise structures, even for long exposures. The capabilities of VELION can be extended by equipping it with additional nanomanipulators, a gas injection system, an optical camera, and a buffer. The advantages of an IBL device equipped with a laser interferometric bench over standard FIB devices discussed in Section 6.2 below are especially pronounced in patterning nanoobjects on larger areas.

An approach free of field stitching, called the fixed-beam moving stage (FBMS), ensures producing thin and smooth lines of arbitrary curvature up to several centimeters in length, as well as of variable-width lines. FBMS exposure can be used in different modes of operation. In the high-resolution mode, the beam is fixed and the sample is moved with a constant speed, which allows shaping one-pixel lines less than 20 nm in width. In the area filling mode, the continuous helical motion of the beam inside a disk allows obtaining lines up to several tens of micrometers in length. Within the width of a line, the dose remains constant, and circular symmetry guarantees a fixed size of the line irrespective of the direction of moving the sample.

The stitching-free mode of FBMS exposure is the ideal choice for creating nanosize optical waveguides and cavities. Examples of the successful formation and nanoengineering of thin-layer structures with three-dimensional design are provided by micro- and nanofluid (hydrodynamic) structures 1 mm in length, shown in Fig. 33, and a photon crystal (Fig. 34).

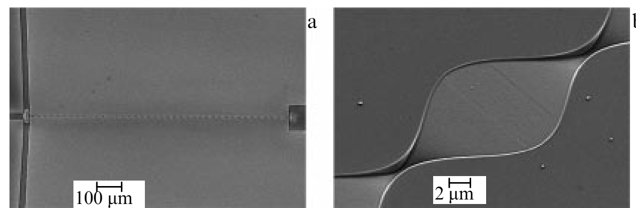

Figure 33. (a) Microfluid channel mixer 1mm in length in glass and (b) magnified view of its cross section [246, 250].

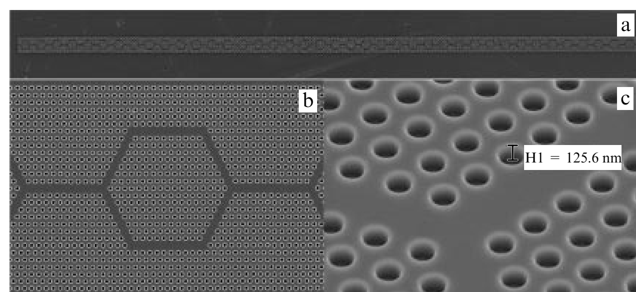

Figure 34. (a) Photonic crystal 1 mm in length in silicon and (b, c) magnified view of its parts [246]. H1 is the micropore depth.

Producing such large objects with high resolution requires high stability of the system in the course of many hours or even days. Therefore, creating patterns of an even greater size is apparently impossible. A convenient high-tech method for patterning gold foils on a silicon surface, called 'sketch and peel' [266], allows reducing the required time by an order of magnitude. Figure 35 shows a contact structure with gold strips on a silicon substrate 1 cm^2 in size, produced with this method, and its magnified parts [267].

6.2 Focused ion beam systems

The demands of the semiconductor industry gave impetus to the development of multifunctional focused ion beam FIB systems already in the late 1970s [268]. The main technological operations with FIB systems are ion microscopy [269–272], ion sputtering [273] and implantation [274], ion-stimulated etching and deposition [28, 275], the preparation of samples of nanosize thickness for transmission electron microscopy [8, 28, 276–278], micromilling of the surface [8, 270], the upgrade and repair of integrated microchips [279], the modification of probes and samples for implantation of individual ions [280, 281] as well as for scanning probing microscopy [282, 283] and atomic-probe mass spectrometry [284], ion tomography [285], ion mixing [286], the study of materials and multilayer

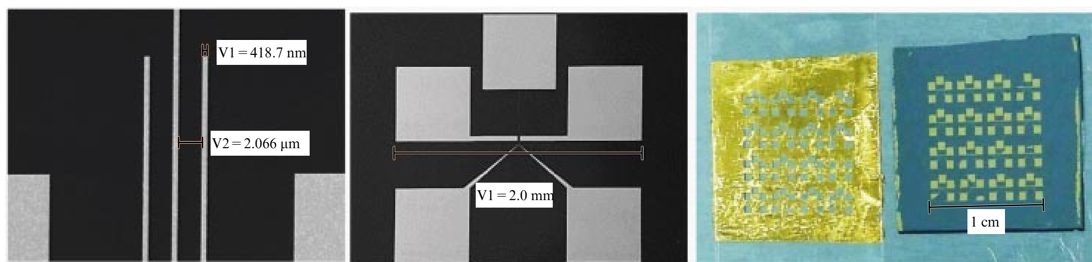

Figure 35. Contact structure with gold strips produced by the 'sketch and peel' method on a silicon substrate 1 cm^2 in size with magnified parts [267]. V1 and V2 are geometric sizes of the strips and gaps between them.

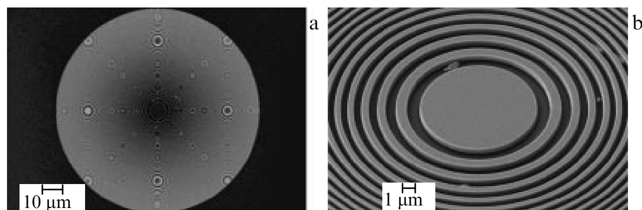

Figure 36. (a) Fresnel zone plate 100 μm in diameter produced by using a beam of gallium ions on a gold membrane 500 nm in thickness; (b) part of the plate with external strips 100 nm wide [1, 246].

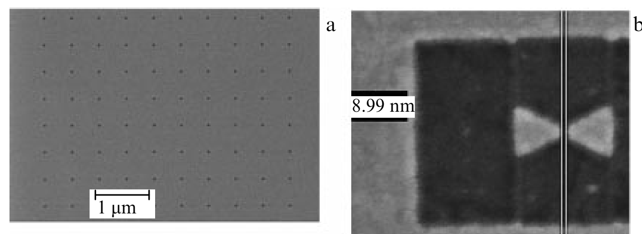

Figure 38. (a) Orifice 10 nm in diameter in an SiN membrane 30 nm thick, (b) bow tie antenna on the needle of an atomic-force microscope [1].

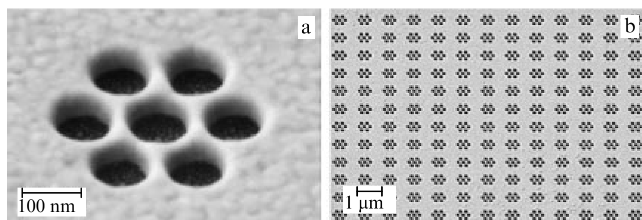

Figure 37. Oligomers 100 nm in diameter formed by gallium ions in a polycrystalline gold film 80 nm in thickness on a silicon substrate [1].

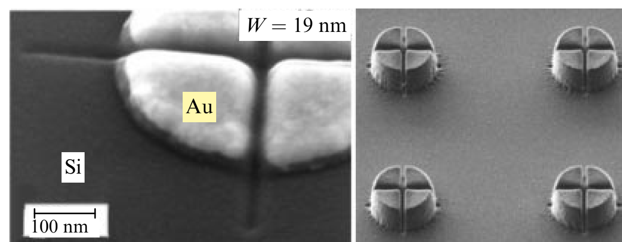

Figure 39. Elements of gold plasmonics on a silicon substrate [1, 246].

structures [270], correlation microscopy and nanopatterning [287, 288], superconductivity enhancement [289], the upgrade and repair of microelectromechanical systems [28, 290], manufacturing devices for integral optics and emission electronics [28], the investigation and modification of various structures in biology and medicine [269, 270, 290], and some others. Technological properties and application domains of FIB systems with gallium LMISs have been worked out in detail and are described in both the international and Russian literature [8, 26, 28, 291–296].

Some examples of producing various structures with the use of gallium ion beams shown in the figures are as follows: a Fresnel zone plate fabricated on a gold membrane (Fig. 36), oligomers in a polycrystalline gold film on a silicon substrate (Fig. 37), micropores in an SiN membrane and bow tie antenna on the needle of an atomic-force microscope (Fig. 38), and plasmonic elements made of gold on a silicon substrate (Fig. 39).

Although the first results with the use of LMAISs were obtained back in the 1980s, their broad use in industrial FIB systems started only a decade ago [297–304]. For example, the use of gold ions, besides the previously noted high sputtering coefficient, has a number of other useful functional properties. For example, in using Ga ions to create large craters in gallium arsenide, large gallium droplets form on its bottom (Fig. 40a), while the use of gold ions considerably accelerates the crater formation process, leaving its bottom smooth (Fig. 40b) [297]. Semiconducting nanowires made of GaAs and InAs, often grown by molecular-beam epitaxy, display a tendency to chaotic distribution over the surface. But if the semiconductor is preliminarily locally implanted with gold ions, especially with gold clusters, then the growth of wires can be achieved only in the locations bounded by the precision implantation (Fig. 40c) [300, 301]. A similar scenario allows selectively growing graphene layers. In [302], silicon carbide substrates were implanted with Au and Si ions with an energy of 60 keV, which allowed decreasing the temperature of graphene formation by 100 °C (Fig. 40d).

Currently, industrial FIB systems with ion sources on ionic liquids are not manufactured, and all the ILISs

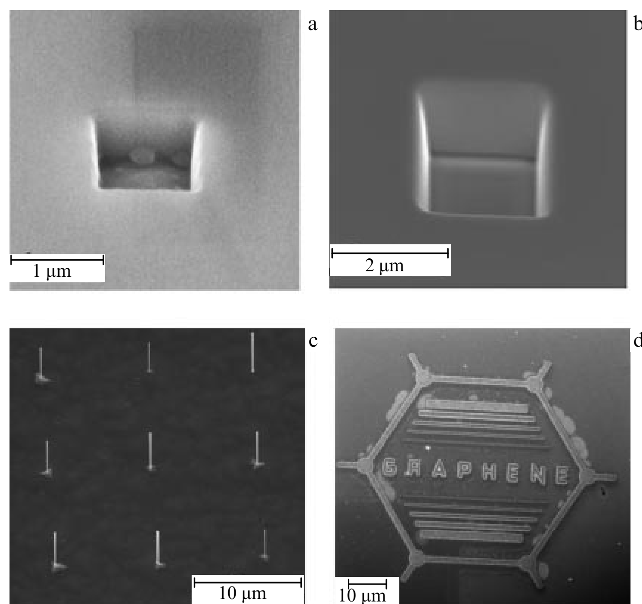

Figure 40. Craters in GaAs obtained in sputtering with (a) Ga and (b) Au ions [297], (c) local growth of nanowires in GaAs [299], (d) selective growth of graphene in SiC after implantation with 60-keV Au ions [302].

discussed in Section 5 are either test devices or prototypes. But in view of the unique possibilities offered by these sources, primarily the large mass and the reactive (chemical) capacity of the produced ions, as well as their bipolarity, we can expect that dedicated industrial systems equipped with ILISs will appear in the foreseeable future.

Information on the use of ILISs in nanopatterning and technological processing of microchips can be found in [61, 77, 224, 232, 236]. In [77, 224], an experimental ILIS (Fig. 4b) was installed in an FIB system developed by CNRS/LPN (France) and was used for ion etching of a silicon substrate covered by a mask with orifices. At an accelerating voltage of 15 kV, emission current of 10 μA, and total etching dose of 1.125×10^{17} ions, the sputter crater depth on the substrate was 17 nm. The sputter yield, i.e., the etching efficiency,

turned out to be equal to 5, and for a 30-kV gallium LMIS in the same system, the sputter yield was less than 2. The mean-square roughness of the surface at the bottom of the crater was approximately the same in both cases: 0.33 nm for the ILIS and 0.32 nm for the LMIS, although increasing the sputter yield usually leads to increased roughness. In the opinion of the authors of [77], charged microdroplets present in the ILIS-generated beam were responsible for the smoothing of the processed surface.

When switching an ILIS into the mode of pure ion emission, attended by a decrease in the emission current to 1 μA at the same accelerating voltage and the dose of 1.125×10^{16} ions, the sputter yield increased to 40. Such a high rate of etching cannot be obtained only due to processes of physical (ballistic) sputtering. The method of photoelectron spectroscopy allowed revealing amorphization of the irradiated surface and the formation of chemical compounds of silicon with carbon and nitrogen, which indicated the contribution of chemical (reactive) etching of silicon. Thus, it was shown that, in the mode of pure ion emission, the bombarding ions stimulate a surface disordering process and are conducive to the formation of highly volatile compounds of silicon with ionic liquid components without additional puffing of xenon fluoride active gases into the chamber.

ILISs with a needle emitter made of xerogel, shown in Fig. 29, were used in the mode of emission of negative ions from the ionic liquid [emim][BF_4] for ion etching of substrates made of Pyrex 7740 glass, silicon, and silicon dioxide. It was shown that irradiation with negative ions ensures stable and uniform etching process of all the substrates, not accompanied by surface charging. In using a 10-keV ion beam, the respective etching rate was 2.129 and 5.34 nm μA^{-1} min^{-1} for glass and silicon. The selectivity of SiO_2/Si etching in the substrate shown in Fig. 41 was equal to 2.26, which is a fairly high level.

The measurements performed in [232] confirmed that the ion etching rate is higher when using ILISs than for conventional gallium LMISs, due to the contribution of deep reactive ion etching. In addition, it was found that etching with negative ions is more efficient than with positive ones, because the negative ions generated with ILISs have a higher reactive capacity than the positive ones.

A capillary ILIS [230] has also been used for technological purposes. It was shown in [228, 230] that under irradiation of the surface of borosilicate glass and single-crystal silicon with ions from a source working on the [bmim][PF_6] ionic liquid, the surface of irradiated samples underwent smoothing as a result of chemical etching attended by the formation of free radicals (Si–F compounds), implantation of phosphorus ions, and surface deposition of carbon and nitrogen, which also interacted with the silicon.

Back in 1951, Erwin Wilhelm Müller built a field-ion microscope based on the design of an electron prototype [39], and in 1975 Levi-Setti used a hydrogen field-ion source in a transmission scanning microscope [305]. During half a century of development, the design of the column and of the EHD sources themselves has been improved so much that the ion beam size, especially for light ions, has become totally competitive with electron beams. Because the ion–electron emission yield is less sensitive to local inhomogeneities of the surface and less dependent on the incidence angle of the probing beam than the secondary electron emission yield, the contrast of ion images taken at the same spatial resolution better reflects the real topography of the surface

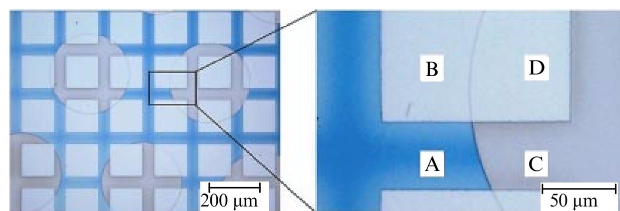

Figure 41. Substrate with silicon and silicon dioxide areas after irradiation with an ion beam: A — an SiO_2 area covered by a mask, B — an SiO_2 area subjected to ion etching, C — an Si area covered by a mask, D — an Si area subjected to ion etching (optical microscope image) [232].

under study. A number of other fundamental advantages of ion microscopy are discussed in detail in the reference literature [269–272].

Figure 42 shows images obtained with the VELION scanning ion microscope using beryllium ions (AuBeSi-LMAIS) with an energy of 70 keV and a 3-nm resolution, and using lithium ions (GaBiLi-LMAIS) with an energy of 40 keV and a 2-nm resolution.

6.3 Local secondary ion mass spectrometry

Secondary ion mass spectrometry (SIMS) is an analytic tool based on sputtering the surface of an investigated sample with a primary ion beam and the subsequent mass-spectrum analysis of sputtered secondary ions. By its nature, SIMS is a destructive method, although the degree of destruction of the sample can vary depending on the regime of the analysis. Detailed information on the SIMS method and its physical foundations, hardware provisions, static and dynamic operation modes, and application domains can be found in numerous papers, reviews, and books (see, e.g., [11–13, 306–311]).

In the static operation mode, a map (image) of the local intensity distribution of selected ions over the surface of the sample can be constructed, which means performing elemental (chemical) microanalysis (SIMS imaging or SIMS mapping). In the dynamic mode, in combination with depth profiling, the spatial distribution of these intensities in the sputtered volume of the sample can be reconstructed (3D SIMS). Detailed information on the current state, the necessary hardware and software, and applications of 3D SIMS to the analysis of inorganic and organic objects can be found in review paper [312].

In Fig. 43, we schematically show the process of formation of a 3D SIMS image, sometimes referred to as 'pseudo-3D visualization' [313], and the spatial distribution of $^{89}Y^+$ ions in a microvolume of superconducting ceramics $YBa_2Cu_3O_{9-y}$ 500 nm in thickness with an area of 200×200 μm. The main characteristics relevant in a local SIMS analysis are the spatial resolution (less than 50 nm) and contrast as functions of the analytic sensitivity (detection threshold); for 3D SIMS, these also include depth resolution (layer-by-layer resolution) less than 1 nm.

The main devices that constitute any SIMS installation are the source of primary ions (sometimes called the ion gun) and a mass analyzer equipped with systems for the collection, transportation, energy analysis, and detection of secondary ions. The choice of primary ions in modern installations is very broad: positive (including multicharge) and negative atomic, molecular, and cluster ions of various intensities and energies. Depending on the operation mode and requirements

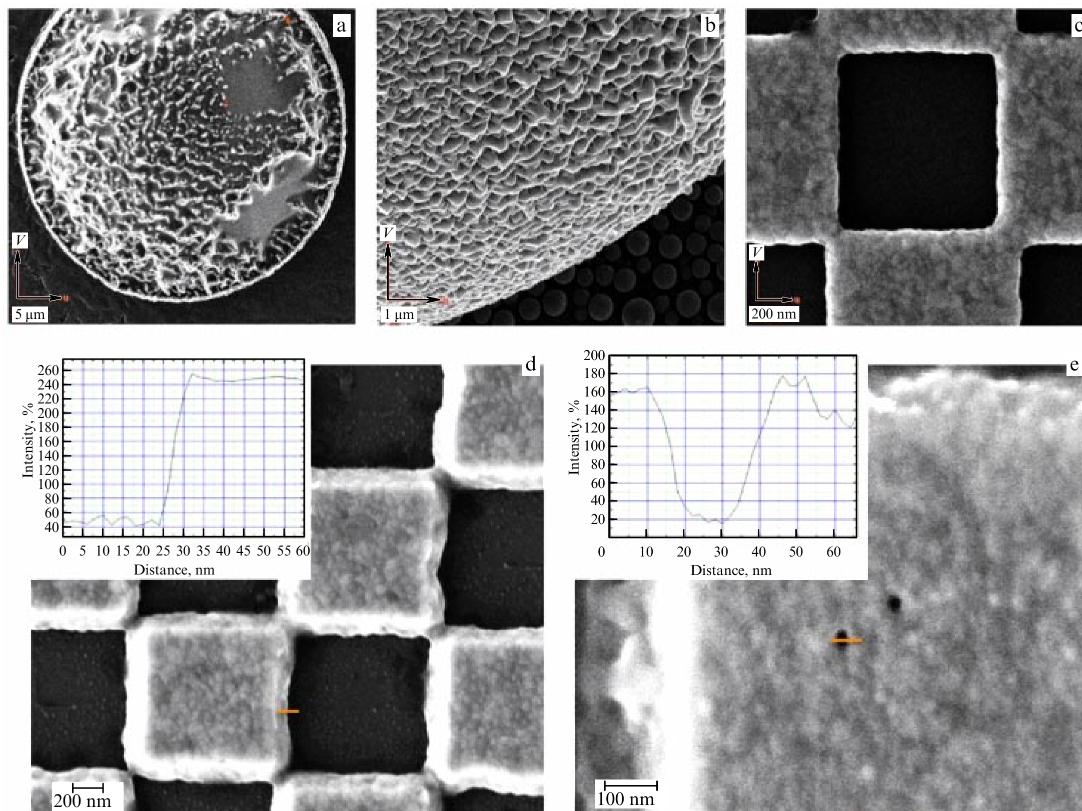

Figure 42. Contrast images with high spatial resolution obtained with the VELION scanning ion microscope (Raith GmbH) using (a–c) berillium ions [247] and (d, e) lithium ions [164].

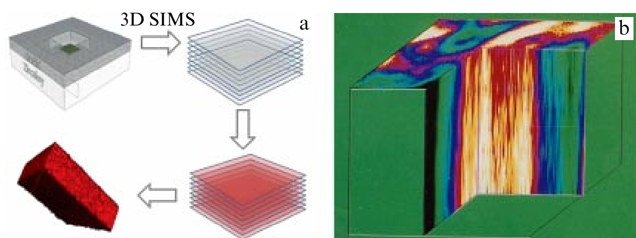

Figure 43. (a) Schematic presentation of forming a 3D SIMS image [313]. (b) Spatial distribution of $^{89}Y^+$ ions in the microvolume of a sample of superconducting ceramics $YBa_2Cu_3O_{9-y}$ (the intensity of $^{89}Y^+$ is color-coded with a thermal color scale; measurements were made by A B Tolstoguzov with the Atomika SIMS-4500 scanning quadrupole microprobe).

for the results of the analysis, gaseous or plasma sources, LMISs and LMAISs, surface ionization sources, gas cluster ion and field ion sources, ionic liquid sources, etc., can be used. The options for mass analyzers are more limited; they can be monopole and quadrupole filters, magnetic mass spectrometers with double focusing, and time-of-flight analyzers. Comparative characteristics of different mass analyzers are discussed in detail in [314].

Two strategies to obtain elemental (chemical) secondary-ion images are possible in local SIMS microanalysis: (1) scanning mode (the mode of a scanning ion microprobe), with a sharply focused ion beam scanning the analyzed surface area and the image of that area being formed at the detector by pixels that reflect the signal strength of secondary ions at a given point; and (2) stigmatic mode (the mode of a mass-spectrum microscope), with a broad ion beam irradiating all of the analyzed surface area and the image of that area projected onto the detector with electrostatic lenses. For the scanning ion microprobe, the main factor affecting the spatial resolution is the ion beam spot, although a proper definition of spatial resolution also involves the distribution function of secondary ions in their formation domain; for a mass-spectrum microscope, spatial resolution depends on the aberration distortions of the electrostatic lenses that form the image. We note that SIMS apparatuses with magnetic mass analyzers can work in both modes of obtaining microimages, while devices with quadrupole and magnetic analyzers can work only in the scanning microprobe mode.

Local mass spectrometry of secondary ions entered the active development stage in the mid-1960s [315, 316], with the goal to overcome a number of substantial deficiencies inherent in other methods of local elemental analysis, such as the limited range of analyzed elements, large informational depth, and low sensitivity; these properties are characteristic first and foremost of X-ray spectrometry microanalysis with an electron probe.

In this review, we do not attempt to follow the entire development path of the local SIMS method, and only discuss the principal scanning ion microprobes equipped with EHD sources, LMISs and LMAISs first of all. Why did these sources immediately attract the attention of the device designers? The answer is simple: the possibility of ensuring high spatial resolution using a reliable source of a sharply focused high-brightness ion beam with a relatively simple design.

One of the first SIMS apparatuses with an EHD source was built in 1984 at the University of Chicago by Levi-Setti's group [317, 318]. A scanning UC-HRL SIM/SIMS microprobe was equipped with a liquid metal source of gallium ions

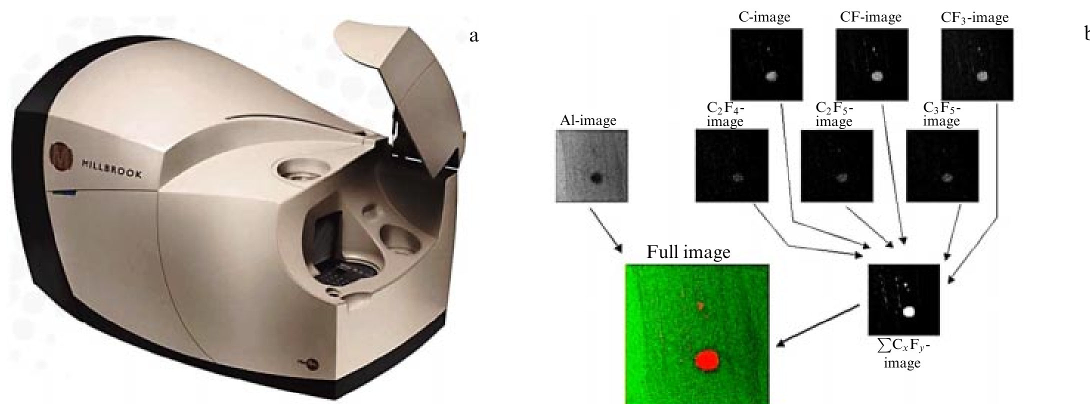

Figure 44. (a) General view of a MiniSIMS analyzer. (b) SIMS image of microimpurities on the surface of an Al substrate. Data are taken from the MiniSIMS promotional leaflet.

(FIB), which, at the maximum accelerating voltage of 40 keV, allowed obtaining a beam with the minimal diameter of 20 nm on the sample at the ion current of several tens of pA. As the mass analyzer, the Extranuclear 324-9 quadrupole mass spectrometer was used.

In 1994, the quadrupole mass analyzer was superseded by a magnetic mass spectrometer with double focusing, which allowed improving the transmission (sensitivity) and mass spectrum resolution R_m to 2×10^3. Numerous examples of using UC-HRL SIM/SIMS to microanalyze various objects, including biological ones, can be found in [318–321].

In the scientific literature, scanning ion microprobes with gallium LMISs are known under the common name FIB-SIMS systems. Besides UC-HRL SIM/SIMS, already discussed in the foregoing, we single out an installation [322] that combines the functionality of a scanning electron microscope and an FIB-SIMS system with a magnetic mass analyzer. In this installation, the objective lens and the electrostatic scanning system are common to the columns serving to form the electron and ion beams. Such an arrangement ensured an exact superposition of both beams, 20 and 70 nm in diameter, on the surface of the sample, which made it possible to choose the area to be investigated in the electron microscope mode (without sputtering the surface with the ion beam) with the subsequent registration of secondary ion images. The design of a compact magnetic mass spectrometer with double focusing, intended to become part of technological FIB installations (thus turning them into FIB-SIMS apparatuses), was modeled and developed in [323].

In the 1980s, the French company Riber manufactured a small line of the scanning ion microprobe MIQ-256 [311] equipped with a quadrupole mass analyzer and three different ion guns, including a gallium LMIS. The best spatial resolution with the beam of Ga^+ ions, about 60 nm, was obtained in investigating vertical slices of thin-layer $Al-LiNbO_3$ structures grown by molecular epitaxy. The measurements were performed with images in $^{27}Al^+$ ions with the registered signal strength varying in a range of 16–84%. According to our data, more than 10 such apparatuses were delivered to the USSR, mainly to electronic industry enterprises. However, we could not find any information on the use of MIQ-256 microprobes in the local SIMS mode in the domestic scientific literature.

Another example of a serial FIB-SIMS system is the desktop device MiniSIMS [324], which was manufactured in the early 2000s by Millbrook Instruments Ltd. (Great Britain). The device, whose general view is shown in Fig. 44a, was equipped with a quadrupole mass spectrometer and a gallium LMIS. Its main advantages were compactness and moderate price. The designers initially called the device a 'chemical microscope,' but later, after a discussion with one of the present authors (ABT), changed it to MiniSIMS. The promotion leaflets stated that MiniSIMS can work in both static and dynamic analysis modes with high elemental sensitivity and good depth and spatial resolutions. Figure 44b shows SIMS images of microimpurities on the surface of an Al substrate (the image is taken from the promotional leaflet, in which the size of the analyzed area and the spatial resolution were not indicated).

The MiniSIMS device was aggressively marketed as an analytic tool to replace expensive and massive SIMS installations, first and foremost for use in university laboratories. In [325], MiniSIMS was used to investigate self-assembled polymer monolayers on a silicon substrate, but no images were available in that work. Overall, the MiniSIMS devices could not quite attain the analytic characteristics claimed by their designers and, as far as we know, are not currently in use anywhere.

In the USSR, apparatuses for a local SIMS analysis were not mass-produced. In 1988, a pilot prototype of a scanning ion microprobe UAE OP. E-0.0001-008 ('Shipovnik') was developed and manufactured at the NITI, Ryazan [326]; a general view and functional layout are shown in Fig. 45. The apparatus was equipped with a quadrupole mass spectrometer, two ion sources (a duoplasmatron and a gallium LMIS), whose general view and functional layout are shown in Fig. 15 [141, 142], an automated sample manipulator, a unit for active and passive damping of vibrations, and an ultra-high vacuum system, including a ring ion Penning-type pump and a cryogenic pump working with liquid nitrogen and helium. The minimal diameter of the Ga^+ beam on the surface of a sample was 300 nm [141], which was a sufficiently good value at the time. Most of the units constituting this installation were developed and manufactured at the NITI and at electronic industry enterprises in the USSR. Serial production of scanning ion microprobes was planned, but only two installations could be produced because, after perestroika and the ensuing events, the NITI was shut down. [2]

[2] One of the present authors (ABT) was head of the project to create this scanning ion microprobe.

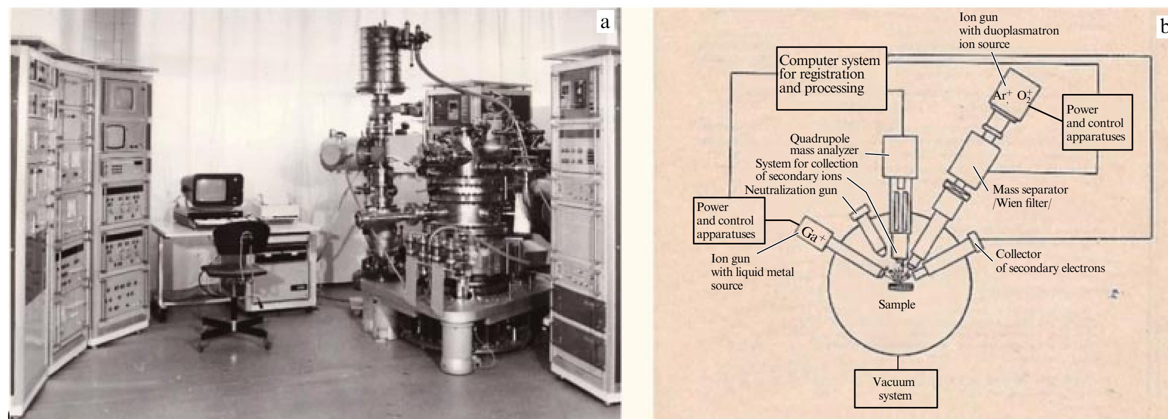

Figure 45. UAE OP. E-0.0001-008 scanning ion microprobe ('Shipovnik'): (a) general view, (b) functional setup [326].

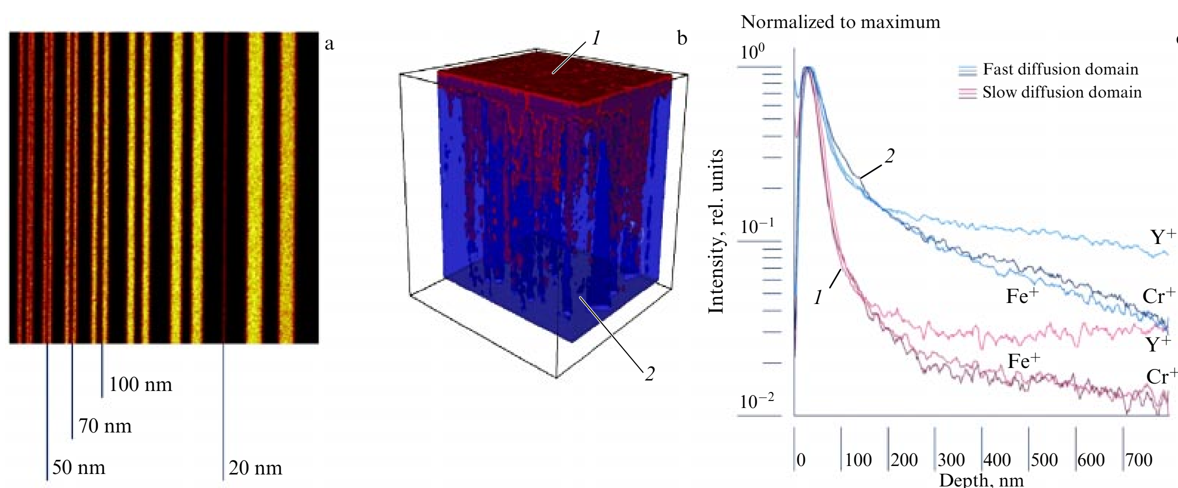

Figure 46. (Color online.) (a) TOF-SIMS image of a test object L-200 made in $^{27}Al^+$ ions (primary ions Bi_3^{2+}, image area 8×8 μm, pixel size 15×15 nm; the width of aluminum strips is shown under the image); (b) 3D image of the polycrystalline oxide $La_{0.8}Sr_{0.2}Ga_{0.8}Mg_{0.2}O_{2.8}$ (red (*1*) shows diffusion of chromium and iron in the bulk of the sample); (c) reconstructed depth profiling plots of this sample in Y^+, Cr^+, and Fe^+ ions for different diffusion domains (red, *1* — slow diffusion domain, blue, *2* — fast diffusion domain). The data are taken from a promotional leaflet for the TOF.SIMS 5 device.

Despite a certain degree of success achieved with FIB-SIMS systems, especially regarding semiconductor techniques and microelectronics, their extensive application in other domains was hindered by a number of negative factors: (1) low ion yield of most chemical elements in bombardment with Ga^+ ions, (2) poor depth resolution due to the use of primary ions of high energies, (3) fragmentation of complex molecular ions in the analysis of biological objects. Another factor was the possibility of forming films/islets of gallium and its compounds on the surface of the investigated objects [311]. The situation was aggravated by poor transmission, insufficient mass spectrum resolution, and an insufficiently large range of analyzed masses for quadrupole mass analyzers, which were used in most of the SIMS FIB systems. The replacement of quadrupoles with magnetic mass analyzers with double focusing (see, e.g., [319]) has allowed improving the transmission and resolution, but did not solve the remaining problems.

The subsequent development of local SIMS was associated with moving to time-of-flight mass analyzers and cluster sources of primary ions, including LMAISs with fine focused beams of gold [328] and bismuth [329] ions. Detailed information on the main stages of this development can be found in [330]. We only discuss the results obtained with TOF.SIMS 5 devices (IONTOF, Germany). They are equipped with a reflectron time-of-flight mass spectrometer with resolution $R_m \leqslant 10^4$ and a mass range of $(0.5-10^4)m/z$. They work in the dual-beam mode, with sputtering separated from sample analysis: for sputtering are used sources of O_2^+ and Cs^+ ions, and the pulsed LMAIS of bismuth is used for analyses in the static mode with currents in the pA range. Equipped with a Wien filter, this source allows obtaining beams of both atomic and cluster Bi_n^{m+} ions ($n \leqslant 5, m \leqslant 2$).

Some examples of the use of TOF.SIMS 5 in the local microanalysis mode are presented in Fig. 46: the image of a test object with nanosized Al strips (Fig. 46a) shows the possibility of obtaining a spatial resolution better than 50 nm. A 3D image of a complex polycrystalline oxide is shown in Fig. 46b, and Fig. 46c plots the results of a depth profiling of various elements reconstructed from this 3D microgram. Other examples of the use of TOF.SIMS 5 by the authors of this review for a depth profiling of reed switches and multilayer X-ray mirrors, for a quantitative analysis of $Si_{1-x}Ge_x$ structures, and for studying the fine size effect on the emission of secondary ions from silicon nanostructures and powders can be found in [331–334].

Improvements in the spatial resolution of the local SIMS method with a simultaneous decrease in the depth of the analyzed layer, i.e., improvements in the depth resolution, lead to a decrease in the number of atoms in the analyzed microvolume and hence to deterioration of the sensitivity of the method (the detection threshold) [335]. The only solution of this situation is the improvement of the acceptance and transmission factors for the mass analyzer and an increase in the ion yield (the ratio of the number of ionized atoms or molecules to the number of sputtered particles). The use of time-of-flight mass analyzers has allowed improving the acceptance and transmission factors, and the use of cluster ions of gold and bismuth in the probing beams increased the ion yield, especially in analyzing biological objects. Further progress can be achieved with the use of post-ionization of sputtered particles, i.e., by moving from SIMS to SNMS, already noted in the Introduction. A detailed discussion of the peculiarities and the development stages of SNMS can be found in papers, reviews, and books [15–18, 310, 336]. We here discuss one the most recent designs [337] that use laser post-ionization of neutral sputtered particles (Laser SNMS or LPI-SNMS [17]).

The results of a local microanalysis of complex polymer compounds with TOF-SIMS and Laser-SNMS methods are compared in [337]. The measurements were made with a TOF-SIMS.5 commercial device, additionally equipped with a Lambda Physik AG excimer laser (Germany), generating radiation at the wavelength of 157 nm with a power density of 5.5×10^6 W cm^{-2}. In Fig. 47, we show images of a silicon plate with spherical polyethylene terephthalate particles (PET ES301445, with a particle diameter of about 1 μm and molecular weight of $\sim$ 25,000 amu). In Fig. 47a, we show the image of a surface 22 × 22 μm in area obtained by the TOF-SIMS method at a Bi_3^+ irradiation dose of about 2×10^{13} cm^{-2}. The intensity of secondary potassium ions (K^+: red) is shown in red (*1*); potassium is a surface impurity on an Si plate and serves as its marker, because the yield of positive ions is higher for alkali metals than for silicon. The total intensity of mass peaks of the secondary hydrocarbon ions $C_7H_7^+$, $C_8H_7^+$, $C_8H_9^+$, $C_8H_7^+$, $C_9H_9^+$, $C_{10}H_8^+$, $C_{13}H_9^+$, $C_{15}H_7^+$, $C_{15}H_9^+$, and $C_{15}H_{13}^+$, which were selected as markers for the polymer compound and denoted as 'Sum of PS_{SIMS}' in the figure, are show in green (*2*). Adding the intensities increases the dynamic range and improves the signal-to-noise ratio. In Fig. 47b, we show images of the analyzed areas of an Si plate, registered with an optical microscope, and in Fig. 47c, an image obtained using the SNMS (Laser-SNMS) method with mass peaks of the ions $C_6H_5^+$, $C_7H_7^+$, $C_8H_7^+$, $C_8H_9^+$, $C_9H_7^+$, $C_9H_9^+$, and $C_{15}H_9^+$ (green, 'Sum of PS_{SNMS}') chosen as the polymer markers. The surface area was taken to be 25 × 25 μm, and the irradiation dose with Bi_3^+ ions was 7×10^{11} cm^{-2}, which is about 30 times less than in the SIMS analysis. In both cases, the diameter of the primary Bi_3^+ beam (spatial resolution) was of the order of 200 nm. The images shown in Fig. 47 clearly demonstrate the superiority of the SNMS methods with laser post-ionization of sputtered neutral atoms and molecules over the 'conventional' SIMS method, where only secondary ions are registered. Figure 47c evidently shows defects in the distribution of microspherical polyethylene terephthalate particles (shown by yellow arrows), which are impossible to discern on the 'blurred' image shown in Fig. 47a.

We note that any experimental image is not a full map of the concentration distribution of chemical elements over the

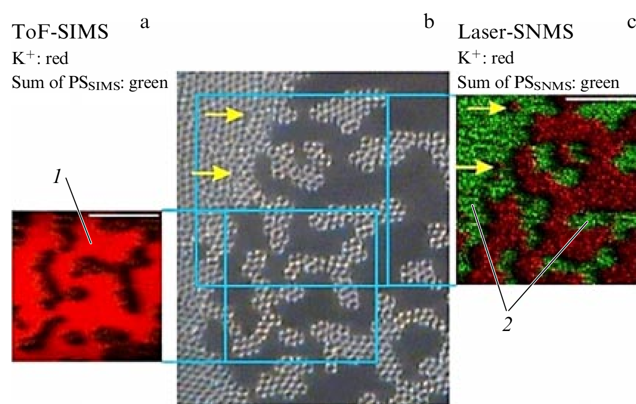

Figure 47. (Color online.) Image of a silicon plate with a film of spherical polyethylene terephthalate particles. (a) Image made with secondary ions (SIMS), (b) optical microscope image, (c) image made with ionized neutral particles (Laser-SNMS) [337].

surface or a microvolume of the sample under study. It should rather be viewed as a superposition of four main contrasts (see, e.g., [311, 335]): concentration, topographic, chromatic, and matrix, and also of some additional contrasts related to the properties of the samples and the method for obtaining the SIMS image. The topographic contrast is due to the different efficiencies of extracting and collecting secondary ions from the microroughness of sample surfaces, and properly taking that contrast into account is one of the main tasks of local SIMS. Here, we discuss the method of correlative microscopy [338], which amounts to parallel *in situ* registration of an image in secondary ions and electrons, with the electron map formed by means of a high-resolution TEM. This approach is not new in and of itself. In this section, we already mentioned an installation [322] combining the functionality of a scanning electron microscope and an FIB-SIMS system equipped with a magnetic mass analyzer. We also note the VG Scientific SIMSLAB scanning microprobe [339], which allowed obtaining images in secondary ions and electrons using a gallium LMIS (MIG100). But the SIMS-TEM integration allows obtaining images with higher spatial resolution and better accounting for the topographic contrast, which is pronounced on electron maps.

In Fig. 48, we present the functional setup and general view of an installation for parallel ion and electron spectrometry (PIES) [340] developed at the Luxembourg Institute of Science and Technology. The PIES installation was made based on the FEI Tecnai F20 TEM transmission electron microscope equipped with a gallium LMIS Magnum FEI FIB and a magnetic mass analyzer with double focusing and two parallel detectors of secondary ions (D1 and D2), with the analyzed mass range of 1–80 amu. The electron beam energy could be varied in the range of 80–200 keV with the maximum spatial resolution of 0.14 nm, while the energy of the monoisotope $^{69}Ga^+$ ion beam could be varied in the range of 5–30 keV, with a beam diameter of less than 10 nm on the sample. The installation was additionally equipped with an energy-dispersive X-ray spectrometer (EDS).

As an example of the application of PIES, in Fig. 49 we show images of a transverse slice of a thin plate (lamella) of a solar panel made with secondary negative ions of hydrogen and oxygen (Fig. 49a) and with electrons (Fig. 49b). We see from the SIMS image that hydrogen, whose role

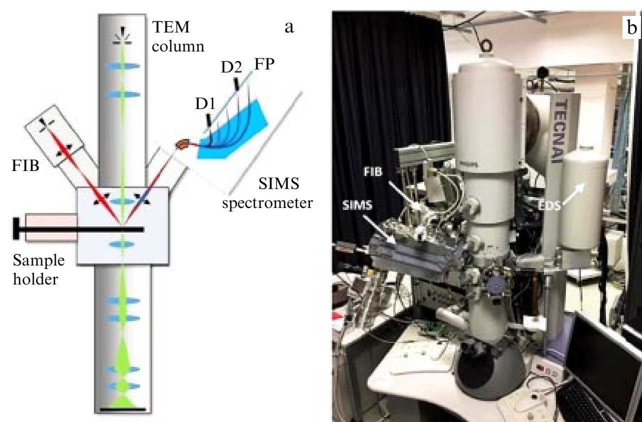

Figure 48. Installation for parallel ion and electron microscopy [340]: (a) functional schematic, (b) general view. FP — focusing plane, D1 and D2 — secondary ion detectors.

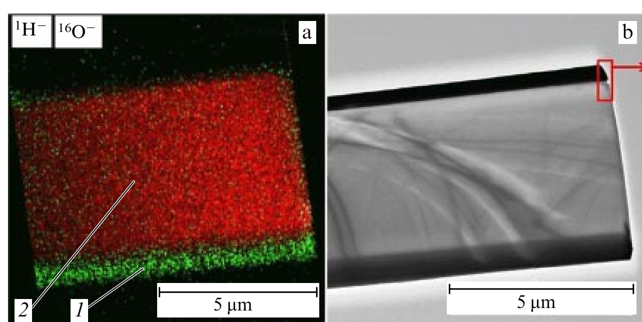

Figure 49. (Color online.) (a) Image of a transverse slice of a solar panel made with secondary negative ions of hydrogen (green, *1*) and oxygen (red, *2*), (b) TEM image of the same area [340].

amounts to minimizing the electron–hole recombination, is mainly located in the lower part of the lamella. We note that the local distribution of hydrogen is very difficult to measure with other analytic tools, for example, with the help of an EDS.

The current development level and prospects for correlative microscopy are discussed in review [341]. There are advantages to combining gallium FIB SIMS with the methods of scanning electron microscopy, energy-dispersive X-ray analysis, diffraction of reflected electrons, and atomic-force microscopy. In Fig. 50, as an example of such a hardware integration, we present an image of an FIB SEM scanning electron microscope (TESCAN, Czech Republic) with an additional orthogonal time-of-flight mass analyzer o-TOF (TOFWERK, Switzerland) intended for an FIB SIMS. Review [341] gives numerous examples of the successful use of complex microscopy apparatuses in the analysis of thin films, various metals, electrochemistry objects (lithium batteries), items of cultural heritage, and geological samples, including for their isotope analysis. Overall, a certain degree of renaissance can be observed in analytic apparatus building, reviving the ideas of the 1980s, when several methods were integrated into a single surface analytical instrument, including the methods of Auger electron microscopy, secondary ion mass spectrometry, low-energy ion scattering, and photoelectron spectroscopy. But the current approach has become more per-

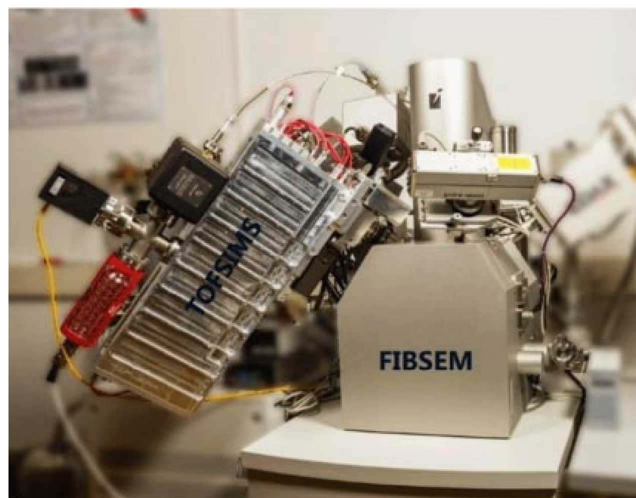

Figure 50. Integrated FIB SIMS SEM apparatus [341].

fected as regards the apparatuses and the methods, which allows solving ever more complicated technological problems with higher spatial and depth resolutions, preserving the high elemental and chemical sensitivity.

6.4 Electrohydrodynamic sources for space exploration

Not only are EHD sources in demand on Earth, but they have also found an appropriate place in space. Three main areas can be singled out here: (1) control and neutralization of the induced potential occurring under the action of solar wind and other versions of cosmic radiation on the outer shell of spacecraft, (2) sources of primary ions for SIMS analyzers working aboard orbital and interplanetary missions, and (3) electrostatic rocket engines for small and ultra-small spacecraft with limited onboard resources.

6.4.1 Control and neutralization of the potential on the surface of spacecraft. It is known (see, e.g., [19, 342, 343] and the references therein) that the outer surface of spacecraft in Earth's orbit is affected by the strong action of solar wind — the flow of charged particles, mainly of helium–hydrogen plasma, from the solar corona. Solar wind interacting with the upper layers of Earth's ionosphere above the Kármán line is conducive to the formation of a cold proton–electron plasmasphere with particle energies of 0.1–10 eV, held by Earth's magnetic field (the magnetosphere). Electrons and ions from the plasmasphere hit the surface of spacecraft, which is in addition subjected to the action of solar radiation of a wide frequency spectrum: from gamma and X-ray radiation to radiation in the ultraviolet, optical, and infrared ranges. As a result of these actions (Fig. 51), the surface of spacecraft, which are isolated in space, accumulates an electric charge, mainly of positive polarity. The electric potential produced by this charge, in accordance with various estimates [342, 343], can reach 100 V, which interferes with the work of onboard radioelectronic devices and instruments. To neutralize the induced potential, the use of different sources of positive ions was proposed [19, 342, 343], so as to 'pull off' the positive charge into the space outside the spacecraft.

The neutralization tools considered initially were sources with surface ionization, which could generate ions of lithium and other alkali metals. But, as we already mentioned in

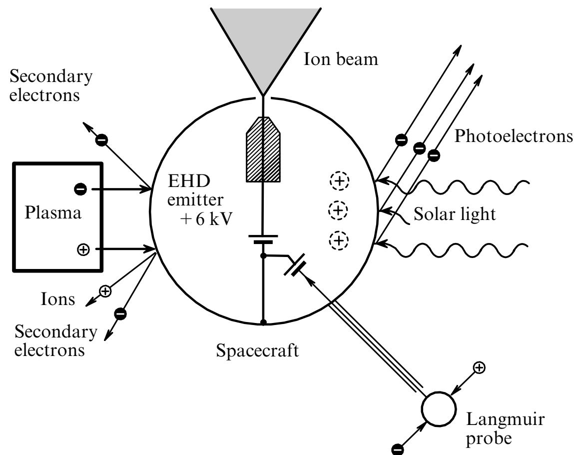

Figure 51. Spacecraft on Earth's orbit: the action on its outer surface of different types of radiation and neutralization of the induced potential with an EHD source [19].

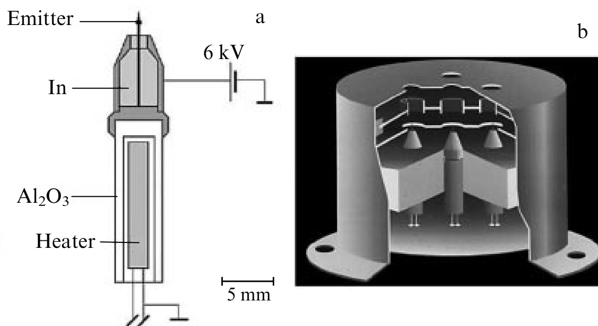

Figure 52. ASPOC system for active control and neutralization of the surface potential of spacecraft: (a) diagram of a single indium LMIS, (b) general view of the neutralization module with three LMISs and a system for focusing and extracting ion beams [19].

Section 1.1, after the first successful experiments with EHD sources aboard the Russian orbital Mir station in 1991, a commercial active control and neutralization system, ASPOC, was developed at the Austrian Researcher Center (ARC) in Seibersdorf, which after minor modifications was then successfully used on different spacecraft and space stations [19].

The basic version of the ASPOC system with three indium LMISs is shown in Fig. 52 [19]. Depending on the purpose and duration of a space mission, each source was loaded with 0.25 to 1 g of indium. The working temperature of the source was 200 °C, with a heating power of 0.8 W; the maximum accelerating potential was 6 kV, which allowed obtaining beams of In^+ ions with a current up to 20 μA. In the GEOTALL mission, the ASPOC system with eight LMISs worked for more than 600 h in total over a period of six years, ensuring a controlled decrease in the potential on the spacecraft surface to 1 V, with the starting values in the range of 25–50 V [19].

The main problem that occurs in using any ion sources for neutralization of the induced potential in space is contamination of the spacecraft units with primary ions and neutral particles from the emitted beam, not to mention the sputtering of ion optics elements and the spacecraft surface with these ions, which can travel back to the surface of the spacecraft under the action of Earth's magnetosphere. Optimization of the design and operation modes of the indium LMIS has allowed reducing the number of neutral particles in the beam and minimizing the processes of undesirable sputtering and deposition of sputtering products on actuation elements and the outer surface of the spacecraft. Another problem is the negative induced potential, which is impossible to neutralize by emission of positive ions from the spacecraft. However, experiments [343] have shown that the probability of a negative charge appearing in Earth's orbit is quite low. In principle, it can be eliminated altogether by using sources of electrons or universal EHD sources with ionic liquids, which can generate ion beams of either polarity.

6.4.2 Space secondary ion mass spectrometry. Interest in the investigation of space objects, which surged in the 1960s after the first space flights, was one of the drivers behind the development of both apparatuses and methods for secondary ion mass spectrometry, which we already discussed in detail in Section 6.3. Space applications of local SIMS can be divided into laboratory investigations of objects of cosmic origin that have arrived on Earth naturally or were brought by a reentering spacecraft, and investigations conducted in the course of space missions directly (*in situ*) aboard spacecraft and stations. The results of ground investigation of meteorites, space dust, lunar soil, etc. warrant writing a separate review or book, and we do not discuss these investigations here, directing the reader, for example, to [344, 345] and the references therein.

Worthy of note are onboard SIMS studies, although they are much less numerous than the ground-based ones. The first such successful experiment was performed on the Mir station in 1991. The onboard scanning ion microprobe (international project MIGMAS) [346] was equipped with an indium LMIS, developed at the ARC and ensuring beam focusing to less than 5 μm in diameter, and a monopole micro-mass analyzer developed by Cherepin's group [14, 238]. The primary task was to study corrosion processes of different construction materials under the action of solar wind and other types of cosmic radiation (see Fig. 51). For this, the investigated sample, placed in a special vacuum container, was pulled out into open space, and then without contact with the atmosphere inside the station was moved into the test chamber of a mass spectrometer. The results of these investigations are described in detail in [19, 346].

Interestingly, the first attempt to conduct an SIMS investigation in open space was undertaken back in 1988 in the framework of the international project DION [19, 347]. Although an EHD source was not involved in that experiment, it is worth commenting upon it here. The Soviet space station Phobos, which was to reach the surface of the namesake satellite of Mars, carried a plasma source of ions SIPPI [348], which allowed obtaining a powerful beam of Kr^+ ions with an energy of 3 keV and current of 3 mA. As the spacecraft would approach Phobos to within 50 m, the beam was to hit the surface of the satellite and the emerging secondary ions were to be collected and analyzed with the Fortron reflectron time-of-flight mass analyzer, developed by the Hungarian Academy of Sciences. In addition to the ion beam, the surface of Phobos was also to be irradiated by laser and electron beams. The combined data on the elemental and chemical composition of the surface of Phobos would settle the question about its origin—whether Phobos had ever been part of Mars. Unfortunately, the mission failed.

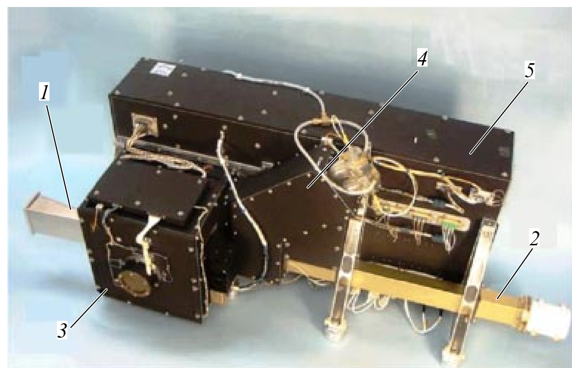

Figure 53. General view of the COSIMA onboard scanning ion microprobe: *1* — device for collecting comet dust, *2* — manipulator, *3* — analytic chamber, *4* — two-channel LMIS with isotopically pure ^{115}In, *5* — time-of-flight mass spectrometer of secondary ions [350].

SIMS investigations were successfully performed aboard the spacecraft sent to the 67P/Churyumov–Gerasimenko comet (the Jovian group of comets) in the framework of the international ROSETTA mission. The spacecraft was launched in 2004, and its primary task was to collect and study space dust in the close vicinity of the comet [19, 349, 350]. For this, a scanning ion microprobe, COSIMA (COmetary Secondary Ion Mass Analyzer), had been designed, which included an indium LMIS [19, 350], which was also developed at the ARC but had a more complicated design than did the sources used for neutralization of the potential on the spacecraft surface and in the ion microprobe MIGMAS. That LMIS consisted of two ion sources, one of which worked in the direct-current mode and was used to clean and sputter the surface of analyzed particles, and the other probing source was intended for SIMS analysis of those particles; thus, a 'dual-beam mode' was realized, which was then successfully used in TOF.SIMS devices described in Section 6.3. The probing ion source worked in a pulsed mode with the pulse duration of ~ 3 ns (on the order of 10^3 ions in one pulse at the repetition rate of 1.5 kHz) and at the energy of 8 keV ensured beam focusing to 10 μm in diameter. Both sources were loaded with isotopically pure indium ^{115}In in order to avoid undesirable mass-spectrum interference of secondary ions due to the contribution of the ^{113}In isotope. The space dust particles, whose speed did not exceed 10 m s^{-1}, were collected in open space on the surface of a target covered with a layer of porous gold. An image of the target was then taken with the optical microscope COSISCOPE, and selected areas 35×50 μm in size containing space dust particles were analyzed with a reflectron time-of-flight mass analyzer with the resolving power of 1400 (FWHM) for $m/z = 100$. The general view of the onboard ion microprobe COSIMA is presented in Fig. 53 [350].

Overall, during the period of active work of COSIMA (from 2014 to 2016), more than 250 samples of space dust particles were collected and analyzed; the particles were given individual names. Each of these samples contained at least 30 individual particles. Typical mass spectra of positive secondary ions for three different samples are shown in Fig. 54 [350]. Mass spectrum files were transmitted to Earth, where they were processed with the use of relative sensitivity coefficients to quantitatively estimate the concentration of different elements in the comet's dust. Detailed information on the results of SIMS analyses made with the use of the ion

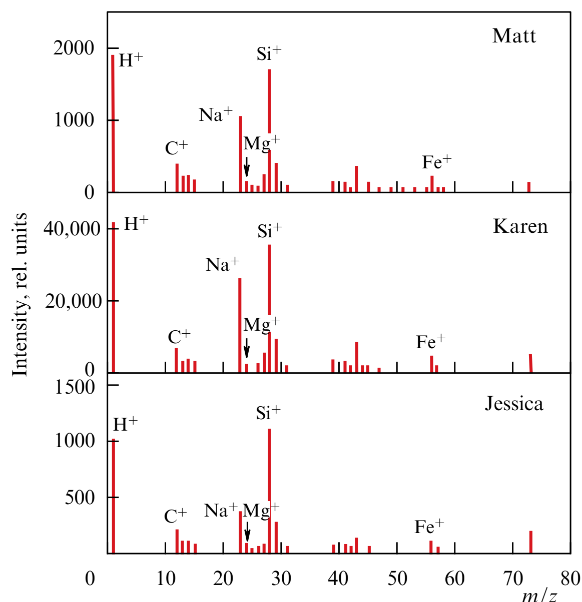

Figure 54. Typical mass spectra of positive secondary ions obtained for three different space dust samples; the names are indicated in the upper right corner of each spectrum [350].

microprobe COSIMA in the framework of the ROSETTA mission can be found, e.g., in [349, 350].

6.4.3 EHD sources for electrostatic rocket engines (microthrusters). The development of EHD sources was initially aimed at their prospective use in electric micropropulsion engines, in which a constant electric field accelerates ions or charged droplets of the working material to high speeds, of the order of several tens of kilometers per second or faster, thus creating thrust in the range of 1–100 μN. Such engines are classified as ion microthrusters and are called field emission electric propulsion (FEEP) thrusters [351]. Besides their compactness, efficiency, and design simplicity, the main advantage of FEEP thrusters is the possibility of a quick start with smooth and controllable tuning of thrust by changing the accelerating voltage.

Starting in the late 1950s, capillary electrospray (colloid) ion sources for ion engines were developed in the USA and the USSR. As a working material (propellant), they used glycerine, tributyl phosphate, and other liquids conducting electrical current. Presently, commercial electrospray microthrusters are manufactured by the American company BUSEK [352], but we do not discuss them here because of the limited volume of this paper.

In the 1960s, Krohn [40], and then Swatik and Hendricks [41], staged experiments with LMAISs working in the droplet mode with the Ga–In alloy, and showed the potential feasibility of such sources for producing reactive thrust. However, comparing the droplet mode and the pure-ion mode shows that the latter is more advantageous from the energy point of view and more parsimonious due to lower working material consumption, which is especially important for autonomous spacecraft, which can hardly be refueled in space. In addition, for tip EHD sources, their operation in the droplet mode leads to rapid degradation of the emitter tip apex, thereby reducing their lifetime.

Before reviewing the modern EHD sources for FEEP thrusters, we clarify their main characteristics, such as mass efficiency factor k_{ion}, specific impulse I_{sp}, and thrust T.

Mass efficiency factor k_{ion} shows the fraction of the working material used to generate ions:

$$k_{ion} = \frac{\dot{m}_{ion}}{\dot{m}_{tot}} = \frac{\dot{m}_{ion}}{\dot{m}_{ion} + \dot{m}_{drop}}, \quad (17)$$

where $\dot{m} = dm/dt$ is the consumption rate of the working material, which (depending on the subscript ion, drop, or tot) is, respectively, related only to the generation of ions, charged droplets, or the total flow (for the pure ion mode, $k_{ion} = 1$).

Specific impulse I_{sp} can be evaluated as

$$I_{sp} = \frac{v_{ion}}{g_0} k_{ion} f, \quad (18)$$

where $v_{ion} = \sqrt{2qU/m}$ is the speed reached by an ion with a mass m and charge q under the accelerating voltage U applied to the emitter relative to the grounded extractor electrode, g_0 is the free fall acceleration (gravity constant), and f is a geometric factor responsible for the losses resulting from the divergence of the ion beam (for thrusters equipped only with an extractor electrode, its value is 0.8–0.85, and in the case of a focusing electrode, it can reach 0.98). The specific impulse has the dimension of time and is typically measured in seconds.

Thrust T depends on the specific impulse and the consumption rate of the working material:

$$T = g_0 \dot{m} I_{sp}. \quad (19)$$

Importantly, the larger the specific impulse, the less working material Δm required for changing the speed of the spacecraft by Δv:

$$\Delta m = m_0 \left[1 - \exp\left(-\frac{\Delta v}{g_0 I_{sp}} \right) \right], \quad (20)$$

where m_0 is the initial mass of the working material.

Formula (20) is valid for the acceleration of a spacecraft in open space (free of atmospheric drag). Evidently, the specific impulse is important in long-term missions, when the onboard supply of the working material is limited. At the same time, as follows from (18) and (19), a high specific impulse limits the thrust necessary for launching the spacecraft into Earth's orbit. More advantageous in that case are boosters with chemical propellants, which can produce strong thrust with a relatively small value of specific impulse.

The main working materials that are used in modern EHD sources for FEEP thrusters are indium and cesium. These chemical elements have a relatively large atomic mass (114.8 amu for In and 133 amu for Cs) and low ionization energies (5.78 eV for In and 3.9 eV for Cs), and therefore, in the pure-ion mode, they can ensure high thrust at a relatively small ratio of produced power to thrust value; Cs is somewhat preferred to In in that respect. However, cesium, unlike indium, is toxic and chemically very active (is vigorously oxidized in air), and is also in the liquid state in the source reservoir ($T_m \sim 28.4\,^\circ$C), which, on the one hand, allows saving on power needed to heat and melt it, but, on the other hand, can cause its leak from the reservoir due to increased vibrations accompanying the launch of the spacecraft. Indium has to be melted ($T_m \sim 157\,^\circ$C), but it is inert and can be stored for a long time in a standard reservoir without vacuum suction and/or puffing dry nitrogen or an inert gas. Therefore, indium is more suitable for FEEP thrusters than cesium is.

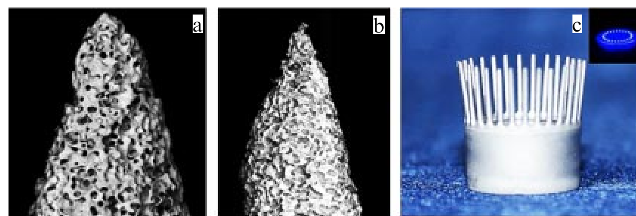

Figure 55. Apex of a porous tungsten emitter (a) without indium and (b) wetted (soaked) with indium; (c) corona-shaped LMIS with 28 porous emitters. The inset in the upper right corner shows the working source [20].

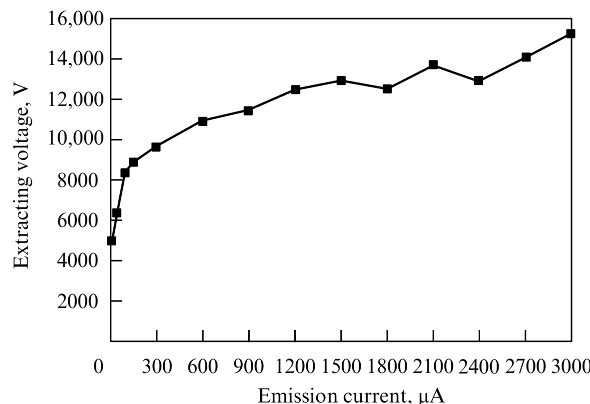

Figure 56. Current–voltage curve of an indium corona-shaped LMIS with 28 emitters of porous W [20].

Indium LMISs for use in space have been developed in Austrian research centers and universities for more than 45 years [19, 20]. By upgrading the sources with needle W-emitters that had been successfully tested in devices for neutralization of potential and in onboard SIMS apparatuses, cluster ion sources were developed in the FOTEC research center [353] that combine 4 to 16 individual LMISs with standard needle emitters, and corona-shaped LMISs with 28 porous W-emitters along the circumference (Fig. 55) [20]. Emitters with micrometer-size pores and a relative porosity up to 85% were produced by compressing tungsten powder, sintering in a special form, and sharpening by chemical etching.

The main goal of creating multiemitter LMISs is an increase in the total ion current and in the source lifetime. Experiments [20] have shown that, when loaded with 15 g of indium, such sources can generate a current up to 3 mA at an accelerating voltage in the range of 3–18 kV and have a lifetime up to 20 thousand hours. The current–voltage curve of corona-shaped LMISs is shown in Fig. 56 [20].

Interest in microthrusters increased considerably after the appearance of CubeSat satellites [354, 355], developed in 1999 at the California Institute of Technology (Pasadena, USA) and Stanford University (Palo Alto, USA). A CubeSat spacecraft is a cubic metal frame $10 \times 10 \times 10$ cm in size (1U, the basic CubeSat unit), which can contain several scientific instruments together with the necessary radioelectronic devices. Outside are solar panels that supply the satellite with several watts of energy and expandable antennas. The total weight of the satellite is not more that 1.33 kg, and its lifetime is estimated to be 25 years. Several individual satellites can be integrated into a module system (nU).

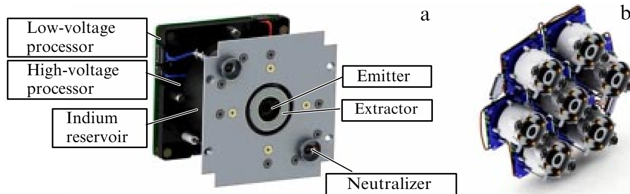

Figure 57. (a) Commercial IFM Nano Thruster, (b) module FEEP engine made of seven individual thrusters [357].

The majority of CubeSat customers are universities, research centers, and small commercial companies. Currently, most of these satellites are still passive objects (without an engine). We note that at the altitude of 600–700 km above Earth's surface, the atmospheric drag force is approximately 0.15 μN, and therefore, in order to be able to make autonomous maneuvers in such an orbit, a CubeSat must have an engine with a thrust of several tens of μN. Microthrusters for orbit corrections and precise orientation of CubeSat satellites in near-Earth space are being actively developed now; in the future, flights to the Moon and possibly interplanetary missions are envisaged for them.

Commercial FEEP microthrusters with corona-shaped indium LMISs are currently manufactured by the Austrian company ENPULSION [356]. A general view of this thruster, called the IFM Nano Thruster, is shown in Fig. 57a; Fig. 57b shows a module engine assembled from seven individual thrusters [357].

An individual thruster contains a reservoir for the working material (In), a corona-shaped emitter unit (LMIS), an extractor electrode, a positive charge neutralizer (source of electrons), and two processors (PPU). Technological specifications of the thruster are as follows:

— thrust: 10–500 μN (nominal value: 350 μN);
— specific impulse: $(2-5)\times10^3$ s;
— working material (indium) load: 250 g;
— outside envelop: $94\times90\times78$ mm;
— weight: 640 g (with working material, 890 g);
— power: 8–40 W;
— lifetime: more than 13×10^3 h.

Often indicated for microthrusters is also the total impulse, which shows the thruster resource, i.e., how long it can generate the specified thrust. For the IFM Nano Thruster, the total impulse is greater than 5×10^3 N s. We note that this microthruster is the first FEEP thruster that was put into operation in 2018 and successfully worked in low Earth orbit as part of CubeSat satellites on the 3U platform. As of early 2020, a total of 25 satellites equipped with such microthrusters have been launched into space.

On the market of commercial FEEP thrusters for CubeSat satellites, a gallium nanoFEEP is currently available that was developed at Technische Universität Dresden [358] and marketed by Morpheus Space GmbH [359]. This miniature thruster is fabricated in accordance with the classical scheme with a needle W-emitter and a porous W-reservoir, in order to prevent liquid gallium from leaking due to vibrations at the launch of the spacecraft. Because Ga melts at almost room temperature ($T_m\sim30\,^\circ$C), low power is needed for its heating and melting, of the order of 50–150 mW.

Figure 58 schematically shows a sectional view of the nanoFEEP next to a 1-euro coin. The current–voltage curve

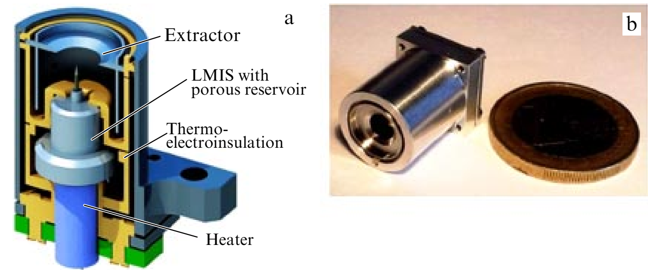

Figure 58. (a) Schematic image of a gallium nanoFEEP, (b) general view next to a 1-euro coin [358].

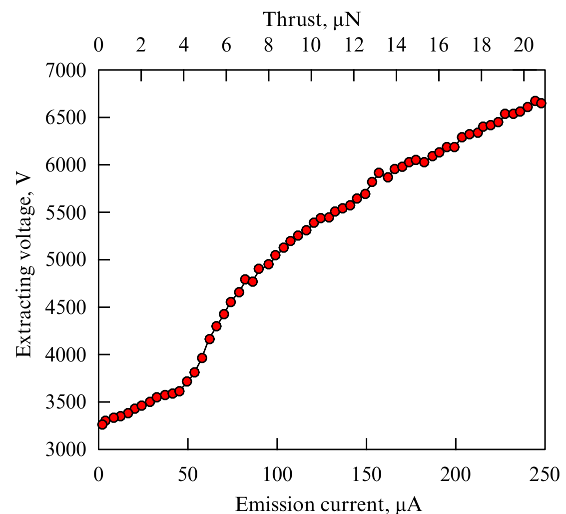

Figure 59. Current–voltage curve of a gallium nanoFEEP [359].

of the nanoFEEP is shown in Fig. 59, and its technological specifications are as follows:

— thrust: 1–20 μN (maximal value: 40 μN);
— specific impulse: $(3-8.5)\times10^3$ s;
— total impulse: up to 3.4×10^3 N s;
— working material (gallium) load: 6.5–13 g;
— outside envelop: $90\times25\times43$ mm;
— weight: 160 g (without working material);
— power: 0.2–3 W.

In view of its small size and low weight, the nanoFEEP, combined with a charge neutralizer and electron equipment, can be installed on the CubeSat 1U platform. For module satellites (2–3U), a cluster multiFEEP engine is available that can produce up to 140 μN of thrust at the same specific and total impulses as for nanoFEEP, but with a maximum power of 19 W. The working material load is 33–125 g, and the weight of the engine itself (without the working material) is 280 g.

FEEP thrusters with cesium and rubidium as working materials have been developed since the 1970s by ESTEC (The Netherlands) and then by Italian companies CENTROSPAZIO, ALTA, and SITAEL with support from the European Space Agency (ESA). The cesium microthruster FT-150 [360] was designed in the framework of the ESA project Lisa Pathfinder, whose goal was to collect preliminary information on the possibility of detecting gravitational waves to subsequently verify the general relativity theory by the space observatory LISA (Laser Interferometer Space Antenna). A feature of the FT-150

microthruster was the use of an extended slit emitter, where numerous point-like Taylor cones were formed (up to a hundred per millimeter in length) [79, 361]. Some technological specifications of this device are as follows:

— thrust: 0.1–150 μN;
— specific impulse: up to 4.5×10^3 s;
— total impulse: more than 3×10^3 N s;
— working material (cesium) load: 92 g;
— weight: 1410 g (without working material);
— power: 6 W.

The FT-150 microthruster or, rather, a propelling module equipped with four such microthrusters, did not take part in the ESA Lisa Pathfinder mission launched in 2015. By its specifications, mainly due to its substantial weight and chemically active cesium, FT-150 is not suitable for CubeSat satellites. Subsequently, the slit design of the emitter was used in microthrusters with ionic liquids as propellants.

The development of FEEP thrusters with liquid metal ion sources began 45 years ago. Ion sources with ionic liquids, discussed in Section 5, are also suitable for engines of CubeSat satellites. The development of ILISs for these purposes began relatively recently, and so far there are no commercial microthrusters with ionic liquids on the market of space exploration equipment. However, experimental models and prototypes have already been built and tested (so far, in ground tests). Detailed information on their design and characteristics can be found in review [25] and original papers [362–367].

Closing this section, devoted to EHD sources for microthrusters, we note that a major problem that will have to be solved for such sources to enjoy broader use aboard satellites in near-Earth space and on long-term space missions is the contamination of the spacecraft surface with a plume of emitted ions and products of sputtering elements, as well as contamination of the thrusters themselves with ion beams. For thrusters working on liquid metals and alloys, this problem appears to be more pressing than for ionic liquid sources. In both cases, systems of ion beam ejection from the spacecraft must be optimized, and materials with low sputter yields must be used.

7. Conclusions and prospects

We have tried to describe the main stages of the development and improvement of EHD ion sources, describe their structural and physical features, analyze the physical principles underlying their work, and show modern domains of application of these sources, emphasizing their unique potential that singles out EHD sources from among other types of ion sources.

It is commonly believed that, in various areas of human activity, any modern analytic apparatus evolves through several major stages in the course of its design and implementation: (1) formulation of scientific principles underlying its operation, (2) experimental verification of prototypes, (3) fabrication of a mass-produced apparatus, (4) in-depth investigation of the mechanisms of its operation and the corresponding improvements to the apparatus and the methods for its use, (5) commercialization (launching on the market), (6) broadening and deepening the domain of applications, and, finally, (7) making the manufacturing standard and routine. Following this pattern, EHD sources are at the seventh stage, but this does not imply that their potential is already exhausted. The appearance of new, more efficient, LMAISs, the development of sources with room temperature ionic liquids (with 'liquid plasma'), the successful development and use of FEEP microthrusters, and many other details show that the process of EHD development is far from being completed.

Regretfully, EHD sources of ions, which are part of a class of high-tech and innovative instrumentation, are currently at a virtually zero level of design and production in Russia, although a proven track record of building them existed in the USSR. One of the main goals of this review was therefore to attract attention and possibly rekindle the interest of Russian researchers in the development and application of these sources in micro- and nanotechnology, in space exploration, and in solving fundamental and applied problems.

To conclude, we note that the design and development of EHD emitters have led to the creation of a fundamentally new method for generating high-brightness ion beams. This method, along with the surface-plasma method for obtaining negative-ion beams [368–370], ECR-generation of multicharge ions [371], and the electron beam method for obtaining multicharge ions [372], is a key to the new ion beam techniques developed over the last 50 years.

Acknowledgments

We thank A Melnikov, L Bischoff, W Pilz, L Bruchhaus, J Gierak, R Jede, A L Shabalin, and D V Kovalevsky for their fruitful collaboration in developing EHD emitters and systems based on them, as well as E Ya Chernyak for making his publications available to us and for the useful discussion of our work. One of the authors (ABT) is thankful to the RF Ministry of Science and Higher Education for partial financial support in the framework of a state assignment (FSSN-2020-0003).

References

1. Bruchhaus L et al. *Appl. Phys. Rev.* **4** 011302 (2017)
2. Bischoff L et al. *Appl. Phys. Rev.* **3** 021101 (2016)
3. Gierak J et al. *J. Vac. Sci. Technol. B* **36** 06J101 (2018)
4. Bassim N, Notte J "Focused ion beam instruments", in *Materials Characterization* (ASM Handbook, Vol. 10) (Materials Park, OH: ASM Intern., 2019) p. 635
5. Machalett F, Seidel P "Focused ion beams and some selected applications", in digital *Encyclopedia of Applied Physics* (New York: Wiley-VCH Verlag, 2019)
6. Zhakin A I *Phys. Usp.* **56** 141 (2013); *Usp. Fiz. Nauk* **183** 153 (2013)
7. Utke I, Moshkalev S, Russell P (Eds) *Nanofabrication Using Focused Ion and Electron Beams: Principles and Applications* (Oxford: Oxford Univ. Press, 2012)
8. Giannuzzi L A, Stevie F A (Eds) *Introduction to Focused Ion Beams. Instrumentation, Theory, Techniques and Practice* (New York: Springer-Verlag, 2005)
9. Bassim N, Scott K, Giannuzzi L A *MRS Bull.* **39** 317 (2014)
10. Gabovich M D *Sov. Phys. Usp.* **26** 447 (1983); *Usp. Fiz. Nauk* **140** 137 (1983)
11. Ruedenauer F G, in *Secondary Ion Mass Spectrometry SIMS IV. Proc. of the Fourth Intern. Conf., Osaka, Japan, November 13–19, 1983* (Springer Series in Chemical Physics, Vol. 36, Eds A Benninghoven et al.) (Berlin: Springer-Verlag, 1984) p. 133
12. Benninghoven A, Rüdenauer F G, Werner H W *Secondary Ion Mass Spectrometry. Basic Concepts, Instrumental Aspects, Applications, and Trends* (New York: J. Wiley, 1987)
13. Wilson R G, Stevie F A, Magee C W *Secondary Ion Mass Spectrometry: a Practical Handbook for Profiling and Bulk Impurity Analysis* (New York: Wiley, 1989)
14. Cherepin V T *Ionnyi Mikrozondovyi Analiz* (Ionic Microprobe Analysis) (Kiev: Naukova Dumka, 1992)
15. Oechsner H *Int. J. Mass Spectrom. Ion Proces.* **143** 271 (1995)
16. Berthold W, Wucher A *Surf. Interface Anal.* **23** 393 (1995)

17. Wucher A "Laser post-ionization — fundamentals", in *ToF-SIMS: Materials Analysis by Mass Spectrometry* (IM Publ. and Surface Spectra, Eds J C Vickerman, D Briggs) 2nd ed. (Manchester: IM Publications LLP, 2013)
18. Baturin V A, Eremin S A *Poverkhnost' Rentgen. Sinkhrotron. Neitron. Issled.* (7) 87 (2008)
19. Rüdenauer F G *Surf. Interface Anal.* **39** 116 (2007)
20. Tajmar M et al. *Ultramicroscopy* **109** 442 (2009)
21. Müller E W *Science* **149** 591 (1965)
22. Hlawacek G, Göltzhäuser A (Eds) *Helium Ion Microscopy* (Cham: Springer Intern. Publ., 2016)
23. Lozano P, Martínez-Sánchez M *J. Colloid Interface Sci.* **282** 415 (2005)
24. Welton T *Chem. Rev.* **99** 2071 (1999)
25. Tolstogouzov A B et al. *Instrum. Exp. Tech.* **58** 1 (2015); *Prib. Tekh. Eksp.* (1) 5 (2015)
26. Prewett P D, Mair G L R *Focused Ion Beams from Liquid Metal Ion Sources* (Taunton: Research Studies Press, 1991)
27. Forbes R G, Mair G L R, in *Handbook of Charged Particle Optics* (Ed. J Orloff) 2nd ed. (Boca Raton, FL: CRC Press. Taylor and Francis, 2009) p. 29
28. Orloff J, Utlaut M, Swanson L *High Resolution Focused Ion Beams: FIB and Its Applications: the Physics of Liquid Metal Ion Sources and Ion Optics and their Application to Focused Ion Beam Technology* (New York: Kluwer Acad. Plenum Publ., 2003)
29. Wolf B (Ed.) *Handbook of Ion Sources* (Boca Raton, FL: CRC Press, 1995)
30. Zhang H *Ion Sources* (New York: Science Press. Springer, 1999)
31. Brown I G *The Physics and Technology of Ion Sources* (New York: Wiley, 1989); Translated into Russian: *Fizika i Tekhnologiya Istochnikov Ionov* (Moscow: Mir, 1998)
32. Mackenzie R A D, Smith G D W *Nanotechnology* **1** 163 (1990)
33. Gilbert W *De Magnete* (Transl. P F Mottelay) Facsimile (New York: Dover Publ., 1958)
34. Gray S *Philos. Trans. R. Soc. Lond.* **37** 227 (1732); *Philos. Trans. R. Soc. Lond.* **37** 260 (1732)
35. Rayleigh Lord *Proc. R. Soc. Lond.* **29** 71 (1879)
36. Zeleny J *Phys. Rev.* **3** 69 (1914)
37. Zeleny J *Phys. Rev.* **10** 1 (1917)
38. Zeleny J *J. Franklin Inst.* **219** 659 (1935)
39. Müller E W *Z. Phys.* **131** 136 (1951)
40. Krohn V E *Prog. Astronaut. Rocketry* **5** 73 (1961)
41. Swatik D S, Hendricks C D *Am. Inst. Aeronautics Astronautics J.* **6** 1596 (1968); *Raketn. Tekh. Kosmonavtika* **6** (8) 195 (1968)
42. Mahoney J F et al. *J. Appl. Phys.* **40** 5101 (1969)
43. Gomer R *Field Emission and Field Ionization* (Harvard Monographs in Applied Science, No. 9) (Cambridge, MA: Harvard Univ. Press, 1961) p. 134
44. Taylor G I *Proc. R. Soc. Lond. A* **280** 383 (1964)
45. Krohn V E, Ringo G R *Appl. Phys. Lett.* **27** 479 (1975)
46. Krohn V E, Ringo G R *Int. J. Mass. Spectrom. Ion Phys.* **22** 307 (1976)
47. Clampitt R, Aitken K L, Jeffries D K *J. Vac. Sci. Technol.* **12** 1208 (1975)
48. Seliger R L et al. *Appl. Phys. Lett.* **34** 310 (1979)
49. Venkatesan T, Wagner A, Barr D *Appl. Phys. Lett* **38** 943 (1981)
50. Dudnikov V G, Shabalin A L "Elektrogidrodinamicheskie emittery ionnykh puchkov" ("Electrohydrodynamic emitters of ion beams"), Preprint 90-31 (Novosibirsk: Institute of Nuclear Physics, Siberian Branch, USSR Academy of Sciences, 1990); https://inis.iaea.org/collection/NCLCollectionStore/_Public/22/057/22057152.pdf?r = 1&r = 1
51. Dudnikov V G, Shabalin A L *Prikl. Mekh. Tekh. Fiz.* (2) 3 (1990)
52. Belchenko Y I et al. *Rev. Sci. Instrum.* **61** 378 (1990)
53. Dudnikov V G, Shabalin A L *Rev. Sci. Instrum.* **63** 2460 (1992)
54. Dudnikov V G, Shabalin A L *Pis'ma Zh. Tekh. Fiz.* **11** 808 (1985)
55. Dudnikov V, arXiv:2003.07354
56. Bell A E et al. *Int. J. Mass Spectrom. Ion Proc.* **88** 59 (1989)
57. Panitz J A, Pregenzer A L, Gerber R A *J. Vac. Sci. Technol. A* **7** 64 (1989)
58. Alyakrinskaya N V et al. *Pis'ma Zh. Tekh. Fiz.* **16** (19) 83 (1990)
59. Dudnikov V G *Rev. Sci. Instrum.* **67** 915 (1996)
60. Milovanov R A, Erofeeva E V *Nano- Mikrosist. Tekh.* (11) 20 (2015)
61. Zorzos A N, Lozano P C *J. Vac. Sci. Technol. B* **26** 2097 (2008)
62. Smith N S, Notte J A, Steele A V *MRS Bull.* **39** 329 (2014)
63. Delobbe A, Salord O, Sudraud P, "i-FIB. The ECR-FIB", in *The European Focused Ion Beam Users Group, EFUG, Annual Meeting, October 3, 2011, Bordeaux, France*; http://efug.imec.be/EFUG2011_08_Delobbe.pdf
64. Smith N et al. *Microscopy Today* **17** (5) 18 (2009)
65. Malherbe J et al. *Anal. Chem.* **88** 7130 (2016)
66. Viteau M et al. *Ultramicroscopy* **164** 70 (2016)
67. Knuffman B, Steele A V, McClelland J J *J. Appl. Phys.* **114** 044303 (2013)
68. Xu X et al. *Nucl. Instrum. Meth. Phys. Res. B* **404** 52 (2017)
69. Xu X et al. *Microelectron. Eng.* **174** 20 (2017)
70. Zhukov V A, Kalbittser Z *Mikroelektron.* **40** (1) 21 (2011)
71. Gierak J, Septier A, Vieu C *Nucl. Instrum. Meth. Phys. Res. A* **427** 91 (1999)
72. Orloff J (Ed.) *Handbook of Charged Particle Optics* (Boca Raton, FL: CRC Press, 1997)
73. Reiser M *Theory and Design of Charged Particle Beams* 2nd ed. (Weinheim: Wiley-VCH, 2008)
74. Pöpel C "Charakterisierung einer neuartigen Ionenstrahlsäule mit Geschwindigkeitsfilter (ExB) für Legierungsfilamente", Master-Thesis (Bochum: Ruhr-Univ. Bochum, 2013)
75. Solov'ev A V, Tolstoguzov A B *Sov. Phys. Tech. Phys.* **32** 580 (1987); *Zh. Tekh. Fiz.* **57** 953 (1987)
76. Klingner N et al. *Beilstein J. Nanotechnol.* **11** 1742 (2020)
77. Guilet S et al. *Microelectron. Eng.* **88** 1968 (2011)
78. Mitterauer J *IEEE Trans. Plasma Sci.* **15** 593 (1987)
79. Marcuccio S, Giusti N, Tolstoguzov A, in *Proc. of the 31st Intern. Electric Propulsion Conf. IEPC-2009, Sept. 20–24, 2009* (Ann Arbor, MI: Univ. of Michigan, 2009) p. 180
80. Hren J J, Ranganathan S (Eds) *Field-Ion Microscopy* (New York: Plenum Press, 1968); Translated into Russian: *Avtoionnaya Mikroskopiya* (Moscow: Mir, 1971)
81. Forbes R G *Surf. Sci.* **61** 221 (1976)
82. Tsong T T *Atom-Probe Field Ion Microscopy* (Cambridge: Cambridge Univ. Press, 1990)
83. Swanson L M, Schwind G A, Bell A E *J. Appl. Phys.* **51** 3453 (1980)
84. Ching M et al. *J. Vac. Sci. Technol. B* **5** 1628 (1987)
85. Schottky W *Phys. Z.* **15** 872 (1914)
86. Kingham D R, Swanson L W *Appl. Phys. A* **34** 123 (1984)
87. Kingham D R, Swanson L W *Appl. Phys. A* **41** 157 (1986)
88. Vladimirov V V, Gorshkov V N *Dokl. Akad. Nauk SSSR* **297** 1107 (1987)
89. Badan V E, Gasanov I S *Pis'ma Zh. Tekh. Fiz.* **15** (18) 49 (1989)
90. Sikharulidze G G, Burmii Zh P *Vysokochist. Veshchestva* (2) 171 (1987)
91. Dudnikov V G, Shabalin A L *Zh. Tekh. Fiz.* **55** 776 (1985)
92. Dudnikov V G, Shabalin A L *Zh. Tekh. Fiz.* **57** 185 (1987)
93. Kingham D R *Surf. Sci.* **116** 273 (1982)
94. Ganetsos Th et al. *Surf. Interface Analysis* **39** 128 (2007)
95. Mair G L R *J. Phys. D* **33** L86 (2000)
96. Venkatesan T et al. *Appl. Phys. Lett.* **39** 9 (1981)
97. Swanson L W, Bell A E, in *The Physics and Technology of Ion Sources* (Ed. I G Brown) (New York: Wiley, 1989) p. 313
98. Swanson L W, Bell A E "Zhidkometallicheskie ionnye istochniki", in *Fizika i Tekhnologiya Ionnykh Istochnikov* (Ed. I G Brown) (Moscow: Mir, 1998) p. 339
99. Hornsey R I, Marriott P *J. Phys. D* **22** 699 (1989)
100. Fano U, Fano L *Physics of Atoms and Molecules*; *an Introduction to the Structure of Matter* (Chicago, IL: Univ. of Chicago Press, 1972); Translated into Russian: *Fizika Atomov i Molekul* (Moscow: Nauka, 1980)
101. Grigor'ev A I *Tech. Phys. Lett.* **27** 305 (2001); *Pis'ma Zh. Tekh. Fiz.* **27** (7) 89 (2001)
102. Shiryaeva S O, Grigor'ev A I, Morozov V V *Tech. Phys.* **48** 822 (2003); *Zh. Tekh. Fiz.* **73** (7) 21 (2003)
103. Dole M et al. *J. Chem. Phys.* **49** 2240 (1968)
104. Hagena O F, Obert W *J. Chem. Phys.* **56** 1793 (1972)
105. De la Mora J F, Loscertales I G *J. Fluid Mech.* **260** 155 (1994)
106. Losano P *J. Phys. D* **39** 126 (2006)
107. Coffman C S, Martínez-Sánchez M, Lozano P C *Phys. Rev. E* **99** 063108 (2019)

108. Bischoff L et al. *Nucl. Instrum. Meth. Phys. Res. B* **161–163** 1128 (2000)
109. Forbes R G *Vacuum* **48** 85 (1997)
110. Forbes R G, Ljepojevic N N *Surf. Sci.* **266** 170 (1992)
111. Swanson L W *Nucl. Instrum. Meth. Phys. Res.* **218** 347 (1983)
112. Gierak J, Jede R, Hawkes P, in *Nanofabrication Handbook* (Eds S Cabrini, S Kawata) (Boca Raton, FL: CRC Press, 2012) Ch. 3, p. 41
113. Sudraud P, Colliex C, Van der Walle J *J. Physics* **40** 207 (1979)
114. Driesel W, Dietzsch C *Appl. Surf. Sci.* **93** 179 (1996)
115. Driesel W et al. *J. Vac. Sci. Technol. B* **14** 1621 (1996)
116. Driesel W, Dietzsch C, Möser M *J. Phys. D* **29** 2492 (1996)
117. Hesse E et al. *Jpn. J. Appl. Phys.* **35** 5564 (1996)
118. Bondarenko G G, Kabanova T A, Rybalko V V *Osnovy Materialovedeniya* (Introduction to Materials Science) (Ed. G G Bondarenko) (Moscow: BINOM. Laboratoriya Znanii, 2018) p. 95
119. Lyakishev N P *Diagrammy Sostoyaniya Dvoinykh Metallicheskikh Sistem* (State Diagrams of Binary Metal Systems) (Moscow: Mashinostroenie, 1996) Handbook in 3 vols
120. Landolt-Boernstein, in Madelung O (Ed.) *Group IV, Phase Equilibria, Crystallographic and Thermodynamic Data of Binary Alloys* (Berlin: Springer, 1995)
121. Massalski T B (Ed.) *Binary Alloy Phase Diagrams* (Materials Park, OH: ASM Intern., 1990)
122. Honig R E, Kramer D A *RCA Rev.* **30** 285 (1969)
123. Alcock C B, Itkin V P, Horrigan M K *Can. Metallurg. Quarterly* **23** 309 (1984)
124. Vapor Pressure Calculator, https://www.iap.tuwien.ac.at/www/surface/vapor_pressure
125. Grigoriev I S, Meilikhov E Z (Eds) *Handbook of Physical Quantities* (Boca Raton, Fl.: CRC Press, 1997); Translated from Russian: *Fizicheskie Velichiny. Spravochnik* (Moscow: Energoatomizdat, 1991)
126. Belashchenko D K *Phys. Usp.* **56** 1176 (2013); *Usp. Fiz. Nauk* **183** 1281 (2013)
127. Bell A E, Swanson L W *Appl. Phys. A* **41** 335 (1986)
128. Mair G L R et al. *Nucl. Instrum. Meth. Phys. Res. B* **217** 347 (2004)
129. Mair G L R, Thoms S *J. Phys. D* **22** 975 (1989)
130. Tegart W J *The Electrolytic and Chemical Polishing of Metals* (Oxford: Pergamon Press, 1959) p. 140
131. Mazarov P et al., in MRS Fall Meeting 2019, Boston, USA
132. Ishikawa J, Takagi T *J. Appl. Phys.* **56** 3050 (1984)
133. Vasiljevich I et al., in *The 32nd Intern. Electric Propulsion Conf., Wiesbaden, Germany, 2011*
134. Pilz W et al. *Rev. Sci. Instrum.* **88** 123302 (2017)
135. Deryagin B V, Churaev N V *Smachivayushchie Plenki* (Wetting Films) (Moscow: Nauka, 1984)
136. Wieck A D "Ionensorten", http://www.rub.de/afp/
137. Kukharchyk N et al. *Appl. Phys. A* **122** 1072 (2016)
138. Wortmann M et al. *Rev. Sci. Instrum.* **84** 093305 (2013)
139. Barr D L *J. Vac. Sci. Technol. B* **5** 184 (1987)
140. Rao S et al. *J. Vac. Sci. Technol. B* **7** 1787 (1989)
141. Vikulova I V et al. *Elektron. Promyshl.* (10) 39 (1990)
142. Zharkov V V, Parshin G D, Chernyak E Ya *Prib. Tekh. Eksp.* (1) 232 (1989)
143. Belykh S F et al. *Surf. Coatings Technol.* **53** 289 (1992)
144. Mazarov P et al. *Appl. Surf. Sci.* **254** 7401 (2008)
145. Bischoff L, Pilz W, Mazarov P, Wieck A D *Appl. Phys. A* **99** 145 (2010)
146. Kollmer F *Appl. Surf. Sci.* **231–232** 153 (2004)
147. Wagner A *J. Vac. Sci. Technol.* **16** 1871 (1979)
148. Gierak J et al. *Microelectron. Eng.* **87** 1386 (2010)
149. Ishitani T, Umemura K, Kawanami Y *J. Vac. Sci. Technol. B* **6** 931 (1988)
150. Dudnikov V G, Shabalin A L *Prib. Tekh. Eksp.* (5) 149 (1986)
151. Shabalin A L "Elektrogidrodinamicheskie istochniki ionnykh puchkov" ("Electrohydrodynamic sources of ion beams"), Ph.D. Thesis (Phys. Math. Sci.) (Novosibirsk: Institute of Nuclear Physics, Siberian Branch, USSR Academy of Sciences, 1989)
152. Van de Walle J, Tarento R J, Joyes P *Z. Phys. D* **20** 17 (1991)
153. Kreissig U *J. Phys. D* **23** 959 (1990)
154. Mair G L R et al. *Appl. Phys. A* **81** 385 (2005)
155. Bischoff L et al. *Ultramicroscopy* **100** 1 (2004)
156. Aidinis C J et al. *Microelectron. Eng.* **73–74** 116 (2004)
157. Higuchi-Rusli R *Rev. Sci. Instrum.* **67** 3501 (1996)
158. Bischoff L et al. *J. Phys. Conf. Ser.* **10** 214 (2005)
159. Georgieva S et al. *Vacuum* **51** (2) 99 (1998)
160. Shpyrko O G et al. *Science* **313** 77 (2006)
161. Mazarov P et al. *J. Vac. Sci. Technol. B* **27** (6) L47 (2009)
162. Berezovskaya V V, Ishina E A, Ozerets N N *Diagrammy Sostoyaniya Troinykh Sistem* (State Diagrams of Ternary Systems) (Moscow: Flinta, 2017)
163. Melnikov A et al. *Nucl. Instrum. Meth. Phys. Res. B* **195** 422 (2002)
164. Mazarov P et al. "Light and heavy ions from new non-classical liquid metal alloy ion sources for advanced nanofabrication", in *AVS 66th Intern. Symp. and Exhibition, Columbus, Ohio, October 20–25, 2019*
165. Bischoff L, Akhmadaliev Ch *J. Phys. D* **41** 052001 (2008)
166. Pilz W et al. *J. Vac. Sci. Technol. B* **37** 021802 (2019)
167. A Simple Sputter Yield Calculator, https://www.iap.tuwien.ac.at/www/surface/sputteryield
168. Ziegler J F, Biersack J P, Littmark U *The Stopping and Range of Ions in Solids* (New York: Pergamon Press, 1985) and version SRIM-2012.03; http://www.srim.com
169. Bischoff L et al. *J. Vac. Sci. Technol. B* **38** 042801 (2020)
170. Dudnikov V G, Shabalin A L, in *Fizika Klasterov* (Physics of Clusters) (Eds A A Vostrikov, A K Rebrov) (Novosibirsk: Inst. Teplofiz. SO AN SSSR, 1987) p. 23
171. Knapp W, Bischoff L, Teichert J *Appl. Surf. Sci.* **146** 134 (1999)
172. Thorn A et al. *Rev. Sci. Instrum.* **83** 02A511 (2012)
173. Swanson L W, Schwind G A *J. Appl. Phys.* **49** 5655 (1978)
174. Chen L W, Wang Y L *Appl. Phys. Lett.* **72** 389 (1998)
175. Rao K A et al. *J. Vac. Sci. Technol. B* **7** 1793 (1989)
176. Hata K et al. *J. Physique C 6* **49** 125 (1988)
177. Hata K et al. *J. Phys. Colloques* **48** C6-177 (1987)
178. Sheu B L, Wang Y L *Appl. Phys. Lett.* **80** 1480 (2002)
179. Mair G L R *J. Phys. D* **17** 2323 (1984)
180. Mair G L R *Vacuum* **36** 847 (1986)
181. Mair G L R *Nucl. Instrum. Meth. Phys. Res. B* **43** 240 (1989)
182. Vladimirov V V et al. *J. Vac. Sci. Technol. B* **9** 2582 (1991)
183. Forbes R G *J. Aerosol Sci.* **31** (1) 97 (2000)
184. Thompson S, Prewett D *J. Phys. D* **17** 2305 (1984)
185. Akhmadaliev Ch et al. *Microelectron. Eng.* **73–74** 120 (2004)
186. Shikin V B *Phys. Usp.* **54** 1203 (2011); *Usp. Fiz. Nauk* **181** 1241 (2011)
187. Vladimirov V V, Gorshkov V N *Dokl. Akad. Nauk SSSR* **297** 1107 (1987)
188. Gabovich M D, Gasanov I S, Protsenko I M *Zh. Tekh. Fiz.* **58** 2367 (1988)
189. Shabalin A L *Pis'ma Zh. Tekh. Fiz.* **15** (6) 27 (1989)
190. Kovalenko V P, Shabalin A L *Pis'ma Zh. Tekh. Fiz.* **15** (6) 62 (1989)
191. Beckman J C et al. *J. Vac. Sci. Technol. B* **15** 2332 (1997)
192. Alton G D, Read P M *Nucl. Instrum. Meth. Phys. Res. B* **54** 7 (1991)
193. Hagen C W, Fokkema E, Kruit P *J. Vac. Sci. Technol. B* **26** 2091 (2008)
194. Orloff J, Swanson L W *J. Vac. Sci. Technol.* **19** 1149 (1981)
195. Schwind G A, Swanson L W *J. Vac. Sci. Technol. B* **25** 2586 (2007)
196. Ward J W *J. Vac. Sci. Technol. B* **3** 207 (1985)
197. Georgieva S, Vichev R G, Drandarov N *Vacuum* **44** 1109 (1993)
198. Kamura M et al. *Appl. Phys. Lett.* **42** 908 (1983)
199. Knauer W *Optik* **59** 335 (1981)
200. Miyauchi E et al. *Jpn. J. Appl. Phys.* **26** L145 (1987)
201. Ishitani T, Kawanami Y, Shuhuri S *Jpn. J. Appl. Phys.* **26** 1777 (1987)
202. Kubena R L, Ward J W *Appl. Phys. Lett.* **51** 1960 (1987)
203. Ward J W, Utlaut M W, Kubena R L *J. Vac. Sci. Technol. B* **5** 169 (1987)
204. Ward J W, Kubena R L, Utlaut M W *J. Vac. Sci. Technol. B* **6** 2090 (1988)
205. Komuro M *Appl. Phys. Lett.* **52** 75 (1988)
206. Ishitani T et al. *Appl. Phys. A.* **44** 233 (1987)
207. *Advanced Focused Ion Beam Nanofabrication Capabilities of the NanoFIBTWO Source and Column Technology*, White Paper, Raith, 2014
208. Knauer W *J. Vac. Sci. Technol.* **16** 1676 (1979)
209. Mair G L R, Mulvey T, Forbes R G *J. Physique C* **9** 179 (1984)

210. Sudraud P, Colliex C, van de Walle J *J. Physique* **40** L207 (1979)
211. Dudnikov V G, Shabalin A L *Zh. Tekh. Fiz.* **60** (4) 131 (1990)
212. Beckman J C et al. *J. Vac. Sci. Technol. B* **14** 3911 (1996)
213. Sakurai T, Culbertson R J, Robertson G H *Appl. Phys. Lett.* **34** 11 (1979)
214. Kim Y G et al. *J. Phys. D* **31** 3463 (1998)
215. Bischoff L et al. *Microelectron. Eng.* **53** 613 (2000)
216. Hornsey R *Appl. Phys. A* **49** 697 (1989)
217. Aidinis C et al. *J. Phys. D* **34** L14 (2001)
218. Bischoff L *Nucl. Instrum. Meth. Phys. Res. B* **266** 1846 (2008)
219. Marriott P *Appl. Phys. A* **44** 329 (1987)
220. Ishitani T, Umemura K, Kawanami Y *J. Appl. Phys.* **61** 748 (1987)
221. Yang P et al. *J. Chem. Phys.* **135** 034502 (2011)
222. Bundaleski N et al. *Int. J. Mass Spectrom.* **353** 19 (2013)
223. Zhang S et al. *Ionic Liquids. Physicochemical Properties* (Amsterdam: Elsevier, 2009)
224. Perez-Martinez C et al. *Microelectron. Eng.* **88** 2088 (2011)
225. Larriba C et al. *J. Appl. Phys.* **101** 084303 (2007)
226. Losano P, Martínez-Sánchez M *J. Colloid Interface Sci.* **280** (1) 149 (2004)
227. Brikner N, Losano P *Appl. Phys. Lett.* **101** 193504 (2012)
228. Takeuchi M et al. *Nucl. Instrum. Meth. Phys. Res. B* **315** 234 (2013)
229. Takaoka G H et al. *Nucl. Instrum. Meth. Phys. Res. B* **315** 257 (2013)
230. Takeuchi M et al. *Nucl. Instrum. Meth. Phys. Res. B* **315** 345 (2013)
231. Perez-Martinez C S, Lozano P C *Appl. Phys. Lett.* **107** 043501 (2015)
232. Xu T, Tao Z, Lozano P C *J. Vac. Sci. Technol. B* **36** 052601 (2018)
233. Fujiwara Y et al. *J. Appl. Phys.* **111** 064901 (2012)
234. Fujiwara Y et al. *Surf. Interface Anal.* **45** 517 (2013)
235. Fujiwara Y, Saito N *Rapid Com. Mass Spectrom.* **31** 1859 (2017)
236. Perez-Martinez C et al. *J. Vac. Sci. Technol. B* **28** (3) L25 (2010)
237. Bischoff L *Nucl. Instrum. Meth. Phys. Res. B* **266** 1846 (2008)
238. Cherepin V T *Ionnyi Zond* (Ionic Probe) (Kiev: Naukova Dumka, 1981)
239. Bruchhaus L "An ion beam complement to electron beam writers", Dissertation, Lehrstuhl Experimentelle Physik l (Dortmund: Tech. Univ. Dortmund, 2012)
240. Bischoff L et al. "Nanostructures by mass-separated FIB", in *FIB Nanostructures* (Lecture Notes on Nanoscale Science and Technology, Vol. 20, Ed. Z Wang) (Berlin: Springer, 2013)
241. Bischoff L, Mair G L R *Recent Res. Developments Appl. Phys.* **6** 123 (2003)
242. Gierak J *Nanofabrication* **1** 35 (2014)
243. Sloyan K, Melkonyan H, Dahlem M S *Int. J. Adv. Manuf. Technol.* **107** 4469 (2020)
244. Baglin J E E *Appl. Phys. Rev.* **7** 011601 (2020)
245. Mühle R *Rev. Sci. Instrum.* **63** 3040 (1992)
246. Joshi-Imre A, Bauerdick S *J. Nanotechnology* **2014** ID170415 (2014)
247. Bauerdick S et al. *J. Vac. Sci. Technol. B* **31** 06F404 (2013)
248. Nadzeyka A et al. *Microelectron. Eng.* **98** 198 (2012)
249. Wanzenboeck H D, Waid S "Focused ion beam lithography", in *Recent Advances in Nanofabrication Techniques and Applications* (Ed. B Cui) (Rijeka: InTech, 2011)
250. Bauerdick S *Microscopy Analysis* (January/February) 11–13 (2018)
251. Yao N, Epstein A K, in *Microscopy: Science, Technology, Applications and Education* (Badajoz: Formatex Research Center, 2010) p. 2190
252. Stanishevsky A V "Focused ion beam nanofabrication", in *Encyclopedia of Nanoscience and Nanotechnology* Vol. 3 (Ed. H S Nalwa) (Stevenson Ranch, CA: American Scientific Publ., 2004) p. 469
253. Watt F et al. *Int. J. Nanosci.* **4** 269 (2005)
254. Matsui S et al. *J. Vac. Sci. Technol. B* **9** 2622 (1991)
255. Bischoff L *Ultramicroscopy* **103** 59 (2005)
256. Melngailis J *J. Vac. Sci. Technol. B* **5** 469 (1987)
257. Tseng A A *Nanolithography* **6** 594 (2005)
258. Evstrapov A A et al. *Nauch. Tekh. Vestn. St. Petersburg Gos. Univ. Inf. Tekh. Mekh. Opt.* (4) 59 (2010)
259. Gierak J *Semicond. Sci. Technol.* **24** 043001 (2009)
260. Gierak J et al. *Ultramicroscopy* **109** 457 (2009)
261. Seniutinas G et al. *Nanofabrication* **2** 54 (2015)
262. RAITH. Nanofabrication, https://www.raith.com/
263. Jede R *Nanoindustriya* (2) 8 (2012)
264. *VELION: FIB-SEM where FIB truly comes first. FIB and SEM for Nanofabrication, Nanoengineering and Inspection*, Technical Notes, Raith (2019)
265. Mazarov P *Lithography Meets FIB: Gallium Free Focused Ion Beam Nanofabrication*, FIB Workshop Zurich, 23.06.2014
266. Chen Y et al. *Nano Lett.* **16** 3253 (2016)
267. Nadzeyka A et al. *FIB Based Sketch and Peel with Various Ion Species for Fast and Precise Patterning of Large Structures*, EIPBN Conference (2018)
268. Levi-Setti R, Fox T R *Nucl. Instrum. Meth.* **168** 139 (1980)
269. Yao N, Wang Z L (Eds) *Handbook of Microscopy for Nanotechnology* (Dordrecht: Kluwer Acad. Publ., 2005)
270. Yao N, Wang Z L (Eds) *Spravochnik po Mikroskopii dlya Nanotekhnologii* (Handbook of Microscopy for Nanotechnology) (Moscow: Nauchnyi Mir, 2011)
271. Volkert M A, Minor A M *MRS Bull.* **32** 389 (2007)
272. Phaneuf M W *Micron* **30** 277 (1999)
273. Nastasi M, Mayer J, Hirvonen J *Ion-Solid Interactions: Fundamentals and Applications* (Cambridge Solid State Science Series) (Cambridge: Cambridge Univ. Press, 1996)
274. Nastasi M, Mayer J W *Ion Implantation and Synthesis of Materials* (Berlin: Springer-Verlag, 2006)
275. Utke I, Hoffmann P, Melngailis J *J. Vac. Sci. Technol. B* **26** 1197 (2008)
276. Giannuzzi L A, Stevieb F A *Micron* **30** 197 (1999)
277. Mayer J et al. *MRS Bull.* **32** 400 (2007)
278. Langford E M, Rogers M *Micron* **39** 1325 (2008)
279. Kuznetsova M A, Luchinin V V, Savenko A Yu *Izv. St. Petersburg Gos. Elektrotekh. Univ. 'LETI'. Ser. Fiz. Tverd. Tela Elektron.* (2) 28 (2006)
280. Pezzagna S et al. *Small* **6** 2117 (2010)
281. Lesik M et al. *Phys. Status Solidi A* **210** 2055 (2013)
282. Kunstmann T et al. *Rev. Sci. Instrum.* **77** 086105 (2006)
283. Konoplev B G et al. *Mikroelektron.* **41** 47 (2012)
284. Tolstoguzov A B *Mass-Spektrom.* **6** 280 (2009); *J. Anal. Chem.* **65** 1311 (2010)
285. Miyaki T et al. *Cell Tissue Res.* **379** 245 (2020)
286. Nastasi M, Mayer J W *Mater. Sci. Eng.* **12** (1) 1 (1994)
287. Rangelow I W et al. *J. Vac. Sci. Technol. B* **36** (6) 06J102 (2018)
288. Holz M et al. *Microscopy Today* **27** (6) 24 (2019)
289. Mykkänen E et al. *Nanomaterials* **10** 950 (2020)
290. Tilli M et al. *Handbook of Silicon Based MEMS Materials and Technologies* (Waltham: Elsevier, 2020)
291. Dubrovin A N, Dudnikov V G, Kovalevskii D V, Shabalin A L *Prib. Tekh. Eksp.* (2) 180 (1991); Preprint 89-50 (Novosibirsk: Institute of Nuclear Physics, Siberian Branch, USSR Academy of Sciences, 1989); http://irbiscorp.spsl.nsc.ru/fulltext/prepr/1989/p1989_50.pdf
292. Prewett P D, Kellogg E M *Nucl. Instrum. Meth. Phys. Res. B* **6** 135 (1985)
293. Reyntjens S, Puers R *J. Micromech. Microeng.* **11** 287 (2001)
294. Luchinin V V "Nanorazmernye ionno-luchevye tekhnologii" ("Nano-size ion beam technology"), in Luchinin V V, Savenko A Yu *Nanotekhnologiya: Fizika, Protsessy, Diagnostika, Pribory. Monografiya* (Nanotechnology: Physics, Processes, Diagnostics, Devices) (Eds V V Luchinin, Yu M Tairov) (Moscow: Fizmatlit, 2006) p. 284
295. Yao N *Focused Ion Beam Systems — Basics and Applications* (Cambridge: Cambridge Univ. Press, 2007)
296. Smith N S, Notte J A, Steele A V *MRS Bull.* **39** 320 (2014)
297. Gila B et al. *AIP Conf. Proc.* **1336** 243 (2011)
298. Benkouider A et al. *Thin Solid Films* **543** 69 (2013)
299. Appleton B R et al. *Nucl. Instrum. Meth. Phys. Res. B* **272** 153 (2011)
300. Bussone G et al. *J. Appl. Cryst.* **46** 887 (2013)
301. Scholz S et al., arXiv:1506.08989
302. Tongay S et al. *Appl. Phys. Lett.* **100** 073501 (2012)
303. Pearton S J et al. *J. Nanoeng. Nanomanuf.* **1** 35 (2011)
304. Gila B P *Microscopy Analysis* (November) 7 (2013)
305. Escovitz W H, Fox T R, Levi-Setti R *Proc. Natl. Acad. Sci. USA* **72** 1826 (1975)
306. Vickerman J C, Swift A, in *Surface Analysis — The Principal Techniques* (Ed. J C Vickerman) (Chichester: Wiley, 1997) p. 135

307. Lamberti W A, in *Handbook of Microscopy for Nanotechnology* (Eds N Yao, Z L Wang) (Boston: Kluwer Acad. Publ., 2005) p. 207
308. Volkov S S, Denisov A G, Tolstoguzov A B "Vtorichno-ionnye mass-spektrometry" ("Secondary ion mass spectrometers"), in *Obzory po Elektronnoi Tekhnike. Ser. 7 Tekhnologiya, Organizatsiya Proizvodstva i Oborudovanie* (Reviews in Electronic Engineering. Ser. 7 Technology, Production Management, and Equipment) (Moscow: TsNII 'Elektronika', 1987) p. 61
309. Volkov S S, Tolstoguzov A B "Posloinyi analiz poluprovodnikovykh materialov metodom vtorichno-ionnoi mass-spektrometrii" ("Depth profiling of semiconducting materials by secondary ion mass spectrometry"), in *Obzory po Elektronnoi Tekhnike. Ser. 7. Tekhnologiya, Organizatsiya Proizvodstva i Oborudovanie* (Reviews in Electronic Engineering Ser. 7 Technology, Production Management, and Equipment) Issue 4(1338) (Moscow: TsNII 'Elektronika', 1988) p. 48
310. Tolstoguzov A B "Perspektivnye napravleniya razvitiya metoda vtoricho-ionnoi mass-spektrometrii" ("Advanced trends in secondary ion mass spectrometry"), in *Obzory po Elektronnoi Tekhnike. Ser. Tekhnologiya, Organizatsiya Proizvodstva i Oborudovanie* (Reviews in Electronic Engineering Ser. Technology, Production Management, and Equipment) Issue 5(1604) (Moscow: TsNII 'Elektronika', 1991) p. 67
311. Tolstoguzov A B *Poverkhnost'* (4) 5 (1994)
312. Wucher A, Fisher G L, Mahoney C M, in *Cluster Secondary Ion Mass Spectrometry: Principles and Applications* (Ed. C M Mahoney) (Singapore: Wiley, 2013) p. 207
313. Zhang L, Dai C, Zhang J *Surf. Interface Anal.* **52** (5) 306 (2020)
314. Gall' L N et al. *Mass-Spektrom.* **5** 295 (2008)
315. Castaing R, Slodzian G *J. Microsc.* **1** 395 (1962)
316. Liebl H *J. Appl. Phys.* **38** 5277 (1967)
317. Levi-Setti R, Wang Y, Crow G *J. Phys. Colloq.* **45** (C9) 197 (1984)
318. Levi-Setti R, Wang Y L, Crow G *Appl. Surf. Sci.* **26** 249 (1986)
319. Chabala J M et al. *Int. J. Mass Spectrom. Ion Proc.* **143** 191 (1995)
320. Gavrilov K L et al. *J. Am. Ceram. Soc.* **82** 1001 (1999)
321. Strick R et al. *J. Cell Biology* **155** 899 (2001)
322. Nomura S et al. *Surf. Interface Anal.* **16** 105 (1990)
323. Khursheed A, Cheong K H, Hoang H Q *J. Vac. Sci. Technol. B* **28** C6F10 (2010)
324. Eccles A J, Steele T A, Robinson A W *Appl. Surf. Sci.* **144–145** 106 (1999)
325. Chérioux F et al. *Appl. Surf. Sci.* **253** 6140 (2007)
326. Volkov S S et al. *Elektron. Promyshl.* (10) 13 (1990)
327. Sun S et al. *Surf. Interface Anal.* **36** 1367 (2004)
328. Walker A V, Winograd N *Appl. Surf. Sci.* **203–204** 198 (2003)
329. Touboul D et al. *J. Am. Soc. Mass Spectrom.* **16** 1608 (2005)
330. Winograd N "The development of secondary ion mass spectrometry (SIMS) for imaging", in *The Encyclopedia of Mass Spectrometry* Vol. 9 *Historical Perspectives* Pt. A *The Development of Mass Spectrometry* (Eds K A Nier, A L Yergey, P J Gale) (Amsterdam: Elsevier, 2016) p. 103
331. Arushanov K A et al. *Appl. Surf. Sci.* **265** 642 (2013)
332. Drozdov M N et al. *Thin Solid Films* **577** 11 (2015)
333. Drozdov M N et al. *Thin Solid Films* **607** 25 (2016)
334. Tolstogouzov A et al. *Rapid Commun. Mass Spectrom.* **33** 323 (2019)
335. Rüdenauer F G *Surf. Interface Anal.* **6** (3) 132 (1984)
336. Veryovkin I V et al. *Nucl. Instrum. Meth. Phys. Res. B* **261** 508 (2007)
337. Pelster A et al. *Anal. Chem.* **88** 9638 (2016)
338. Wirtz T et al. *Nanotechnology* **26** 434001 (2015)
339. Bayly A R, Waugh A R, Anderson K *Nucl. Instrum. Meth.* **218** 375 (1983)
340. Eswara S et al. *Appl. Phys. Rev.* **6** 021312 (2019)
341. Pillatsch L, Ostlund F, Michler J *Prog. Crystal Growth Characterization Mater.* **65** (1) 1 (2019)
342. Grad R, Knott K, Pedersen A *Space Sci. Rev.* **34** 289 (1983)
343. Riedler W et al. *Space Sci. Rev.* **79** 271 (1997)
344. Stephan T *Planet. Space Sci.* **49** 859 (2001)
345. Shilobreeva S N *Mass-Spektrom.* **14** (1) 40 (2017)
346. Riedler W et al. *ESA-ISY* **4** 127 (1992)
347. Hamelin M et al. *Adv. Space Res.* **10** (3–4) 49 (1990)
348. Pomathoid L, Michau J L, Hamelin M *Rev. Sci. Instrum.* **59** 2409 (1988)
349. Hornung K et al. *Planet. Space Sci.* **103** 309 (2014)
350. Bardyn A et al. *Mon. Not. R. Anstron. Soc.* **469** S712 (2017)
351. Tajmar M *Advanced Space Propulsion Systems* (Wien: Springer, 2003)
352. Busek Co. Inc., http://www.busek.com/index.htm (2020)
353. FOTEC Forschungs- und Technologietransfer GmbH, https://www.fotec.at (2020)
354. Waydo S, Henry D, Campbell M *IEEE Aerospace Conf. Proc.* **1** 435 (2002)
355. CubeSat, http://www.cubesat.org (2020)
356. Enpulsion, https://www.enpulsion.com (2020)
357. Schönherr T et al., in *Proc. of the 36th Inter. Electric Propulsion Conf. IEPC-2019, Sept. 15–20, 2019* (Vienna: Univ. of Vienna, 2019) p. 362
358. Bock D, Tajmar M *Acta Astronautica* **144** 422 (2018)
359. Morpheus Space, https://www.morpheus-space.com (2020)
360. Paita L et al., in *Proc. of the 31st Inter. Electric Propulsion Conf. IEPC-2009, Sept. 20 – 24, 2009* (Ann Arbor, MI: Univ. of Michigan, 2009) p. 186
361. Marcuccio S, Genovese A, Andrenucci M *J. Propulsion Power* **14** 774 (1998)
362. Courtney D G, Li H Q, Losano P *J. Phys. D* **45** 485203 (2012)
363. Krpoun R et al. *Appl. Phys. Lett.* **94** 163502 (2009)
364. Krpoun R, Shea H R *J. Micromech. Microeng.* **19** 045019 (2009)
365. Dandavino S et al., in *Proc. of the 33rd Inter. Electric Propulsion Conf. IEPC-2013, Oct. 6–10, 2013* (Washington, DC: The George Washington Univ., 2013) p. 127
366. MEMS-Based Electric Micropropulsion for Small Spacecraft to Enable Robotic Space Exploration and Space Science, http://cordis.europa.eu/projects/263035 (2020)
367. Marcuccio S, Pergola P, Giusti N "IL–FEEP: a simplified, low cost electric thruster for micro- and nano-satellites", Paper presented at the ESA-CNES Small Satellites Systems and Services (4S) Symp., Portorose, Slovenia (2012)
368. Dudnikov V *Istochniki Otritsatel'nykh Ionov* (Negative Ion Sources) (Novosibirsk: NGU, 2018)
369. Dudnikov V *Development and Applications of Negative Ion Sources* (Berlin: Springer, 2019)
370. Dudnikov V G *Phys. Usp.* **62** 1233 (2019); *Usp. Fiz. Nauk* **189** 1315 (2019)
371. Geller R *Electron Cyclotron Resonance Ion Sources and ECR Plasmas* 1st ed. (Bristol: Institute of Physics Publ., 1996)
372. Donets E D *Sov. J. Part. Nucl.* **13** 388 (1982); *Fiz. Elem. Chastits Atom. Yadra* **13** 941 (1982)